

## Wall ironing of polymer coated sheet metal

**Citation for published version (APA):**

Aa, van der, M. A. H. (1999). *Wall ironing of polymer coated sheet metal*. [Phd Thesis 1 (Research TU/e / Graduation TU/e), Mechanical Engineering]. Technische Universiteit Eindhoven.  
<https://doi.org/10.6100/IR519715>

**DOI:**

[10.6100/IR519715](https://doi.org/10.6100/IR519715)

**Document status and date:**

Published: 01/01/1999

**Document Version:**

Publisher's PDF, also known as Version of Record (includes final page, issue and volume numbers)

**Please check the document version of this publication:**

- A submitted manuscript is the version of the article upon submission and before peer-review. There can be important differences between the submitted version and the official published version of record. People interested in the research are advised to contact the author for the final version of the publication, or visit the DOI to the publisher's website.
- The final author version and the galley proof are versions of the publication after peer review.
- The final published version features the final layout of the paper including the volume, issue and page numbers.

[Link to publication](#)

**General rights**

Copyright and moral rights for the publications made accessible in the public portal are retained by the authors and/or other copyright owners and it is a condition of accessing publications that users recognise and abide by the legal requirements associated with these rights.

- Users may download and print one copy of any publication from the public portal for the purpose of private study or research.
- You may not further distribute the material or use it for any profit-making activity or commercial gain
- You may freely distribute the URL identifying the publication in the public portal.

If the publication is distributed under the terms of Article 25fa of the Dutch Copyright Act, indicated by the "Taverne" license above, please follow below link for the End User Agreement:

[www.tue.nl/taverne](http://www.tue.nl/taverne)

**Take down policy**

If you believe that this document breaches copyright please contact us at:

[openaccess@tue.nl](mailto:openaccess@tue.nl)

providing details and we will investigate your claim.

# Wall Ironing of Polymer Coated Sheet Metal

M.A.M. van der Aa



Wall Ironing  
of  
Polymer Coated Sheet Metal

This research project was carried out in co-operation with and sponsored by Hoogovens Research & Development, Centre for Packaging Technology.

CIP DATA LIBRARY TECHNISCHE UNIVERSITEIT EINDHOVEN

Aa, Michiel A.H. van der

Wall ironing of polymer coated sheet metal / door Michiel A.H. van der Aa.  
- Eindhoven : Technische Universiteit Eindhoven, 1999.

Proefschrift. - ISBN 90-386-0900-0

NUGI 841

Trefwoorden: plaatmaterialen; polymere coatings / omvormprocessen;  
wandstrekken / constitutieve modellen / Arbitrary Lagrange Euler methode  
Subject headings: polymer coated sheet metal / polymer coatings / forming  
processes; wall ironing / constitutive modelling / Arbitrary Lagrange Euler  
method

Printed by Universiteitsdrukkerij TU Eindhoven.

*Cover: Mark & Remark Communications, Beverwijk.*

Wall Ironing  
of  
Polymer Coated Sheet Metal

Proefschrift

ter verkrijging van de graad van doctor  
aan de Technische Universiteit Eindhoven,  
op gezag van de Rector Magnificus, prof.dr. M. Rem,  
voor een commissie aangewezen door het College voor Promoties  
in het openbaar te verdedigen  
op donderdag 4 maart 1999 om 16.00 uur

door

Michiel Adrianus Henricus van der Aa

geboren te Den Dungen

Dit proefschrift is goedgekeurd door de promotoren:

prof.dr.ir. F.P.T. Baaijens  
prof.dr.ir. H.E.H. Meijer

Copromotor:

dr.ir. P.J.G. Schreurs

*Voor Odette  
en voor mijn ouders*





# Contents

<b>Summary</b>	<b>ix</b>
<b>Notation</b>	<b>xi</b>
<b>1 Introduction</b>	<b>1</b>
1.1 General introduction . . . . .	1
1.2 The conventional DWI process . . . . .	3
1.3 A new approach for the DWI process . . . . .	4
1.4 Objective and line of research . . . . .	7
1.5 Outline of the thesis . . . . .	7
<b>2 Constitutive modelling</b>	<b>9</b>
2.1 Introduction . . . . .	9
2.2 Kinematics . . . . .	9
2.3 Generalised compressible Leonov model . . . . .	11
2.3.1 Compressible Leonov model with Eyring viscosity function . . . . .	11
2.3.2 Compressible Leonov model with Bodner-Partom viscosity function . . . . .	12
2.4 Material parameters for the generalised compressible Leonov model . . . . .	14
2.4.1 Material parameters for PET . . . . .	14
2.4.2 Material parameters for steel and aluminium . . . . .	17
2.5 Integration of the constitutive equations . . . . .	19
2.5.1 The Leonov model embedded in Rubin's formulation . . . . .	20
2.5.2 Incremental integration . . . . .	20
2.6 Concluding remarks . . . . .	23
<b>3 Operator Splitted Arbitrary Lagrange Euler method</b>	<b>25</b>
3.1 Introduction . . . . .	25
3.2 Operator Splitted ALE . . . . .	26
3.2.1 Numerical procedure and finite element formulation . . . . .	26
3.2.2 Consistent stiffness matrix . . . . .	29
3.2.3 Configuration of OS-ALE . . . . .	32
3.3 Transport algorithms . . . . .	32

3.3.1	Local Coordinate Matching method . . . . .	33
3.3.2	Discontinuous Galerkin method . . . . .	34
3.3.3	Performance of the convection schemes . . . . .	36
3.4	Validation of the method . . . . .	40
3.4.1	Backward extrusion forging problem . . . . .	40
3.4.2	Wall ironing of blank steel . . . . .	41
3.5	Concluding remarks . . . . .	43
<b>4</b>	<b>Experiments and model validation</b>	<b>45</b>
4.1	Introduction . . . . .	45
4.2	Strip ironing device . . . . .	45
4.2.1	Literature review of experimental devices . . . . .	45
4.2.2	Configuration of the strip ironing device . . . . .	47
4.2.3	Displacement measurement: Digital Image Correlation . . . . .	50
4.2.4	Numerical-experimental verification strategy . . . . .	54
4.3	Results . . . . .	57
4.3.1	Influence of die angle . . . . .	58
4.3.2	Influence of ironing velocity . . . . .	61
4.3.3	Influence of ironing reduction . . . . .	62
4.3.4	Sensitivity study of pressure and velocity dependence . . . . .	63
4.3.5	Analysis of flow paths and strain fields . . . . .	64
4.4	Full-scale experiment . . . . .	67
4.5	Conclusions . . . . .	69
<b>5</b>	<b>Conclusions and recommendations</b>	<b>73</b>
5.1	Conclusions . . . . .	73
5.2	Recommendations . . . . .	74
<b>A</b>	<b>Details on the stiffness matrices of the material models</b>	<b>77</b>
A.1	Compressible Leonov model . . . . .	77
A.2	Bodner-Partom model . . . . .	78
<b>B</b>	<b>Derivation and implementation of the Discontinuous Galerkin Method</b>	<b>81</b>
B.1	One-dimensional derivation of the DG method . . . . .	81
B.2	Two-dimensional implementation of the DG method . . . . .	85
	<b>Bibliography</b>	<b>89</b>
	<b>Samenvatting</b>	<b>95</b>
	<b>Dankwoord</b>	<b>97</b>
	<b>Curriculum Vitae</b>	<b>99</b>

# Summary

The Draw and Wall Ironing (DWI) process is a metal forming process, in which a deep drawing step is followed by a wall ironing operation, resulting in a thin walled, cylindrical product. Industrial application is found in a large number of products: food and beverage cans, battery housings, and gas and hydraulic cylinders. Currently, food and beverage cans are lacquered on the inside and outside of the can. Several washing steps are necessary to remove lubricants and emulsions. The washing and lacquering of the cans are costly and, moreover, cause a significant environmental load.

In this thesis, an alternative method is studied, in which polymer coated sheet metal is formed into a can. The coating functions as: (1) a lubricant during deformation, (2) a protection layer against corrosion (at the inside of the can), and (3) a basic lacquer (at the outside of the can). It is expected that this approach cuts production costs and leads to a significant reduction in environmental pollution.

To efficiently optimise the can making process and attain product innovation, the use of numerical simulation is essential. The forming process is characterised by large, localised strains, the movement of free surfaces, and, due to the high production speeds, a significant thermo-mechanical coupling. To simulate the forming process, a finite element model has been developed based on an Arbitrary Lagrange Euler (ALE) description using an Operator Splitting technique (OS-ALE). After a Lagrange step, resulting in an amount of mesh distortion, the positions of nodes are adapted such that computation can be continued with a well conditioned mesh. State variables, such as stresses and plastic strains, are transported to the new mesh with the Discontinuous Galerkin (DG) method, which is an appropriate technique to transport discontinuous variables accurately.

Due to the high deformation rates in the DWI process, both metal and coating exhibit elasto-viscoplastic material behaviour. An analogous constitutive model is used to describe this behaviour: the generalised compressible Leonov model. For the metal and the polymer, a Bodner-Partom and an Eyring viscosity function are used, respectively. Material parameters are determined by tension and compression tests at high deformation speeds and under high hydrostatic pressures.

To verify the model, an experimental device has been built, in which thin strips of polymer coated sheet metal are ironed. By employing a numerical-experimental method, computed and measured global forces can be compared. Moreover, displacement fields can be measured using a digital image correlation technique and com-

pared with simulation results.

The developed and experimentally validated finite element model of the wall ironing process of polymer coated sheet metal can be used to design food and beverage cans quicker and more efficiently. Influences of critical design parameters in the process, such as die angle, material choice, deformation speed, and imposed reduction have been examined. An easily manageable set-up has been realised in which realistic experiments with respect to process conditions can be performed supporting the choice of metal, coating, and tool.

# Notation

## Quantities

$\alpha, a, A$	scalar
$A$	second order tensor
${}^4A$	fourth order tensor
$I$	second order identity tensor
${}^4I$	fourth order identity tensor
$O$	second order zero tensor

## Operations

$A^c$	conjugate or transposed
$A^{-1}$	inverse
$\text{tr}(A)$	trace
$\det(A)$	determinant
$A^d = A - \frac{1}{3}\text{tr}(A)I$	deviatoric part
$A^h = \frac{1}{3}\text{tr}(A)I$	hydrostatic part
$\tilde{A} = \det(A)^{-1/3}A$	isochoric part
$\dot{A}$	material time derivative
$AB$	dyadic product
$A \cdot B$	inner product
$A : B = \text{tr}(A \cdot B)$	double inner product
$\delta$	finite difference



# Chapter 1

## Introduction

### 1.1 General introduction

Extensive development of can making techniques and of the raw materials used in their manufacturing has taken place over the last 30 years. Considerable research effort has been put into the development of several new sophisticated drawing techniques. Most of these are now firmly established in mass production. The standard material to manufacture cans is so-called tinplate, which is essentially low carbon steel between 0.14 and 0.49 mm thick, covered with a very thin coating of pure tin. The tin layer gives the can an attractive appearance and has also tribologically favourable properties.

Since the beginning of this century three-piece cans have widely been used for packaging applications. They consist of a cylindrical body and two separate ends. In early days, these parts were soldered together, but nowadays this is done in a welding step. The ends are made from circular blanks, which are pressed into rather complex membranes. The contour consists of a countersink, expansion rings and a seaming panel. It has this shape to support internal pressure through tensile rather than bending stresses.

However, quality demands, cost considerations and convenience have led to new approaches: the Draw Redraw (DRD) and the Draw and Wall Iron (DWI) process. These techniques produce two-piece bodies, consisting of a cylindrical body and bottom end in one piece, and a separate top end. Cans used for meat spreads, snack foods, pet foods, and such (Figure 1.1) are made by the draw redraw method, while beer and beverage cans (Figure 1.2) are mostly made by the DWI process.

DRD is a forming technique in which a deep drawn cup is redrawn once or twice to one of a smaller diameter, resulting in a larger height. The advantages of the DRD can over the three-piece can are that it is free of a side seam and has only one double seam. Main disadvantage of the DRD technique is that it results in an unnecessarily thick-walled and, thus, expensive product. An interesting application with DRD products is the use of pre-lacquered plate material, thus avoiding costly and difficult



Figure 1.1. Two-piece (DRD) and three-piece tins.



Figure 1.2. Typical DWI products.

post-cleaning and spray-lacquering (Morgan, 1985).

DWI is a forming technique, where a thin metal blank is subjected to a deep draw step, followed by three wall ironing operations in a so-called bodymaker (see Figure 1.3), resulting in a thin walled, cylindrical end product with a relatively thick can end. The attainable height-to-diameter ratio is higher than in DRD products. Since the introduction of DWI cans in the late 1960's, there has been a drive to reduce the unit cost of production (Nichols *et al.*, 1995). In addition to this, there are legislative and public pressures to reduce the overall packaging volume of consumables.

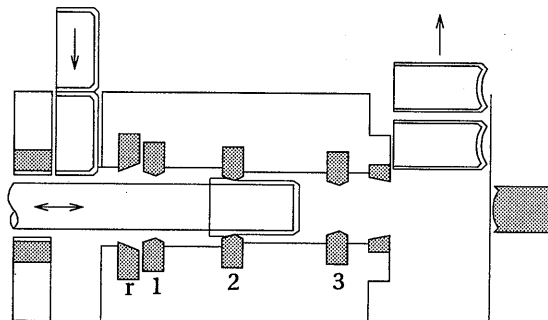


Figure 1.3. The bodymaker deforms a deep drawn cup to a can by a redraw step (r) and three wall ironing steps (1–3).

This project focusses on the DWI process for food and beverage cans. In the next section, the conventional DWI process is discussed. A new approach for this process is given in Section 1.3. In Section 1.4, the objective and the approach of this research project are given. The outline of the thesis is summarized in Section 1.5.



## 1.2 The conventional DWI process

The development of the DWI process was aimed at the production of cans with a large height-to-diameter ratio for pressurised beverages. The standard production of a DWI can consists of a number of stages (see Figure 1.5):

1. **Blanking and Drawing:** a circular blank is cut from a strip of tinplate, a controlled amount of drawing lubricant is applied, and the blank is drawn into a cup.
2. **Redraw:** the cup is redrawn to a final can diameter either in a single- or double-action press, or integrally at the beginning of the next stage (see Figure 1.3).
3. **Wall ironing:** in the bodymaker (see Figure 1.4), the wall of the cup is ironed by three or four ironing rings in a single operation, to thicknesses of approximately 35% of the original. The rings, or dies, have to be manufactured to a high precision, and carbide inserts are used to minimise wear. Emulsions are added for lubrication at each of the dies and for cooling. The typical industrial ironing velocity is 10 m/s with an output rate of 300 cans per minute.
4. **Doming:** at the end of the wall ironing operation a concave dome is formed in the base of the can by a reverse redraw operation.
5. **Trimming:** the can is trimmed to the correct height to remove an irregular rim.
6. **Washing:** the forming lubricants are washed from the can in a thorough washing step employing water-based detergents or organic solvents to ensure near absolute cleanliness, followed by a drying step using hot air.

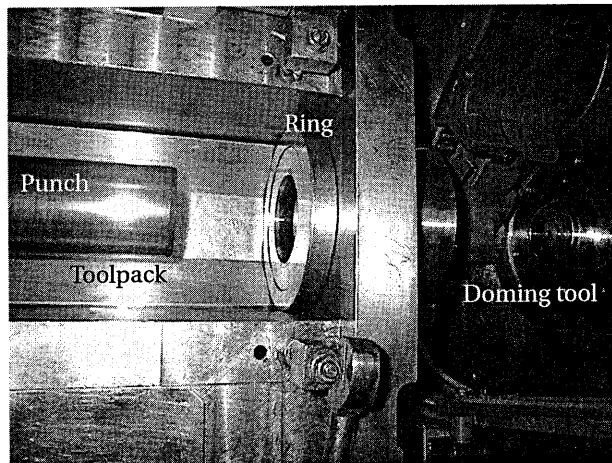


Figure 1.4. The bodymaker in which the punch moves with one ring in the toolpack. In the right part of the photograph, the doming tool is visible.

7. A basecoat is applied for improved appearance, and is cured in an oven.
8. Decorating: the desired label graphics is applied. An over-varnish application improves the can abrasion resistance and enhances can graphic quality with a glossy appearance. A coating is applied on the bottom of the can.
9. Curing: in an oven the inks and coatings are cured.
10. Necking: the top end of the can is reduced in diameter by a series of spin and or die forming operations to facilitate the use of a reduced area end closure.
11. Inside spraying: the inside coating is sprayed into the can to protect the product integrity. In case of steel cans, two 'in can' lacquering steps are necessary.
12. Curing: the inside coating is cured in an oven.
13. After transport to beverage or food manufacturers, the can is filled with food or beverage.
14. Closing: the end closure is sealed to the end of the can.
15. In case of food beverages, a pasteurisation step is needed.

To give an idea of the size of the world wide can market, an estimate of the world production per annum of metal beverage DWI cans is given in Table 1.1 (Brown and Nutting, 1997). In Europe, steel and aluminium have equal shares, but worldwide aluminium has an 84% share of DWI beverage can making capacity (Bergeson and Reiling, 1997). Apart from application in beverage cans, DWI cans are also used in packaging applications as foods, aerosols and batteries.

Part of the world	Cans in billions
The Americas	126.5
Asia and Australasia	63.7
Europe	36.6
Middle East and Africa	11.7
Total	238.5

Table 1.1. Estimated world production of DWI beverage cans (Brown and Nutting, 1997).

### 1.3 A new approach for the DWI process

Innovative can manufacturing technology focusses on the use of polymer coated sheet metal. In this so-called 'pre-finish' approach, the sheet metal is coated with a polymeric coating *before* the deformation by deep drawing and wall ironing. Instead of tinplate, Electrolytic Chromium/chromiumoxide Coated Steel (ECCS) is used. In this thesis, ECCS is simply referred to as steel. Chromiumoxide promotes adhesion between steel and polymer coating. In this approach, the mechanical behaviour of the

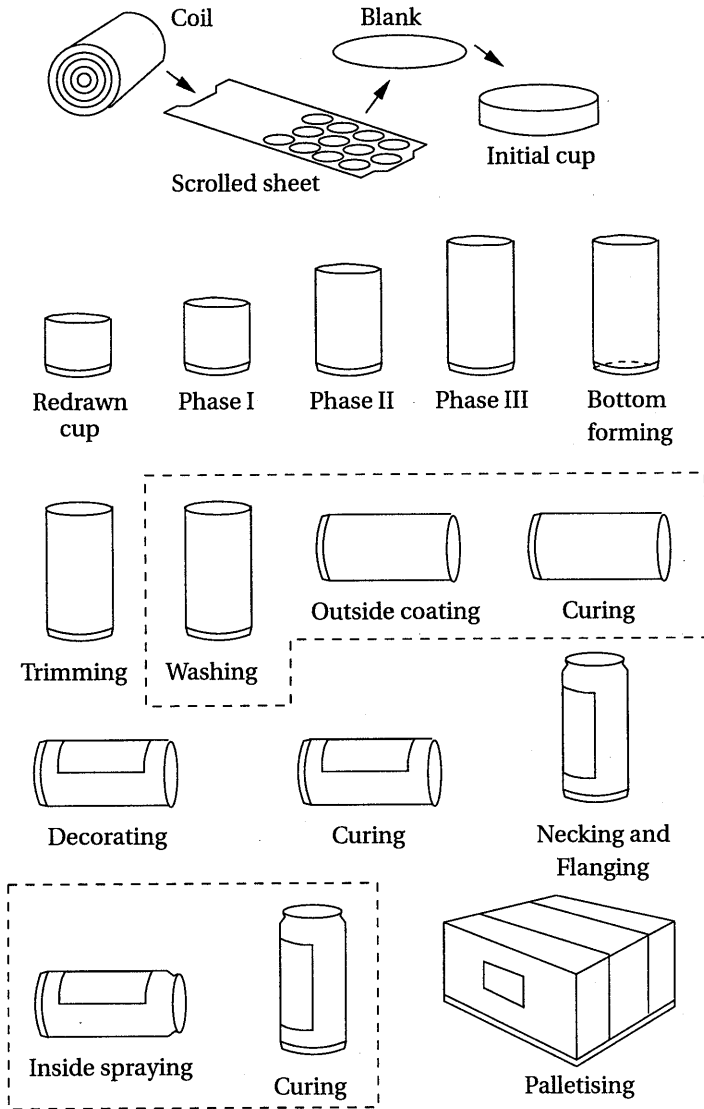


Figure 1.5. Drawing and wall ironing operation sequence (after Morgan (1985)).

coating becomes a matter of major concern as the coating has to resist the large, localised deformation. The advantages of this approach over the conventional process will be discussed.

### **Cheaper production process**

Post-lacquering of the inside and outside of the can, and subsequent curing becomes superfluous in the proposed pre-finish approach. In Figure 1.5, the obsolete process steps are given in the dashed blocks.

### **Emission-free coating**

A polymeric coating is an emission-free 'lacquer' after the forming process, which is a hot item in coating technology caused by environmental pressure aiming at zero emission. Note that in the DRD process with pre-lacquered plate still volatile solvents are emitted during curing.

### **Shorter cycle times**

The time of production will be significantly reduced by the omission of the outside and inside curing times.

This polymer coating, thus, accomplishes a number of functions: environmentally friendly lubrication, protection against corrosion, and emission-free coating. Moreover, the outside coating has an aesthetic function by ensuring the can looks appealing on the shelf.

For food packaging, a major consideration is whether the coating will impart a flavour or odour to the product or will absorb from the product. This consideration includes the factor of solvent removal as well as the cure of the coating. The Food and Drug Administration (FDA) in the United States, the European Economic Community Directives, and similar safety regulations in most countries impose strict rules on materials used for food and beverage packaging. Furthermore, coatings should be acid and sulphur resistant, and absolutely pore-free. Depending on the product packed, the coating must be able to withstand temperatures from 63 °C for 45 minutes for products such as beer, to as high as 121 °C for 90 minutes for some meat products.

When a *pre-finish* approach is used in the manufacturing process of cans, not only the FDA restrictions, but also the mechanical behaviour of the coating deserves eminent concern. In this thesis, poly(ethylene terephthalate) (PET) is considered as coating polymer. PET shows mechanical behaviour that favours its choice, such as a high glass transition temperature,  $T_g$ , a high melting temperature  $T_m$ , and a phenomenon that is termed strain induced crystallisation, which is the ability to undergo crystallisation during processing. Due to this crystallisation, the mechanical resistance to deformation increases.

## 1.4 Objective and line of research

In the past, manufacturing design was largely based on empirical knowledge. Furthermore, the evaluation of new designs is costly in terms of tooling and lead times. Fundamental insight in the process, prediction of trends resulting from changed processing conditions and variables, which dominantly influence the forming process, can be obtained using Finite Element based methods (FEM). Therefore, the objective of this research can be formulated as the development of an experimentally validated FEM simulation model for the wall ironing process of coated sheet metal. The validated model can then be used in a design environment to perform material design and process optimisation.

The success of this approach depends on the combination of numerical simulation and experimental verification. The numerical simulation of the wall ironing process must be able to analyse:

- complex material behaviour: thermo-elasto-viscoplastic material behaviour of both polymer and metal
- large, localised deformations
- moving, free boundaries
- contact and friction

The line of research is as follows: first, a FEM model has to be developed, which is able to capture the above requirements. Material parameters have to be identified. An experimental validation tool has to be built on lab-scale, which comprises the proper forming operation allowing the measurement of important quantities. Finally, experimental verification is obtained by the comparison of numerical results with measurement data on a full-size industrial forming process.

## 1.5 Outline of the thesis

In Chapter 2, a material model will be presented that can describe the material behaviour of both polymer and coating. In this chapter, also attention is paid to the determination of parameters in these constitutive models. To handle large deformations and free boundaries, an Arbitrary Lagrange Euler method (ALE) based on an Operator Splitted procedure (OS-ALE) is introduced in Chapter 3. Numerical validation has been performed to show its feasibility. Experimental and model validation of the simulation tool for the wall ironing process is described in Chapter 4. Finally, conclusions are drawn and recommendations for further research are given in Chapter 5.



# Chapter 2

## Constitutive modelling

### 2.1 Introduction

Due to the extreme processing conditions in the wall ironing process with strain rates and (true) strains, typically in the order of  $10^3 \text{ s}^{-1}$  and 1, the deforming materials behave elasto-viscoplastically. In this chapter, the generalised compressible Leonov model is presented, which is used to describe the elasto-viscoplastic behaviour of *both* polymer coating *and* metal.

First, the kinematics of the deforming continuum are given. The compressible Leonov model is described in Section 2.3. It is shown that with only a minor adaptation the elasto-viscoplastic model according to Bodner and Partom is obtained. The materials of interest in this thesis are: PET, steel and aluminium. In Section 2.4, the identification of material parameters of these materials is discussed. The numerical integration of the constitutive equations is described in Section 2.5.

### 2.2 Kinematics

The deformation of a continuum  $C$  is schematically shown in Figure 2.1. The transformation of the undeformed material  $C_o$  to its current configuration  $C_c$  is described by the deformation tensor  $F$ . The deformation tensor is defined as  $F(\vec{x}_o, \tau) = (\vec{\nabla}_o \vec{x})^c$ , where  $\vec{x}(\tau)$  is the evolving position in time  $\tau$  of an arbitrary point with reference position  $\vec{x}_o$ , and  $\vec{\nabla}_o$  is the gradient operator with respect to the reference configuration  $C_o$ . In the following, the time dependence is omitted. The multiplicative decomposition of the deformation tensor  $F$  into an elastic ( $F_e$ ) and a plastic contribution ( $F_p$ ) is assumed to exist

$$F = F_e \cdot F_p \tag{2.1}$$

This decomposition follows from Leonov's postulate of a stress-free plastic intermediate configuration  $C_p$ . As this decomposition is not unique with respect to rota-

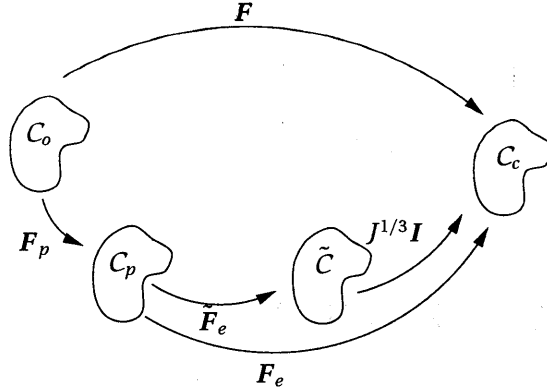


Figure 2.1. Total and relative deformation gradient tensors relating the configurations  $C_0$ ,  $C_c$ ,  $C_p$ , and  $\tilde{C}$ .

tional contributions, an extra assumption is needed regarding the rotations. Furthermore, it is assumed that during plastic deformation the volume change is zero, i.e.  $J_p = \det(\mathbf{F}_p) = 1$  and thus  $J = \det(\mathbf{F}) = \det(\mathbf{F}_e)$ . After Simo (1987), the elastic volume deformation is decoupled from the isochoric distortional deformation by the definition of the tensor  $\tilde{\mathbf{F}}_e$  according to

$$\tilde{\mathbf{F}}_e = J^{\frac{1}{3}} \mathbf{F}_e \quad (2.2)$$

The left Cauchy-Green strain tensor  $\mathbf{B} = \mathbf{F} \cdot \mathbf{F}^c$  is used as a strain measure. Its volume invariant elastic part is given by

$$\tilde{\mathbf{B}}_e = \tilde{\mathbf{F}}_e \cdot \tilde{\mathbf{F}}_e^c \quad (2.3)$$

The velocity gradient tensor  $\mathbf{L} = (\vec{\nabla} \vec{v})^c = \dot{\mathbf{F}} \cdot \mathbf{F}^{-1}$  can be written as the sum of the symmetric deformation rate tensor  $\mathbf{D}$  and the skew-symmetric spin tensor  $\mathbf{\Omega}$

$$\mathbf{L} = \mathbf{D} + \mathbf{\Omega} \quad ; \quad \mathbf{D} = \frac{1}{2}(\mathbf{L} + \mathbf{L}^c) \quad ; \quad \mathbf{\Omega} = \frac{1}{2}(\mathbf{L} - \mathbf{L}^c) \quad (2.4)$$

Using Eq. (2.1), we can split  $\mathbf{L}$  in an elastic and a plastic part

$$\mathbf{L} = \mathbf{L}_e + \mathbf{L}_p \quad ; \quad \mathbf{L}_e = \dot{\mathbf{F}}_e \cdot \mathbf{F}_e^{-1} \quad ; \quad \mathbf{L}_p = \mathbf{F}_e \cdot \dot{\mathbf{F}}_p \cdot \mathbf{F}_p^{-1} \cdot \mathbf{F}_e^{-1} \quad (2.5)$$

leading to associated tensors  $\mathbf{D}_e$ ,  $\mathbf{D}_p$ ,  $\mathbf{\Omega}_e$  and  $\mathbf{\Omega}_p$ . For a kinematical interpretation of  $\mathbf{L}_e$  and  $\mathbf{L}_p$ , usually an unloaded state or 'natural reference state' is introduced (Besseling and van der Giessen, 1994). However, the orientation of the unloaded state is irrelevant for isotropic materials. Therefore, both the elastic and plastic spin tensors are undetermined. To make the decomposition in Eq. (2.1) unique,  $\mathbf{\Omega}_p$  is chosen equal to the null tensor. It has been shown by e.g. Boyce *et al.* (1989), that this specific choice regarding rotational contributions has no significant influence on the overall stress-strain behaviour.



## 2.3 Generalised compressible Leonov model

In this section, a unified constitutive model is presented for the description of large strain, time dependent mechanical behaviour of both polymer and metal. PET is modelled with a generalised compressible Leonov model with Eyring viscosity function, whereas for aluminium and steel the same model is used with the Eyring viscosity function replaced by a Bodner-Partom viscosity function.

### 2.3.1 Compressible Leonov model with Eyring viscosity function

The generalised compressible Leonov model is a compressible generalisation of the Leonov model (Leonov, 1976), proposed by Baaijens (1991). In the Leonov model with hardening, the Cauchy stress  $\sigma$  is additively decomposed in an effective stress  $s$  and a hardening stress  $w$ , according to:

$$\sigma = s + w \quad (2.6)$$

The deviatoric part of the effective stress  $s^d$  is related to  $\tilde{B}_e^d$  through the generalised Hookean relation. The hydrostatic part  $s^h$  is coupled to the volumetric deformations (see Baaijens (1991)):

$$s^d = G\tilde{B}_e^d \quad ; \quad s^h = \kappa(J - 1)I \quad (2.7)$$

Here  $G$  represents the shear modulus,  $\kappa$  the bulk modulus, and  $I$  the unit tensor.

Hardening is modelled according to Gaussian chain statistics after Haward (1993), as this model is applicable to a large number of thermoplastic polymers, both amorphous and semi-crystalline, up to very high extension ratios. A three-dimensional generalisation of the Gaussian approach results in the neo-Hookean relation (Tervoort, 1996; Timmermans, 1997)

$$w = H\tilde{B}^d \quad (2.8)$$

where  $H$  is the hardening modulus. Crystallisation is not explicitly modelled, as it is not clear whether strain induced crystallisation of PET takes place *during* or *after* deformation in the wall ironing process of PET coated sheet metal.

As the viscoplastic model describes time- and history-dependent behaviour, the elastic (volumetric) strains must be updated by integration of appropriate evolution equations for  $\tilde{B}_e$  and  $J$ . For  $\dot{J}$  we have

$$\dot{J} = J\text{tr}(D) \quad (2.9)$$

where  $D$  is the deformation rate tensor.

The evolution equation for  $\tilde{B}_e$ , being a tensor equation, must be objective with respect to rigid material rotations. This implies that a so-called objective derivative must

be employed. Here the Truesdell time derivative is used. Using the assumption that the plastic spin tensor  $\Omega_p = \mathbf{O}$ , it can be shown (Timmermans, 1997) that the relationship between this Truesdell derivative  $\overset{\nabla}{\mathbf{B}}_e$  and the plastic deformation rate tensor  $\mathbf{D}_p$  is given by

$$\overset{\nabla}{\mathbf{B}}_e = -\mathbf{D}_p \cdot \tilde{\mathbf{B}}_e - \tilde{\mathbf{B}}_e \cdot \mathbf{D}_p \quad \text{with} \quad \overset{\nabla}{\tilde{\mathbf{B}}}_e = \dot{\tilde{\mathbf{B}}}_e - \mathbf{L}^d \cdot \tilde{\mathbf{B}}_e - \tilde{\mathbf{B}}_e \cdot (\mathbf{L}^d)^c \quad (2.10)$$

which can be used to update  $\tilde{\mathbf{B}}_e$  if, besides  $\mathbf{L}^d$ ,  $\mathbf{D}_p$  is known. This plastic deformation rate tensor is related to the deviatoric effective stress tensor  $\mathbf{s}^d$  by the viscosity  $\eta$ :

$$\mathbf{D}_p = \frac{1}{2\eta(\mathbf{s}^d, p, T, D)} \mathbf{s}^d \quad (2.11)$$

where  $p$  represents the hydrostatic pressure in the material,  $T$  is its temperature and  $D$  describes the intrinsic softening behaviour. The Eyring viscosity is specified by:

$$\eta = \frac{A\bar{\sigma}}{\sqrt{3} \sinh\left(\frac{\bar{\sigma}}{\sqrt{3}\tau_0}\right)} \quad \text{with} \quad A = A_0 \exp\left[\frac{\Delta H}{RT} + \frac{\mu p}{\tau_0} - D\right] \quad \text{and} \quad \tau_0 = \frac{RT}{V} \quad (2.12)$$

where

$$\bar{\sigma} = \sqrt{\frac{3}{2} \boldsymbol{\sigma}^d : \boldsymbol{\sigma}^d} \quad (2.13)$$

is the equivalent Von Mises stress,  $A_0$  is a time constant,  $\Delta H$  is the activation energy,  $R$  is the universal gas constant,  $T$  is the absolute temperature,  $\mu$  is a material parameter describing the pressure dependence, and  $V$  is the shear activation volume. The current value of the softening variable  $D$  is determined from the evolution equation:

$$\dot{D} = h \left(1 - \frac{D}{D_\infty}\right) \frac{\bar{\sigma}}{\sqrt{6}\eta} \quad (2.14)$$

with initial condition  $D = 0$ , and where  $h$  is the softening slope and  $D_\infty$  is the saturation value of  $D$ .

### 2.3.2 Compressible Leonov model with Bodner-Partom viscosity function

Over the past three decades, many elasto-viscoplastic constitutive models have been developed to describe rate dependent plasticity, creep, and stress relaxation of metals. Bodner and Partom (1975) presented an elasto-viscoplastic model for metals, which

has been applied to superalloys (Kolkailah and McPhate, 1990; Rowley and Thornton, 1996), aluminium alloys (Rowley and Thornton, 1996) and tin-lead alloys (i.e. solders) (Skipor *et al.*, 1996).

The model has a similar base as the compressible Leonov model. Basically, a different viscosity function is chosen, which includes strain hardening behaviour instead of an explicit hardening contribution in the constitutive equation. Again, plastic flow is modelled according to a non-Newtonian flow rule, given by:

$$\mathbf{D}_p = \frac{s^d}{2\eta(\mathbf{II}_{\mathbf{D}_p})} \quad (2.15)$$

A principal feature is the assumption that the second invariant of plastic deformation rate tensor  $\mathbf{II}_{\mathbf{D}_p} = \frac{1}{2}\mathbf{D}_p : \mathbf{D}_p$  is a function of the second invariant of the deviatoric stress. This hypothesis is partially motivated by research in dislocation dynamics, which has shown that the dislocation velocity and therefore the plastic strain rate is a function of stress. In particular forms of this relationship,  $\mathbf{II}_{\mathbf{D}_p}$ , which is a measure for the dislocation velocity, is represented as a power function or as an exponential function of the stress (Gilman, 1969). Rubin (1987) suggests the following generalised form based on the work of Bodner and Partom:

$$\mathbf{II}_{\mathbf{D}_p} = \Gamma_0 \exp\left(-\left[\frac{Z}{\bar{\sigma}}\right]^{2n}\right) \quad (2.16)$$

where  $\Gamma_0$  is a constant, which reflects the smoothness of the transition from the elastic to the (visco)plastic response,  $Z$  is the resistance to plastic flow,  $n$  is the rate sensitivity of the viscoplastic response, and  $\bar{\sigma}$  is the equivalent Von Mises stress. In accordance with the evolution equation in the original Bodner-Partom model, the following form for  $Z$  is chosen:

$$Z = Z_1 + (Z_0 - Z_1) \exp(-m\bar{\epsilon}_p) \quad (2.17)$$

where  $Z_0$  and  $Z_1$  are the lower and upper bounds of  $Z$  ( $0 < Z_0 < Z < Z_1$ ), respectively, and  $m > 0$  is a material constant controlling the rate of work hardening. The variable  $\bar{\epsilon}_p$  represents the equivalent plastic strain, which is defined by the following rate equation

$$\dot{\bar{\epsilon}}_p = \sqrt{\frac{2}{3}\mathbf{D}_p : \mathbf{D}_p} \quad (2.18)$$

Combining Eqs. (2.13), (2.15) and (2.16), the viscosity function can be written as

$$\eta = \frac{\bar{\sigma}}{\sqrt{12}\Gamma_0} \exp\left(\frac{1}{2}\left[\frac{Z}{\bar{\sigma}}\right]^{2n}\right) \quad (2.19)$$

The Bodner-Partom model corresponds to isotropic hardening and therefore does not capture the Bauschinger effect. This can be accounted for by allowing  $\mathbf{D}_p$  to alter upon a change in sign of the load direction.

## 2.4 Material parameters for the generalised compressible Leonov model

For the presented constitutive models, parameter values have to be determined. The usual strain rates to determine the parameters are in the order of  $10^{-4}$  up to  $10^{-2} \text{ s}^{-1}$ . However, in the industrial wall ironing process significantly higher strain rates occur. Moreover, high hydrostatic stresses arise in the deformation zone during this process. It is difficult to combine both a high strain rate and a high pressure in one experiment. Therefore, several different experiments are performed, yielding one set of parameters for each material fitting all experiments. In Subsection 2.4.1, the mechanical behaviour of PET is characterised. The material parameters of steel and aluminium are identified in Subsection 2.4.2.

### 2.4.1 Material parameters for PET

PET Copolyester 9921W is a thermoplastic polyester copolymer that has been modified with 1,4-cyclohexanedimethanol (CHDM) to slow the crystallisation rate. The test material has been supplied by Eastman Chemical Company, Kingsport (TN), USA. The material shows initially (visco-)elastic material behaviour, followed by yield and a substantial intrinsic softening, continued with strain hardening behaviour. Zaroulis and Boyce (1997) combined mechanical tests with the differential scanning calorimetry method (d.s.c.) to separate a contribution of molecular orientation from a strain-induced crystallisation to hardening of PET with deformation. After a coating process of the steel sheet, the PET layers are assumed to be in an amorphous state. Therefore, experiments are done with amorphous PET.

The material parameters for PET are determined in two steps: first, yielding parameters are measured by tension tests under atmospheric conditions and under superimposed pressure. Then, the softening and hardening parameters are determined by compression tests, as in tension necking results in an inhomogeneous deformation.

To determine the yielding parameters of PET, the yield stress is written as a function of these parameters. For that purpose, viscosity equation (2.12) is rewritten in terms of the equivalent Von Mises stress  $\bar{\sigma} = \sqrt{\frac{3}{2}} s^d$ ;  $s^d = 3\eta(\bar{\sigma})\dot{\epsilon}_p$ . Assuming that, at the yield point, the total equivalent strain rate  $\dot{\epsilon} = \sqrt{\frac{2}{3}} \mathbf{D} : \mathbf{D}$  is equal to the equivalent plastic strain rate  $\dot{\epsilon}_p = \sqrt{\frac{2}{3}} \mathbf{D}_p : \mathbf{D}_p$  we can write:

$$\dot{\epsilon} = \frac{1}{\sqrt{3}A_0} \sinh\left(\frac{\bar{\sigma}}{\sqrt{3}\tau_0}\right) \exp\left(-\frac{\Delta H}{RT} - \frac{\mu p}{\tau_0} + D\right) \quad (2.20)$$

This equation can be approximated by:

$$\dot{\epsilon} = \frac{1}{2\sqrt{3}A_0} \exp\left(\frac{\frac{1}{3}\sqrt{3}\bar{\sigma} - \mu p}{\tau_0} - \frac{\Delta H}{RT} + D\right) \quad (2.21)$$

where we used the approximation  $\sinh(x) = \frac{1}{2}(\exp(x) - \exp(-x)) \approx \frac{1}{2}\exp(x)$ , which is allowed as  $\tau_0$  is in the order of 1 MPa and  $\bar{\sigma}$  in the order of 10–100 MPa. In case of uniaxial tension under superimposed pressure  $p_0$ , pressure  $p$  can be written as a function of imposed uniaxial stress  $\sigma$ :

$$p = p_0 - \frac{1}{3}\sigma \quad (2.22)$$

Substitution of Eq. (2.22) into Eq. (2.21) and omission of  $D$  as no softening has developed at yield, give for the initial yield stress  $\sigma_y$ :

$$\sigma_y = \frac{3}{\sqrt{3} + \mu} \left( \tau_0 \ln(2\sqrt{3}A_0\dot{\epsilon}) + \mu p_0 + \frac{\Delta H \tau_0}{RT} \right) \quad (2.23)$$

This expression is used for fitting the experimental data up to yield.

At the Interdisciplinary Research Centre for Polymer Science and Technology (IRC) in Leeds, tensile tests have been performed under high superimposed hydrostatic pressures. The uniaxial tension tests have been carried out using a tensile device placed in a pressurised oil chamber. The maximum pressure that can be obtained is 800 MPa. In Figure 2.2, the yield stress is plotted against the imposed hydrostatic pressure for a constant clamp velocity of 2 mm/min. The initial length of a specimen is  $l_0 = 20.8$  mm, giving an imposed strain rate of approximately  $1.6 \cdot 10^{-3} \text{ s}^{-1}$ .

The measured curve can be compared with results of a study done by Christiansen *et al.* (1971). They characterised the mechanical behaviour of several polymers under high pressures, including PET. Their results are also depicted in Figure 2.2.

In Figure 2.3, the yield stresses of PET are plotted for a range of strain rates under atmospheric conditions and superimposed pressures of 300 and 600 MPa. Only a limited range of strain rates  $10^{-4} - 10^{-2} \text{ s}^{-1}$  can be covered by the tensile set-up under hydrostatic pressure. In a conventional testing machine, oscillations of the device hinder the determination of the yield stress for higher strain rates. The set of material parameters  $\{A_0, \Delta H, \mu, \tau_0\}$  have been determined using a least square fit of Eq. (2.23) for all tension experiments. The fits are also shown in Figures 2.2 and 2.3.

The softening parameters  $h$  and  $D_\infty$  and hardening parameter  $H$  are determined by compression tests with cylindrical specimens with an initial height  $h_0 = 4$  mm. The stress-strain curve is measured for three deformation velocities: 0.6, 6 and 60 mm/min. In Figure 2.4, the measurements and fits of the compression tests are shown. The constitutive model captures the severe softening after yield and subsequent hardening.

In Table 2.1, the material parameters for PET are listed. Parameters  $G$  and  $K$  have been supplied by the manufacturer.

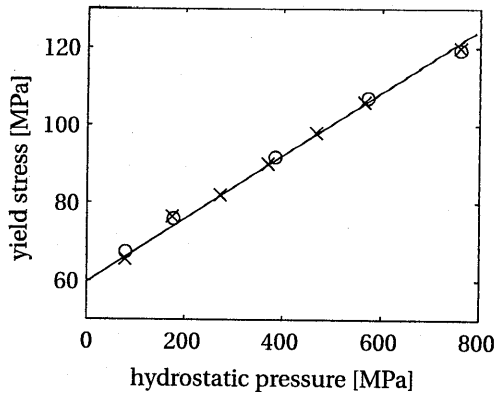


Figure 2.2. Yield stress versus hydrostatic pressure for PET. Measured data in Leeds ( $\times$ ), measured data by Christiansen *et al.* (1971) ( $\circ$ ) and fit (line) are shown.

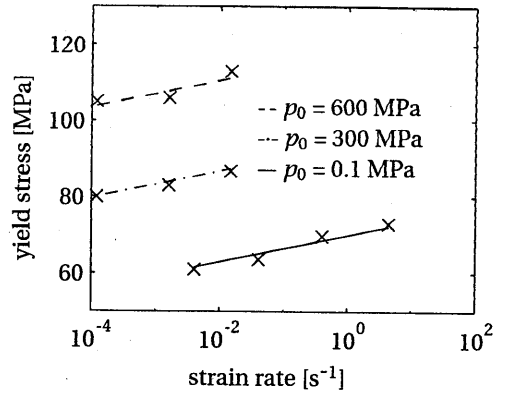


Figure 2.3. Yield stress versus strain rate for uniaxial tension tests with PET under different pressure conditions. Measured data ( $\times$ ) and results of constitutive modelling (lines) are shown.

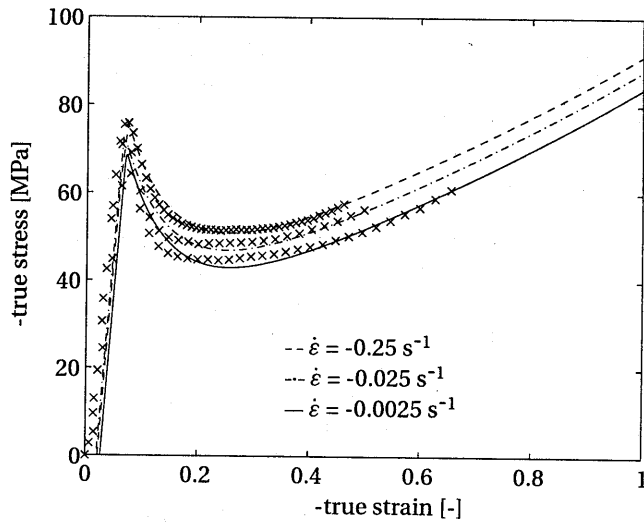


Figure 2.4. True stress versus true strain in uniaxial compression at three strain rates for PET. Experimental data ( $\times$ ) and results of constitutive modelling (lines) are shown.

parameters								
$G$	$K$	$A_0$	$\Delta H$	$\tau_0$	$\mu$	$D_\infty$	$h$	$H$
[MPa]	[MPa]	[s <sup>-1</sup> ]	[J mol <sup>-1</sup> ]	[MPa]	[-]	[-]	[-]	[MPa]
790	3670	8.1 10 <sup>-26</sup>	2.3 10 <sup>5</sup>	0.90	0.047	27.3	205	26

Table 2.1. Material parameters for PET at room temperature.

## 2.4.2 Material parameters for steel and aluminium

The material parameters in the compressible Leonov model with the Bodner-Partom viscosity are determined by uniaxial tensile tests. In uniaxial extension, the following relations hold:

$$II_{D_p} = \frac{3}{4} \dot{\epsilon}_p^2 \quad ; \quad \bar{\sigma} = \sigma \quad (2.24)$$

where  $\sigma$  is the tensile stress and  $\dot{\epsilon}_p$  is axial plastic strain rate. Substitution of these relations into Eq. (2.16), this equation can be rewritten to yield:

$$\ln \left( -\ln \left( \frac{1}{2} \sqrt{\frac{3}{\Gamma_0}} \dot{\epsilon}_p \right) \right) - 2n \ln(Z_1 + (Z_0 - Z_1) \exp(-m\bar{\epsilon}_p)) + 2n \ln(\bar{\sigma}) + \ln 2 = 0 \quad (2.25)$$

Using a least square estimator, the parameter set  $\{Z_0, Z_1, n, m\}$  are directly fitted from this relationship with the assumption that  $\dot{\epsilon} \approx \dot{\epsilon}_p$  for the range of (constant) strain rates. Parameter  $\Gamma_0$  is fixed on 10<sup>8</sup> s<sup>-2</sup>, which appears to be a universal constant for a range of metals, as reported in literature (Bodner and Partom, 1975; Rubin and Yarin, 1993; Kolkailah and McPhate, 1990; Chan *et al.*, 1988; Rowley and Thornton, 1996; Skipor *et al.*, 1996).

Two metals are considered: steel (electrolytic chromium/chromiumoxide coated steel (ECCS)) and annealed aluminium AA 1050. To determine the strain rate dependence of the steel, the material is tested up to a velocity of 1.2 m/s ( $\dot{\epsilon} = 27$  s<sup>-1</sup> with  $l_0 = 45$  mm), as shown in Figure 2.5. Note that failure behaviour is not captured in the constitutive models.

In the constitutive model for the metal, it is assumed that the material is not pressure dependent. To validate this assumption, stress-strain curves of a uniaxial tensile test under superimposed pressure are determined. In Figure 2.6, the stress-strain curves are shown at atmospheric conditions and under superimposed pressures of 200 and 600 MPa for an imposed strain rate  $\dot{\epsilon} = 7.4 \cdot 10^{-4}$  s<sup>-1</sup>. No pressure dependence is observed in the mechanical behaviour of the steel.

The aluminium samples were cut from 1 mm thick stock sheet and annealed for 2.5 hours at 350°C. The annealing allowed us to obtain a stress-strain curve up to a

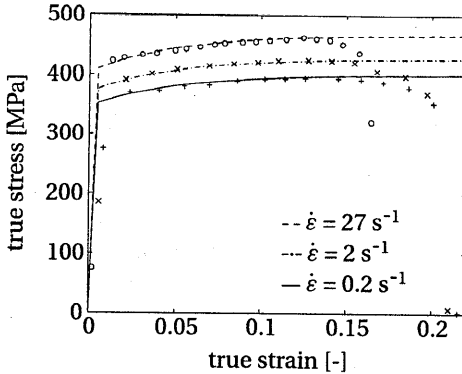


Figure 2.5. Measured and fitted stress-strain curves for tension tests at different strain rates for steel (ECCS).

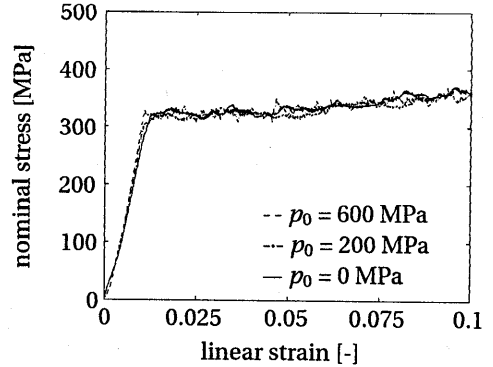


Figure 2.6. Nominal stress-strain curves for tension tests under superimposed pressure for steel (ECCS).

considerable strain, as shown in Figure 2.7. A significant influence of strain rate is visible. Again, no pressure dependence of the metal is observed in the tensile tests at a strain rate  $\dot{\epsilon} = 7.4 \cdot 10^{-4} \text{ s}^{-1}$ , see Figure 2.8.

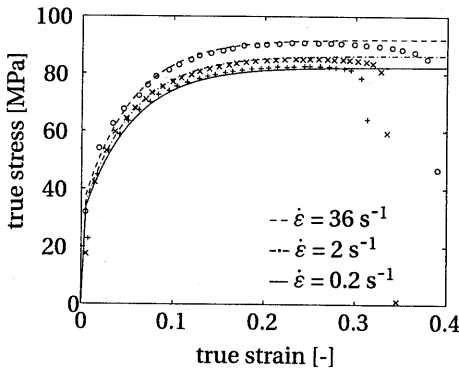


Figure 2.7. Measured and fitted stress-strain curves for tension tests at different strain rates for aluminium AA 1050.

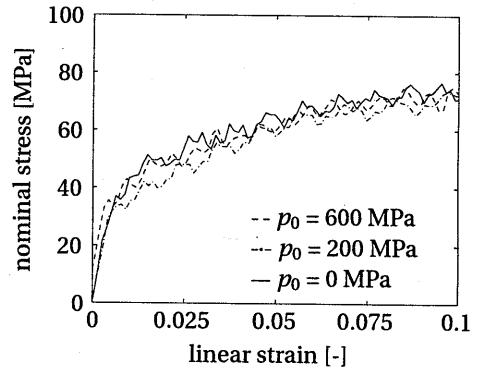


Figure 2.8. Nominal stress-strain curves for tension tests under superimposed pressure for aluminium AA 1050.

The material parameters of both steel and annealed aluminium are given in Table 2.2. Parameters  $G$  and  $K$  have been determined from measurements of the Young's modulus and the Poisson's ratio.

In this subsection, it has been shown that all materials exhibit elasto-viscoplastic material behaviour. For the polymer, also pressure dependence should be taken into account. For both metals, the assumption of pressure independent behaviour is justified up to high pressures.



	<i>parameters</i>						
	$G$ [MPa]	$K$ [MPa]	$\Gamma_0$ [s <sup>-2</sup> ]	$n$ [-]	$m$ [-]	$Z_0$ [MPa]	$Z_1$ [MPa]
steel	$7.8 \cdot 10^4$	$1.52 \cdot 10^5$	$1.0 \cdot 10^8$	1.82	20	810	930
aluminium	$2.6 \cdot 10^4$	$7.80 \cdot 10^4$	$1.0 \cdot 10^8$	3.4	13.8	81.4	170

Table 2.2. Material parameters for steel (ECCS) and aluminium at room temperature.

## 2.5 Integration of the constitutive equations

Analysis of the DWI process implies that at every moment during the deformation history, the state of the deforming material must be determined. At every moment, the state variables have to satisfy the balance equations - law of conservation of mass, of momentum, of moment of momentum -, the constitutive equations, the boundary conditions and the initial state. Certain state variables must be determined by integration of evolution equations over the total time history to determine their current value. For the generalised Leonov model with the Eyring viscosity function, the evolu-

tion equations (2.9), (2.10) and (2.14) for  $\dot{j}$ ,  $\overset{\nabla}{\mathbf{B}}_e$  and  $\dot{D}$  have to be solved in time, respectively. For the model with the Bodner-Partom viscosity function, the latter variable is replaced by Eq. (2.18) for  $\dot{\tilde{\epsilon}}_p$ .

Many constitutive models, including the Leonov model, are defined such that the elastic spin tensor equals the total spin tensor, assuming the plastic spin tensor to be zero. This implies that plastic strains are invariant: the directions of the plastic strains are not affected by rigid body rotations. Especially for large rotations this is convenient because the time derivative of the invariant plastic strains equals the material time derivative. As the time derivative of the elastic strains is not objective, another time derivative has to be used. Therefore, Rubin (Rubin, 1989; Rubin and Yarin, 1993; Rubin and Attia, 1996) proposed to rewrite the evolution equation for the objective

elastic strain  $\overset{\nabla}{\mathbf{B}}_e$  into a much more simpler evolution equation for the invariant plastic strain. For this purpose, Rubin introduced the invariant plastic right Cauchy-Green strain tensor  $\mathbf{C}_p$  and introduced the following general formulation for the constitutive evolution equation:

$$\dot{\mathbf{C}}_p = \Gamma \mathbf{A} ; \quad \Gamma = G/\eta \quad (2.26)$$

This equation states that the direction of the plastic strain rate is defined by the directional tensor  $\mathbf{A}$ , while the plastic strain rate magnitude is governed by the characteristic plastic deformation rate  $\Gamma$ . Rubin showed that this alternative formulation, in which a plastic predictor is used instead of a more common elastic predictor, resulted in a fully implicit, robustly stable and efficient time integration procedure, suitable

for numerically stiff evolution equations. In the next subsection, the compressible Leonov model will be rewritten into Rubin's formulation.

Numerical analysis implies that the state of the material is determined at a finite number of discrete moments in time:  $t_n : n = 0, 1, 2, \dots$ . The time increments  $\Delta t_n = t_{n+1} - t_n$  may have different lengths. Assuming the state at the begin increment time to be completely known - with all equations satisfied -, the goal is to determine the equilibrium state at  $t_{n+1}$ , the end of the increment. To integrate the evolution equations during the increment, some assumptions have to be made. Also reformulation of one of the evolution equations will prove to be advantageous. The incremental integration procedure is described in Subsection 2.5.2. To simplify notation, we will consider the last increment i.e.  $t_{n+1} = t$ , the current time.

### 2.5.1 The Leonov model embedded in Rubin's formulation

With the decomposition of the total isochoric deformation gradient tensor  $\tilde{\mathbf{F}}$  into an elastic and a plastic part, we can relate  $\mathbf{C}_p$  to  $\tilde{\mathbf{B}}_e$ :

$$\tilde{\mathbf{F}} = \tilde{\mathbf{F}}_e \cdot \mathbf{F}_p \rightarrow \mathbf{C}_p = \mathbf{F}_p^c \cdot \mathbf{F}_p = \tilde{\mathbf{F}}^c \cdot \tilde{\mathbf{B}}_e^{-1} \cdot \tilde{\mathbf{F}} \quad (2.27)$$

Taking the material time derivative of  $\mathbf{C}_p$  results in:

$$\dot{\mathbf{C}}_p = -\tilde{\mathbf{F}}^c \cdot \tilde{\mathbf{B}}_e^{-1} \cdot \overset{\nabla}{\tilde{\mathbf{B}}}_e \cdot \tilde{\mathbf{B}}_e^{-1} \cdot \tilde{\mathbf{F}} \quad (2.28)$$

$$\overset{\nabla}{\tilde{\mathbf{B}}}_e = -\tilde{\mathbf{F}} \cdot \mathbf{C}_p^{-1} \cdot \dot{\mathbf{C}}_p \cdot \mathbf{C}_p^{-1} \cdot \tilde{\mathbf{F}}^c \quad (2.29)$$

where  $\tilde{\mathbf{L}} = \dot{\tilde{\mathbf{L}}}^d = \dot{\tilde{\mathbf{F}}} \cdot \tilde{\mathbf{F}}^{-1}$  is used. In the compressible Leonov model,  $\overset{\nabla}{\tilde{\mathbf{B}}}_e$  is given by:

$$\overset{\nabla}{\tilde{\mathbf{B}}}_e = -2\mathbf{D}_p \cdot \tilde{\mathbf{B}}_e = -\frac{\mathbf{s}^d}{\eta} \cdot \tilde{\mathbf{B}}_e = -\frac{G}{\eta} \tilde{\mathbf{B}}_e^d \cdot \tilde{\mathbf{B}}_e \quad (2.30)$$

Combining Eqs. (2.29) and (2.30) leads to the following expression for  $\dot{\mathbf{C}}_p$ :

$$\dot{\mathbf{C}}_p = \frac{G}{\eta} \left( \tilde{\mathbf{C}} - \frac{1}{3} \text{tr}(\tilde{\mathbf{B}}_e) \mathbf{C}_p \right) \quad (2.31)$$

which is now written in the desired form  $\dot{\mathbf{C}}_p = \Gamma \mathbf{A}$ .

### 2.5.2 Incremental integration

To describe the kinematics of the incremental deformation, an updated Lagrange formulation is used, where the reference configuration is chosen to be the begin increment state, configuration  $C_n$  in Figure 2.9. The deformation tensor  $\mathbf{F}_n$  describes the

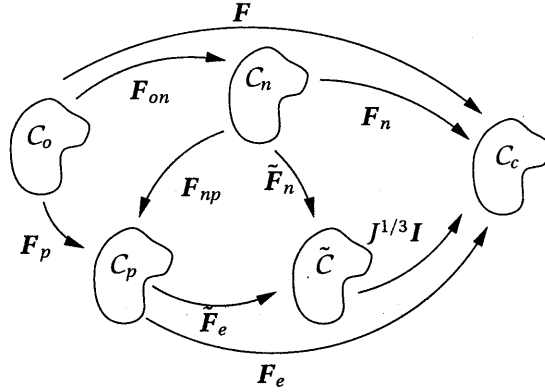


Figure 2.9. Total and relative deformation gradient tensors relating the relevant configurations.

incremental deformation and is defined by:

$$\mathbf{F}_n = \mathbf{F} \cdot \mathbf{F}_{on}^{-1} \quad (2.32)$$

In each increment, the deformation path involves large rotations and, therefore, the objectivity of the stresses must be preserved during the integration over time interval  $\Delta t_n$ . According to an integration scheme, proposed by Nagtegaal and Veldpaus (1984), the incremental rotation is separated from the incremental deformation by the polar decomposition  $\mathbf{F}_n = \mathbf{R}_n \cdot \mathbf{U}_n$ . The incremental rotation tensor is initially left out of consideration, while the rotation neutralised deformation tensor is assumed to evolve in time with a constant rotation neutralised strain rate  $\bar{\mathbf{L}} = \bar{\mathbf{L}}^c$  according to:

$$\mathbf{U}_n(\tau) = [\mathbf{U}_n] \frac{\tau - t_n}{\Delta t_n}; \quad \bar{\mathbf{L}}_n = \frac{1}{\Delta t_n} \ln(\mathbf{U}_n) \quad (2.33)$$

where the bar superscript in  $\bar{\mathbf{L}}$  denotes the rotation neutralised form of  $\mathbf{L}$ , defined as:

$$\bar{\mathbf{L}} = \mathbf{R}_n^c \cdot \mathbf{L} \cdot \mathbf{R}_n \quad (2.34)$$

The evolving  $\mathbf{U}_n(\tau)$  and  $\bar{\mathbf{L}}$  are used to integrate the tensorial state variables ( $\tilde{\mathbf{B}}_e, \sigma$ ) without considering any rotations. The rotations are incorporated afterwards using a reverse operation of Eq. (2.34).

The implementation of Rubin's formulation of the Leonov model in the updated Lagrange environment is essentially the re-definition of the incremental rotation neutralised plastic strain  $\mathbf{C}_{p_n}(\tau)$  of Eq. (2.27):

$$\mathbf{C}_{p_n}(\tau) = \tilde{\mathbf{U}}_n(\tau) \cdot \tilde{\mathbf{B}}_e^{-1}(\tau) \cdot \tilde{\mathbf{U}}_n(\tau) \quad (2.35)$$

Using  $\bar{\mathbf{L}}^d = \dot{\tilde{\mathbf{U}}}_n \cdot \tilde{\mathbf{U}}_n^{-1} = \tilde{\mathbf{U}}_n^{-1} \cdot \dot{\tilde{\mathbf{U}}}_n$ , the Rubin model in an updated Lagrange environment becomes

$$\dot{\mathbf{C}}_{p_n}(\tau) = \Gamma(\tau) \left[ \tilde{\mathbf{C}}_n(\tau) - \frac{1}{3} \text{tr}(\tilde{\mathbf{B}}_e(\tau)) \mathbf{C}_{p_n}(\tau) \right] \quad (2.36)$$

where the incremental isochoric right Cauchy-Green strain tensor  $\tilde{\mathbf{C}}_n$  is given by

$$\tilde{\mathbf{C}}_n(\tau) = \tilde{\mathbf{U}}_n(\tau) \cdot \tilde{\mathbf{U}}_n(\tau) \quad (2.37)$$

In order to calculate  $\mathbf{C}_{p_n}$ , rate equation (2.36) must be solved in time.

### Integration of $\dot{\mathbf{C}}_p$

Equation (2.36) can now be approximated by an implicit backward Euler differential scheme:

$$\mathbf{C}_{p_n}(t_{n+1}) - \mathbf{C}_{p_n}(t_n) = \Delta t_n \Gamma(t_{n+1}) \left[ \tilde{\mathbf{C}}_n(t_{n+1}) - \frac{1}{3} \text{tr}(\tilde{\mathbf{B}}_e(t_{n+1})) \mathbf{C}_{p_n}(t_{n+1}) \right] \quad (2.38)$$

Rearrangement of this expression results in the explicit relationship for  $\mathbf{C}_{p_n}(t_{n+1})$ :

$$\mathbf{C}_{p_n}(t_{n+1}) = \frac{(1 - \lambda_{n+1})}{\frac{1}{3} \text{tr}(\tilde{\mathbf{B}}_e(t_{n+1}))} \tilde{\mathbf{C}}_n(t_{n+1}) + \lambda_{n+1} \mathbf{C}_{p_n}(t_n) \quad (2.39)$$

where

$$\lambda_{n+1} = \frac{1}{1 + \frac{1}{3} \Delta t_n \Gamma(t_{n+1}) \text{tr}(\tilde{\mathbf{B}}_e(t_{n+1}))} \quad (2.40)$$

The scalar  $\lambda$  is the so-called elasticity scalar, a state variable indicating the proportion of incremental elastic/plastic strains with respect to the incremental total strains ( $\lambda = 1$ , fully elastic increment, and  $\lambda = 0$ , fully plastic increment). Using Eq. (2.35) and  $\mathbf{U}_n(t_n) = \mathbf{I}$ , we can write for  $\mathbf{C}_{p_n}(t_n)$ :

$$\mathbf{C}_{p_n}(t_n) = \tilde{\mathbf{U}}_n(t_n) \cdot \tilde{\mathbf{B}}_e^{-1}(t_n) \cdot \tilde{\mathbf{U}}_n(t_n) = \tilde{\mathbf{B}}_e^{-1}(t_n) \quad (2.41)$$

Assuming small incremental strains, the term  $\frac{1}{3} \text{tr}(\tilde{\mathbf{B}}_e(t_{n+1})) \approx 1$ , the total plastic strain becomes:

$$\mathbf{C}_{p_n}(t_{n+1}) = (1 - \lambda_{n+1}) \tilde{\mathbf{C}}_n(t_{n+1}) + \lambda_{n+1} \tilde{\mathbf{B}}_e^{-1}(t_n) \quad (2.42)$$

where  $\lambda_{n+1}$  can be solved from

$$\lambda_{n+1} (\Delta t_n \Gamma(t_{n+1}) + 1) - 1 = 0 \quad (2.43)$$

With a known  $\lambda_{n+1}$ , the deviatoric part of the Cauchy stress  $\sigma_{n+1}^d = G\tilde{\mathbf{B}}_{e_{n+1}}^d$  can be obtained by computing the plastic strain increment  $\mathbf{C}_{p_n}(t_{n+1})$  from Eq. (2.36) and the total elastic strain  $\tilde{\mathbf{B}}_{e_{n+1}}$  from

$$\tilde{\mathbf{B}}_{e_{n+1}} = \mathbf{R}_n \cdot \tilde{\mathbf{B}}_{e_{n+1}} \cdot \mathbf{R}_n^c = \tilde{\mathbf{F}}_n \cdot \mathbf{C}_{p_n}^{-1}(t_{n+1}) \cdot \tilde{\mathbf{F}}_n^c \quad (2.44)$$

where the bar transformation (2.34) and the definition of the incremental rotation neutralised plastic strain (2.35) were used.

However, according to the viscosity definitions (2.12) and (2.19) the characteristic plastic deformation rate  $\Gamma = G/\eta$  is a function of equivalent stress  $\bar{\sigma} = \sqrt{\frac{3}{2}\sigma^d : \sigma^d}$ , pressure  $p$  and -unknown- softening variable  $D$  or equivalent plastic strain  $\bar{\epsilon}_p$  for the compressible Leonov model with the Eyring or the Bodner-Partom viscosity function, respectively. Since this state variable is implicitly coupled to the unknown scalar  $\lambda$  via the equivalent stress in the evolution equation  $\dot{D}$  (2.14) or  $\dot{\bar{\epsilon}}_p$  (2.18), both this evolution equation and the scalar equation for  $\lambda$  (2.43) must be solved simultaneously in order to obtain a reliable solution.

For the compressible Leonov model with Eyring viscosity, the evolution equation is approximated with a backward Euler differential scheme:

$$\Delta t \dot{D} = D_{n+1} - D_n \quad (2.45)$$

The coupled system of equations is given by:

$$\begin{cases} f = \lambda_{n+1}(\Delta t_n \Gamma(t_{n+1}) + 1) - 1 = 0 \\ g = D_n - D_{n+1} + \Delta t_n \dot{D} = 0 \end{cases} \quad (2.46)$$

For the compressible Leonov model with Bodner-Partom viscosity, one obtains the next coupled equations after applying the same time discretisation scheme for  $\dot{\bar{\epsilon}}_p$ :

$$\begin{cases} f = \lambda_{n+1}(\Delta t_n \Gamma(t_{n+1}) + 1) - 1 = 0 \\ g = \bar{\epsilon}_{p_n} - \bar{\epsilon}_{p_{n+1}} + \Delta t_n \dot{\bar{\epsilon}}_p = 0 \end{cases} \quad (2.47)$$

The coupled systems are solved using a Newton-Raphson iteration scheme.

## 2.6 Concluding remarks

In this chapter, it is shown that it is necessary to use advanced constitutive models to capture the strain rate dependence of the materials and the pressure dependence of PET. Moreover, PET exhibits a strong strain softening after yield which is followed by considerable hardening behaviour. Compression and tension tests have been performed to identify the material parameters in the constitutive equations. The assumption that steel and aluminium behave pressure independent has been justified by tension tests under high superimposed pressure.

The outline of an efficient solution procedure for the integration of the constitutive equations has been presented. The formulation allows for a generic class of viscosity definitions, where the viscosity is assumed to be a function of the equivalent Von Mises stress, the pressure and a state variable, which has to be determined from an evolution equation.

## Chapter 3

# Operator Splitted Arbitrary Lagrange Euler method

### 3.1 Introduction

Extensive analytical work focussing on the DWI process has been done by Avitzur (1968, 1983) using the upper bound method. He examined e.g. the influence of variations of the die angle and of friction coefficients on punch force, wall stresses in the cup, and reductions in a single pass. Also the slab method has been employed to determine the *mean* stress in the wall of the can (Saito *et al.*, 1989; Kawai *et al.*, 1992). To obtain more accurate results, several authors (Odell, 1978; Huang *et al.*, 1991; Tufekci *et al.*, 1995; Schünemann *et al.*, 1996), used the finite element method based on the (updated) Lagrange formulation to simulate the (draw and) wall ironing process of blank metal. In this formulation, a grid is fixed on the material that is deformed. In that case, material points correspond to grid or mesh points. If deformations become too large, the method may fail due to mesh distortion. For the wall ironing process of polymer coated sheet metal, large deformations might occur, because the polymer coating is relatively weak compared to the metal substrate.

An Euler formulation, using a finite element mesh which is fixed in space with the material flowing through it, is not hampered by mesh distortion. This approach, however, is not very appropriate when free surface flows occur. The Arbitrary Lagrange Euler (ALE) formulation is a suitable alternative as it decouples the motion of the computational mesh from the motion of the material, see e.g. Schreurs *et al.* (1986), Liu *et al.* (1988), Huétink *et al.* (1990) and Baaijens (1993).

Globally, the ALE methods presented in literature are divided in two groups: first, the method in which material and mesh points are updated simultaneously (Schreurs *et al.*, 1986; Liu *et al.*, 1988), and, second, the approach, where the mesh points are adjusted only *after* a Lagrange step to obtain a well conditioned configuration for the next step (Huétink *et al.*, 1990; Baaijens, 1993). The latter approach is more cost effective, while results are almost the same as those of the former method.

In Section 3.2, the decoupled method, so-called Operator Splitted ALE, is elucidated. Two transport methods are discussed in Section 3.3 and, based on a performance study, a specific transport algorithm is chosen. In Section 3.4, the procedure is numerically validated with two examples.

## 3.2 Operator Splitted ALE

By employing this approach, we need to solve the balance equations using the finite element method in the Lagrange part of the procedure. In Subsection 3.2.1, this numerical procedure is addressed, which is followed by a derivation of the consistent stiffness matrix. In Subsection 3.2.3, the approach of the method is elucidated.

### 3.2.1 Numerical procedure and finite element formulation

At every time and in every material point, the balance laws representing conservation of momentum, moment of momentum and mass have to be satisfied:

$$(\vec{\nabla} \cdot \boldsymbol{\sigma}) + \vec{q} = \vec{0} \quad ; \quad \boldsymbol{\sigma} = \boldsymbol{\sigma}^c \quad ; \quad \rho J = \rho_0 \quad \forall \vec{x}, \forall \tau \leq t \quad (3.1)$$

where  $\boldsymbol{\sigma}$  is the Cauchy stress tensor and  $\vec{q}$  represents the body force per unit volume in the current state. Taking  $\tau = t$ , the current time, the volume change between  $C_0$  and  $C_c$  (see Figure 2.1) is represented by  $J = \det(\boldsymbol{F})$ , where  $\boldsymbol{F}$  is the total deformation gradient.

As described in the previous chapter, constitutive equations relate the stress  $\boldsymbol{\sigma}$  to the strain  $\vec{\boldsymbol{B}}_e$  and  $J$ . Current values of  $\vec{\boldsymbol{B}}_e$  and  $J$  can only be determined by integrating the evolution equations for  $\vec{\boldsymbol{B}}_e$  and  $J$  over the total deformation history  $t_0 \leq \tau \leq t$ . It has been explained that this integration is only possible when the total time period is subdivided into time increments. As before, we focus attention on the last increment  $n$ . It is assumed that balance and constitutive equations are satisfied at the begin increment time  $t_n$ . The configuration  $C_n$  is completely known. The state variables have to be determined such that also at the current end increment time  $t_{n+1} = t$ , balance and constitutive equations, together with appropriate boundary conditions, are satisfied.

Instead of the equilibrium equation  $(\vec{\nabla} \cdot \boldsymbol{\sigma}) + \vec{q} = \vec{0}$ , its weighted residual formulation is a more suitable starting point for the solution procedure. Introducing the weighting function  $\vec{w}$ , its weak form reads:

$$\int_{\Omega(t)} (\vec{\nabla} \vec{w})^c : \boldsymbol{\sigma} \, d\Omega = \int_{\Omega(t)} \vec{w} \cdot \vec{q} \, d\Omega + \int_{\Gamma(t)} \vec{w} \cdot \vec{p} \, d\Gamma \quad \forall \vec{w}(\vec{x}) \quad (3.2)$$

where  $\Omega(t)$  and  $\Gamma(t)$  are the current volume and surface of the material and  $\vec{p}$  represents the surface load per unit area in the current state. Using the deformation



gradient tensor  $F_n$  (see Figure 2.9), the integrals in Eq. (3.2) can be transformed to integrals taken over  $\Omega_n = \Omega(t_n)$  and  $\Gamma_n = \Gamma(t_n)$ . Also the gradient operator is transformed according to  $\vec{\nabla}(\cdot) = F_n^{-1} \cdot \vec{\nabla}_n(\cdot)$ . Writing the right-hand side, which represents the external loads on the material as  $f_{ex}(\vec{w}, \vec{q}, \vec{p})$ , we have:

$$\int_{\Omega_n} (\vec{\nabla}_n \vec{w})^c : (F_n^{-1} \cdot \sigma) \det(F_n) d\Omega_n = f_{ex}(\vec{w}, \vec{q}, \vec{p}) \quad \forall \vec{w}(\vec{x}) \quad (3.3)$$

Taking the begin increment state  $C_n$  as the reference configuration for deformation variables, is known as the updated Lagrange procedure.

Starting from the known configuration  $C_n$  at  $t = t_n$ , the above equation can be used to determine the current state  $C_c$ . Because of the large deformations occurring in the current increment and the history dependent material behaviour, the value of the state variables at the current time can not be determined directly. The well-known Newton-Raphson iteration procedure is used to determine a sequence of approximate solutions until Eq. (3.3) is satisfied to a certain degree of accuracy.

To describe the essential steps of the iteration procedure, it is assumed that an approximate state  $C_c^*$  is determined with values for  $F_n^*$ ,  $\sigma^*$  and the other state variables. The unknown current values are written as  $F_n = H \cdot F^* = (I + \delta H) \cdot F^*$  and  $\sigma = \sigma^* + \delta\sigma$ , where  $\delta(\cdot)$  indicates the difference between  $C_c^*$  and  $C_c$ , and  $\delta H = (\vec{\nabla}^* \delta \vec{x})^c$ , where  $\delta \vec{x} = \vec{u}$  is the iterative displacement. Substitution into Eq. (3.3) and some linearisation result in:

$$\int_{\Omega_n} (\vec{\nabla}_n \vec{w})^c : \left[ (F_n^*)^{-1} \cdot (I - (\vec{\nabla}^* \vec{u})^c) \cdot (\sigma^* + \delta\sigma) \right] \left( 1 + I : (\vec{\nabla}^* \vec{u})^c \right) \det(F_n^*) d\Omega_n = f_{ex}(\vec{w}, \vec{q}, \vec{p}) \quad \forall \vec{w}(\vec{x}) \quad (3.4)$$

Further linearisation with regard to the iterative changes  $\vec{u}$  and  $\delta\sigma$  results in:

$$\int_{\Omega^*} (L_w^{*c} : \sigma^* I : L_u^* + L_w^{*c} : \delta\sigma - L_w^{*c} : (\sigma^{*c} \cdot L_u^*)) d\Omega^* = f_{ex}(\vec{w}, \vec{q}, \vec{p}) - \int_{\Omega^*} L_w^{*c} : \sigma^* d\Omega^* = r^*(\vec{w}, \vec{q}, \vec{p}, \sigma^*) \quad \forall \vec{w}(\vec{x}) \quad (3.5)$$

where  $L_w^* = \vec{\nabla}^* \vec{w}$  and  $L_u^* = \vec{\nabla}^* \vec{u}$  are introduced as abbreviations. The right-hand side of this equation is the residual load, which has to become zero if all equations are satisfied at the current time. To calculate  $r^*$  and the first term in the left-hand integral, the stress  $\sigma^*(t)$  must be determined following the integration algorithm described in Chapter 2.

Eq. (3.5) is used to determine an iterative displacement  $\vec{u}$  of the material points. This, however, is only possible, when the iterative change of the stress,  $\delta\sigma$ , is expressed in  $\vec{u}$ . This relation can be written as:

$$\delta\sigma = {}^4M^* : L_u^* \quad (3.6)$$

where  ${}^4\mathbf{M}$  is a fourth-order tensor, which will be derived in the next subsection. Substitution of Eq. (3.6) into Eq. (3.5) results in:

$$\int_{\Omega^*} \left( \mathbf{L}_w^{*c} : \boldsymbol{\sigma}^* \mathbf{I} : \mathbf{L}_u^* + \mathbf{L}_w^{*c} : {}^4\mathbf{M}^* : \mathbf{L}_u^* - \mathbf{L}_w^{*c} : (\boldsymbol{\sigma}^{*c} \cdot \mathbf{L}_u^*) \right) d\Omega^* = r^*(\vec{w}, \vec{q}, \vec{p}, \boldsymbol{\sigma}^*) \quad \forall \vec{w}(\vec{x}) \quad (3.7)$$

After introduction of a suitable coordinate system, vectors and tensors can be expressed in their components with respect to the coordinate axes. These components are placed in columns as indicated below:

$$\vec{w} \rightarrow \underline{w} \quad ; \quad \vec{u} = \delta \vec{x} \rightarrow \underline{u} \quad ; \quad \boldsymbol{\sigma} \rightarrow \underline{\sigma} \quad ; \quad \vec{q} \rightarrow \underline{q} \quad ; \quad \vec{p} \rightarrow \underline{p}$$

Iteration equation (3.7) becomes

$$\int_{\Omega^*} \underline{\mathbf{L}}_w^{*T} (\underline{\boldsymbol{\sigma}}^* \underline{\mathbf{I}}^T + \underline{\mathbf{M}}^* - \underline{\boldsymbol{\Sigma}}^*) \underline{\mathbf{L}}_u^* d\Omega^* = \underline{\mathbf{r}}^*(\underline{w}, \underline{q}, \underline{p}, \underline{\boldsymbol{\sigma}}^*) \quad \forall \underline{w} \quad (3.8)$$

where  $(\underline{\cdot})^T$  denotes transposition of column  $(\underline{\cdot})$  and  $\underline{\mathbf{I}}$  is a column with 0 and 1 as entries on appropriate rows.

The scalar iteration equation (3.8) is now solved using the finite element method. Spatial discretisation implies subdivision of the volume  $\Omega^*$  into a finite number of elements  $ne$ . In every element, the unknown iterative displacement components are interpolated between their values in the element nodal points, using local coordinates  $\xi = [\xi_1, \xi_2, \xi_3]^T$  with  $-1 \leq \xi_i \leq 1$  for  $i \in \{1, 2, 3\}$ . Following Galerkin's method, displacement and weighting functions are interpolated analogously. We can write:

$$\underline{u} = \underline{\mathbf{N}}(\xi) \underline{u}^e \quad ; \quad \underline{w} = \underline{\mathbf{N}}(\xi) \underline{w}^e \quad (3.9)$$

where  $\underline{u}^e$  and  $\underline{w}^e$  are nodal point values of element  $e$  and  $\underline{\mathbf{N}}$  the shape functions. Substitution of these relations into Eq. (3.8) gives:

$$\sum_{e=1}^{ne} \underline{w}^{eT} \left[ \int_{\Omega^{e*}} \underline{\mathbf{B}}^{*T} (\underline{\boldsymbol{\sigma}}^* \underline{\mathbf{I}}^T + \underline{\mathbf{M}}^* - \underline{\boldsymbol{\Sigma}}^*) \underline{\mathbf{B}}^* d\Omega^{e*} \right] \underline{u}^e = \sum_{e=1}^{ne} \underline{w}^{eT} \underline{\mathbf{r}}^{e*} \quad \forall \underline{w}^e \quad ; \quad e = 1, \dots, ne \quad (3.10)$$

or, with introduction of the element stiffness matrix  $\underline{\mathbf{K}}^{e*}$ :

$$\sum_{e=1}^{ne} \underline{w}^{eT} \underline{\mathbf{K}}^{e*} \underline{u}^e = \sum_{e=1}^{ne} \underline{w}^{eT} \underline{\mathbf{r}}^{e*} \quad \forall \underline{w}^e \quad ; \quad e = 1, \dots, ne \quad (3.11)$$

Assembling the elements results in the algebraic equation:

$$\underline{w}^T \underline{\mathbf{K}}^* \underline{u} = \underline{w}^T \underline{\mathbf{r}}^* \quad \forall \underline{w} \quad (3.12)$$

The columns  $\underline{w}$  and  $\underline{u}$  contain all nodal point values and  $\underline{K}^*$  is the so-called tangential stiffness matrix. Because Eq. (3.12) has to be satisfied for every possible  $\underline{w}$ , the iterative nodal point displacements  $\underline{u}$  have to satisfy the next system of linear algebraic equations:

$$\underline{K}^* \underline{u} = \underline{r}^* \quad (3.13)$$

When the boundary conditions are taken into account,  $\underline{u}$  can be solved from Eq. (3.13). After calculation of the stresses and other state variables, a new approximation  $C_c^{**}$  of the current configuration  $C_c$  is known. If the residual  $\underline{r}^{**}$  is small enough, the iteration process is terminated, otherwise a new iteration step is carried out.

### 3.2.2 Consistent stiffness matrix

A fourth order Jacobian tensor  ${}^4\mathbf{S}$ , providing a linear relationship between strain variations and stress variations, is used by many implicit finite element procedures to compute a new estimation of the nodal displacements ( $\sim$ the strain field) from the error in nodal forces ( $\sim$ the error in the stress field). In an updated Lagrange environment, the Jacobian tensor relates variations of the incremental deformation tensor  $\delta F_n$  to variations of the Cauchy stress tensor  $\delta \sigma$ :

$$\delta \sigma = {}^4\mathbf{S} : \delta F_n \quad (3.14)$$

which can be rewritten in the desired form of  $\delta \sigma = {}^4\mathbf{M}^* : L_u^*$  (Eq. 3.6). A fully consistent Jacobian tensor can be derived for the generalised compressible Leonov model (Smit *et al.*, 1999). Here, the derivation is made more specific for the models presented in Chapter 2. Rubin's integration scheme in the updated Lagrange formulation, which provides a non-linear relationship between the incremental deformation gradient tensor and the total Cauchy stress tensor, is linearised at the end of the increment.

The starting point is a known incremental deformation tensor  $F_n$  (and thus incremental elongation  $\mathbf{U}_n$  and rotation  $\mathbf{R}_n$ ), the elastic strain at the beginning of the increment  $\mathbf{B}_{e_n}$ , the time increment  $\Delta t_n$ , and the associated solution in the form of the scalars  $\lambda_n$  and plastic and elastic strains  $\mathbf{C}_{p_n}(t_{n+1})$ ,  $\tilde{\mathbf{B}}_{e_{n+1}}$ . Also all other intermediate quantities (e.g.  $\Gamma_{n+1}$ ,  $\eta_{n+1}$ ) are assumed to be known before the calculation of the Jacobian matrix. In the following, the subscripts  $n$  and  $n + 1$  will be omitted for the reason of clarity.

First, only the effective stress  $\mathbf{s}$  is considered. Variation of the deviatoric part and the hydrostatic part Eq. (2.7) yields:

$$\delta \mathbf{s} = \delta \mathbf{s}^d + \delta \mathbf{s}^h = G \delta \tilde{\mathbf{B}}_e^d + \kappa \delta J I \quad (3.15)$$

The variation of  $\delta \mathbf{s}$  can be rewritten as:

$$\delta \mathbf{s} = {}^4\mathbf{S}_1 : \delta \tilde{\mathbf{B}}_e + {}^4\mathbf{S}_2 : \delta F \quad (3.16)$$

where  ${}^4S_1$  and  ${}^4S_2$  are the associated fourth order tensors for the variations of  $\tilde{\mathbf{B}}_e$  and  $\mathbf{F}$ .

The variation of the elastic strain  $\delta\tilde{\mathbf{B}}_e$  follows from the linearised version of equation (2.44):

$$\delta\tilde{\mathbf{B}}_e = \delta\tilde{\mathbf{F}} \cdot \mathbf{C}_p^{-1} \cdot \tilde{\mathbf{F}}^c - \tilde{\mathbf{F}} \cdot \mathbf{C}_p^{-1} \cdot \delta\mathbf{C}_p \cdot \mathbf{C}_p^{-1} \cdot \tilde{\mathbf{F}}^c + \tilde{\mathbf{F}} \cdot \mathbf{C}_p^{-1} \cdot \delta\tilde{\mathbf{F}}^c \quad (3.17)$$

An expression for the variation of the plastic strain increment  $\mathbf{C}_p$  can be obtained from Eq. (2.42):

$$\delta\mathbf{C}_p = (1 - \lambda)\delta\tilde{\mathbf{C}} + (\tilde{\mathbf{B}}_e^{-1}(t_n) - \tilde{\mathbf{C}})\delta\lambda \quad (3.18)$$

Using  $\tilde{\mathbf{C}} = \tilde{\mathbf{U}} \cdot \tilde{\mathbf{U}} = \tilde{\mathbf{F}}^c \cdot \tilde{\mathbf{F}}$ , we can write for  $\delta\tilde{\mathbf{C}}$ :

$$\delta\tilde{\mathbf{C}} = \delta\tilde{\mathbf{F}}^c \cdot \tilde{\mathbf{F}} + \tilde{\mathbf{F}}^c \cdot \delta\tilde{\mathbf{F}} \quad (3.19)$$

The variation of the constant initial elastic strain  $\tilde{\mathbf{B}}_e(t_n)$  is zero. Using Eq. (2.42), we can write  $\tilde{\mathbf{B}}_e^{-1}(t_n) - \tilde{\mathbf{C}} = \frac{1}{\lambda}(\mathbf{C}_p - \tilde{\mathbf{C}})$  and  $\delta\mathbf{C}_p$  becomes:

$$\delta\mathbf{C}_p = (1 - \lambda)(\delta\tilde{\mathbf{F}}^c \cdot \tilde{\mathbf{F}} + \tilde{\mathbf{F}}^c \cdot \delta\tilde{\mathbf{F}}) + \frac{1}{\lambda}(\mathbf{C}_p - \tilde{\mathbf{C}})\delta\lambda \quad (3.20)$$

Substitution of this relation into Eq. (3.17), yields for the variation of the elastic strain:

$$\delta\tilde{\mathbf{B}}_e = {}^4\mathbf{B}_1 : \delta\tilde{\mathbf{F}} + \mathbf{B}_2\delta\lambda \quad (3.21)$$

An expression for  $\delta\lambda$  is obtained by variation of Eq. (2.43) using  $\Gamma = G/\eta$ :

$$\delta\lambda = \frac{\lambda\Delta t\Gamma}{G\Delta t + \eta} \delta\eta \quad (3.22)$$

Now, a distinction is necessary between the model for the polymer and for the metal because of the different choice in viscosity definition (see Chapter 2).

### Compressible Leonov model with Eyring viscosity and strain hardening

In Appendix A, the expression for  $\delta\lambda$  is derived:

$$\delta\lambda = l_1\tilde{\mathbf{B}}_e^d : \delta\tilde{\mathbf{B}}_e + l_2\mathbf{I} : \delta\mathbf{F} \quad (3.23)$$

Substitution of this expression and  $\delta\tilde{\mathbf{F}} = {}^4\mathbf{A} : \mathbf{F}$  into the relation (3.21), yields:

$$\delta\tilde{\mathbf{B}}_e = {}^4\mathbf{B}_1 : {}^4\mathbf{A} : \delta\mathbf{F} + l_1\mathbf{B}_2\tilde{\mathbf{B}}_e^d : \delta\tilde{\mathbf{B}}_e + l_2\mathbf{B}_2\mathbf{I} : \delta\mathbf{F} \quad (3.24)$$

An explicit relationship for  $\delta\tilde{\mathbf{B}}_e$  can now be written as:

$$\delta\tilde{\mathbf{B}}_e = \left({}^4\mathbf{I} - l_1\mathbf{B}_2\tilde{\mathbf{B}}_e^d\right)^{-1} : ({}^4\mathbf{B}_1 : {}^4\mathbf{A} + l_2\mathbf{B}_2\mathbf{I}) : \delta\mathbf{F} \quad (3.25)$$

Substitution of this relation into Eq. (3.16) then yields:

$$\delta\mathbf{s} = {}^4\mathbf{S} : \delta\mathbf{F} \quad (3.26)$$

Apart from the effective stress  $\mathbf{s}$ , also the variation of the work hardening contribution  $w$  should be considered. Using  $\tilde{\mathbf{B}} = \tilde{\mathbf{F}} \cdot \tilde{\mathbf{F}}^c$ , the variation  $\delta w$  can be written as:

$$\delta w = H\left({}^4\mathbf{I} - \frac{1}{3}\mathbf{I}\mathbf{I}\right) : {}^4\mathbf{G} : \delta\tilde{\mathbf{F}} \quad (3.27)$$

with  ${}^4\mathbf{G} : \delta\tilde{\mathbf{F}} = \delta\tilde{\mathbf{F}} \cdot \tilde{\mathbf{F}}^c + \tilde{\mathbf{F}} \cdot \delta\tilde{\mathbf{F}}^c$ . Using  $\delta\tilde{\mathbf{F}} = {}^4\mathbf{A} : \mathbf{F}$ , we can write:

$$\delta w = {}^4\mathbf{H} : \delta\mathbf{F} \quad ; \quad {}^4\mathbf{H} = H\left({}^4\mathbf{I} - \frac{1}{3}\mathbf{I}\mathbf{I}\right) : {}^4\mathbf{G} : {}^4\mathbf{A} \quad (3.28)$$

Substitution of Eqs. (3.25) and (3.28) into Eq. (3.14) yields the following relationship for  $\delta\sigma$ :

$$\delta\sigma = ({}^4\mathbf{S} + {}^4\mathbf{H}) : \delta\mathbf{F} = {}^4\mathbf{S}_{EV} : \delta\mathbf{F} \quad (3.29)$$

where  ${}^4\mathbf{S}_{EV}$  is the fourth order Jacobian tensor for the compressible Leonov model with Eyring viscosity function and strain hardening.

### Compressible Leonov model with Bodner-Partom viscosity

In Appendix A, the expression for  $\delta\lambda$  is derived:

$$\delta\lambda = b_1\tilde{\mathbf{B}}_e^d : \delta\tilde{\mathbf{B}}_e \quad (3.30)$$

Following the same approach as for the compressible Leonov model with the Eyring viscosity, we can write for  $\delta\tilde{\mathbf{B}}_e$ :

$$\delta\tilde{\mathbf{B}}_e = \left({}^4\mathbf{I} - b_1\mathbf{B}_2\tilde{\mathbf{B}}_e^d\right)^{-1} : {}^4\mathbf{B}_1 : {}^4\mathbf{A} : \delta\mathbf{F} \quad (3.31)$$

Substitution of this relation in Eq. (3.16) then yields:

$$\delta\sigma = \delta\mathbf{s} = {}^4\mathbf{S}_{BP} : \delta\mathbf{F} \quad (3.32)$$

where  ${}^4\mathbf{S}_{BP}$  is the fourth order Jacobian tensor for the compressible Leonov model with Bodner-Partom viscosity function.

### 3.2.3 Configuration of OS-ALE

The Operator Splitted (OS-ALE) procedure (van der Aa *et al.*, 1997, 1998a) is implemented in the MATLAB (1996) programming environment. The finite element analysis is efficiently performed using the commercial finite element code MARC (1997). After initialisation in MATLAB, an initial mesh, consisting of coordinate positions and a connectivity, is generated and a MARC input file is written including boundary conditions and (initial) state variables. A fixed number of (updated) Lagrange increments are calculated, giving rise to a certain mesh distortion. MATLAB reads the coordinates of the deformed material and state variables  $\mathcal{S}$ . For the compressible Leonov model with Eyring viscosity and with Bodner-Partom viscosity, the state variables are given by:

$$\mathcal{S}_{EV} = \{ \tilde{\mathbf{B}}, \tilde{\mathbf{B}}_e, J, D \} \quad ; \quad \mathcal{S}_{BP} = \{ \tilde{\mathbf{B}}_e, J, \bar{\varepsilon}_p \} \quad (3.33)$$

Subsequently, the positions of nodes are adapted to preserve a well conditioned mesh. Finally, the state variables are transported to the new mesh in a transport step according to the Discontinuous Galerkin method, which will be described in the next section. This procedure is repeated until a steady state result has been obtained, when the process forces, stresses and strains no longer change. A flow scheme of the implementation is shown in Figure 3.1. MARC is used for the finite element calculation due to its capability to implement complex non-linear material behaviour using user subroutines (see Chapter 2) and to perform advanced contact analysis.

SEPMESH, which is the mesher of finite element code SEPRAN (1995), is used to create and update the finite element mesh. The mesher generates a structured mesh over the deforming domain. Edge nodes of the deforming domain have to remain on the edge, but may be re-positioned to preserve mesh quality. Inner nodes of the mesh are adapted using a smoothing algorithm, which places a node at the average position of its adjacent nodes. Certain points on the edge such as inflow and outflow boundaries must be re-positioned to their original position as they do not change in space. To control the contour of deforming domains, SEPMESH uses so-called usercurves, which contain the node sets that describe the contour edges.

### 3.3 Transport algorithms

After the generation of a new mesh, the history dependent variables have to be transported from an old, deformed mesh to this new, well conditioned mesh. However, these variables are generally discontinuous across the element edges. Several algorithms exist to perform this transport step: Local Coordinate Matching (LCM), Discontinuous Galerkin (DG), Streamline Upwind Petrov Galerkin (SUPG) (Brooks and Hughes, 1982) etc.

An important parameter in the numerical solution of convection problems is the

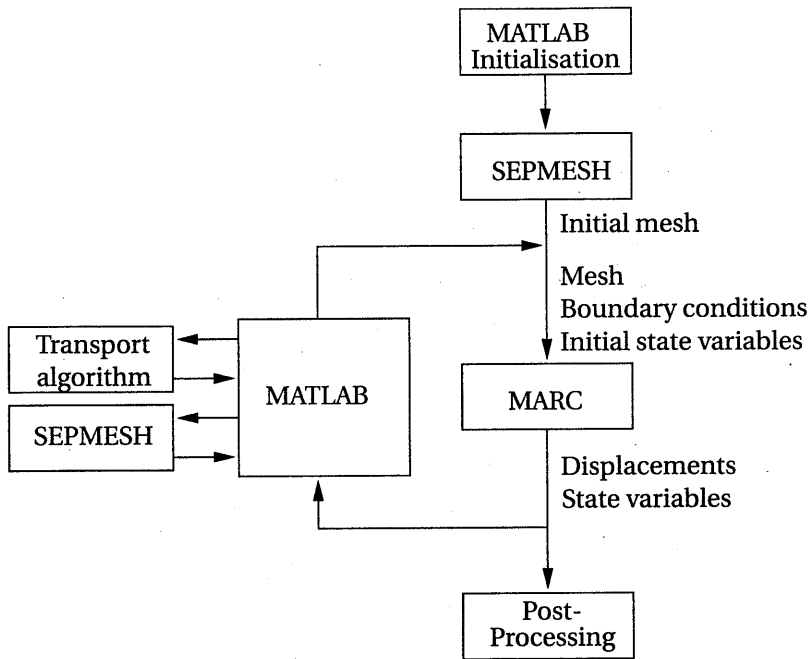


Figure 3.1. Flow scheme of Operator Splitted ALE.

Courant number  $Cr$ , given by

$$Cr \stackrel{\text{def}}{=} \frac{U}{h} \tag{3.34}$$

where  $U$  is a characteristic measure for the displacement, and  $h$  a typical element length. The Courant number and the discontinuous nature of history dependent variables across element edges, however, limit the number of suitable transport algorithms. Two transport algorithms have been investigated: the LCM and DG method, which are described in Subsections 3.3.1 and 3.3.2, respectively. The performance of the transport algorithms is evaluated in Subsection 3.3.3 for a one-dimensional and a two-dimensional test problem.

### 3.3.1 Local Coordinate Matching method

Mesh rezoning is one of the techniques to redefine the finite element mesh due to element distortion during simulation of deformation processes. Here, the rezoning

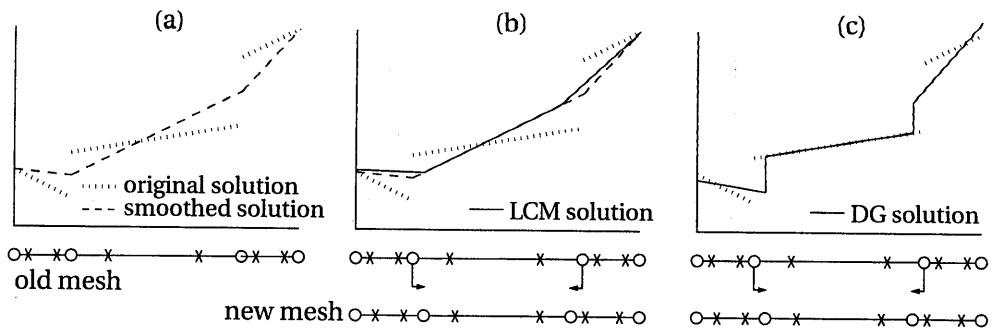


Figure 3.2. Principle of LCM method (a) and (b), and solution using DG (c).

procedure Local Coordinate Matching will be investigated. The LCM method works as follows:

- a continuous (or smoothed) field of state variables is calculated for the old element mesh by extrapolating the integration point values to node values using the element shape functions. The contributions of different elements are averaged in the nodes.
- for each node of the new mesh, the location in the old mesh is determined.
- the values in the nodes of the new mesh are determined by interpolation from the averaged nodal values using the element shape functions.

A number of procedures exist to construct a continuous field for the state variables: conjugate approximation functions (Oden and Brauchli, 1971), least square fit methods (Hinton and Campbell, 1974), local smoothing with triangularization (Gelten and de Jong, 1987) etc.

The LCM method is illustrated for a one-dimensional discontinuous solution in Figure 3.2 (a) and (b). The old mesh consists of three elements with 2 nodes (o) and 2 integration points (x). The nodes of the central element are shifted to obtain the new mesh. In Figure 3.2 (a), the smoothed solution is shown for the original field. The LCM solution is then obtained by interpolation in the nodes of the smoothed solution (Figure 3.2 (b)). This solution is continuous across the element edges.

### 3.3.2 Discontinuous Galerkin method

The Discontinuous Galerkin method takes advantage of the discontinuous character of the fields of history variables and solves the describing transport equation, yielding again a discontinuous transported solution. The determination of the field of history



variables on an updated mesh, which is a transport problem, is in several aspects similar to a convection problem. To show this similarity, the transport equation is derived from a convection problem.

A material variable  $\varphi$  is dependent on position vector  $\vec{x}$  and time  $t$ :  $\varphi(\vec{x}, t)$ . The material derivative  $\frac{D}{Dt}$  of  $\varphi$  has to equal zero:

$$\frac{D\varphi}{Dt} = 0, \quad (3.35)$$

which can be rewritten into:

$$\frac{\partial\varphi}{\partial t} + \vec{v} \cdot (\vec{\nabla}\varphi) = 0, \quad (3.36)$$

where  $\frac{\partial\varphi}{\partial t}$  is the (partial) time derivative of  $\varphi$ ,  $\vec{v}$  is the material velocity, and  $\vec{\nabla}$  is the gradient operator. A possible choice to perform a discretisation in time, is to approximate  $\frac{\partial\varphi}{\partial t}$  with an implicit Euler scheme<sup>1</sup>:

$$\frac{\varphi(\vec{x}, t_{n+1}) - \varphi(\vec{x}, t_n)}{\Delta t} + \vec{v} \cdot \vec{\nabla}\varphi(\vec{x}, t_{n+1}) = 0. \quad (3.37)$$

By multiplication of Eq. (3.37) by  $\Delta t$ , a displacement based formulation is obtained instead of a flow based one:

$$\varphi(\vec{x}, t_{n+1}) - \varphi(\vec{x}, t_n) + \vec{u} \cdot \vec{\nabla}\varphi(\vec{x}, t_{n+1}) = 0, \quad (3.38)$$

where  $\vec{u}$  is the material displacement vector in the *convection* problem. Labelling  $\varphi^a = \varphi(\vec{x}, t_n)$  and  $\varphi^b = \varphi(\vec{x}, t_{n+1})$ , the *transport* equation for state variable  $\varphi^a$  to its new value  $\varphi^b$  must be solved:

$$\varphi^b - \varphi^a - \vec{u}_m \cdot \vec{\nabla}\varphi^b = 0 \quad (3.39)$$

where  $\vec{u}_m$  is the mesh displacement and  $\vec{\nabla}$  the gradient operator. Due to finite element discretisation (see Subsection 3.2.1), the state variables become discontinuous across the element boundaries. To transport a discontinuous solution with minimal diffusion, the Discontinuous Galerkin method, introduced by Lesaint and Raviart (1974), is used to solve the transport equation (3.39). Considering the spatial domain  $\Omega$  with boundary  $\Gamma$ , the DG method is formulated as:

$$\int_{\Omega} w (\varphi^b - \varphi^a - \vec{u}_m \cdot \vec{\nabla}\varphi^b) d\Omega - \sum_{\forall e} \int_{\Gamma_e^i} w \vec{u}_m \cdot \vec{n} (\varphi^b - \varphi_{ext}^b) d\Gamma = 0 \quad \forall w \quad (3.40)$$

<sup>1</sup>Main reason for this choice is its unconditional stability and its relative simple implementation compared to higher order implicit schemes.

Here,  $w$  is a weighting function,  $\Gamma_e^i$  is the inflow boundary ( $\vec{u}_m \cdot \vec{n} > 0$ ) of an element  $e$  with outward unit normal  $\vec{n}$ , and  $\varphi_{ext}$  is the value of  $\varphi$  on the adjacent upstream side of  $\Gamma_e^i$ . In Appendix B, the DG method is derived for the one-dimensional case.

In Figure 3.2 (c), the solution using DG is given. Note that for the second element the solution matches the original solution. Moreover, the DG solution may be discontinuous over the element edges in contrast with the LCM solution.

An efficient implementation of the method has been developed by Brokken *et al.* (1998). In this implementation, variable  $\varphi_{ext}^b$  can be made explicit by using  $\varphi^b$  of the previous increment, the solution  $\varphi^b$  can be determined by an element-by-element (EBE) method (see Appendix B). To obtain sufficient accuracy, the Courant number  $Cr$  can be limited by splitting the convective step into a number of sub-increments. The accuracy of the transport step is guaranteed by imposing a desired Courant number, which leads to a number of sub-increments. In Appendix B, also the two-dimensional implementation is discussed. In the next subsection, the performance of both transport schemes are evaluated using 2 examples.

### 3.3.3 Performance of the convection schemes

The performance of the Local Coordinate Matching and the Discontinuous Galerkin method are elucidated for two specific test cases. First, a one-dimensional convection problem with large discontinuities is solved to illustrate the ability of both methods in handling them. Then, a two-dimensional Molenkamp test is considered to show the conservative quality of the methods for a smooth field, but with steep gradients in two directions.

#### 1D convection of a discontinuous field

To illustrate the influence of the Courant number for the LCM and DG method, the transport of a block function is considered. On domain  $\Omega = [0, 20]$ , 40 equally sized linear elements describe the solution  $\varphi(x) = 1$  for  $5 < x < 15$ , while  $\varphi(x) = 0$  elsewhere. The discontinuous solution is fixed and the mesh is transported with mesh displacement  $u_m = 2.8$ .

In Figures 3.3 and 3.4, the initial solution and the solution after transport with LCM and DG are shown for a corresponding Courant number  $Cr = 5.6$ . A good solution for LCM is obtained as the transported solution only shows a minor deviation in the neighbourhood of the discontinuities. A severe diffusion of the DG solution is observed. In Figures 3.5 and 3.6, the LCM and DG solutions are compared with the initial ones for Courant number  $Cr = 0.1$ . A large diffusion of the LCM solution is seen and a good preserved solution using the DG method.

Obviously, the Courant number plays an important role in the proper choice of a transport algorithm. Note that the loss of accuracy of the DG solution (see Figure 3.4) can be preserved by splitting the total transport step in 56 sub-increments, limiting the Courant number to 0.1 and giving the result as shown in Figure 3.6. In this solution,

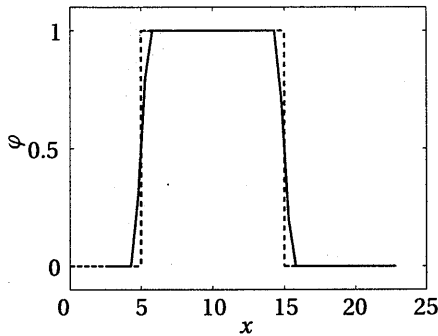


Figure 3.3. Initial (dashed) and transported (solid) solutions  $\varphi$  using LCM for Courant number 5.6.

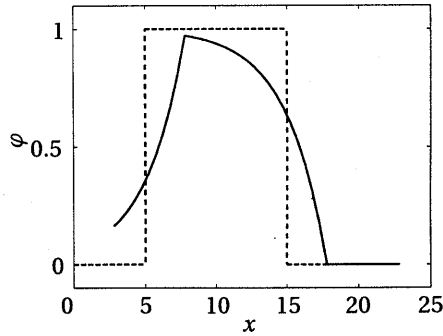


Figure 3.4. Initial (dashed) and transported (solid) solutions  $\varphi$  using DG for Courant number 5.6.

some over- and undershoot is observed. For even smaller Courant numbers, this (unwanted) effect increases, but less diffusion is observed. Therefore,  $Cr = 0.05$  is chosen based on experience and will be used in the rest of this thesis. With a known mesh displacement and element size over the entire mesh, the number of sub-increments is determined to guarantee  $Cr = 0.05$ .

In conclusion, it has been shown that Local Coordinate Matching is an appropriate transport method for large Courant numbers, and gives a diffusive solution for small Courant numbers. Discontinuous Galerkin shows the opposite behaviour of LCM: the method is diffusive for large Courant numbers and conservative for small Courant numbers. However, the numerical scheme to solve the constitutive and balance equations (see Sections 2.5 and 3.2) requires small increments to obtain convergence. Thus, the DG method will be a better method for the transport of history dependent variables.

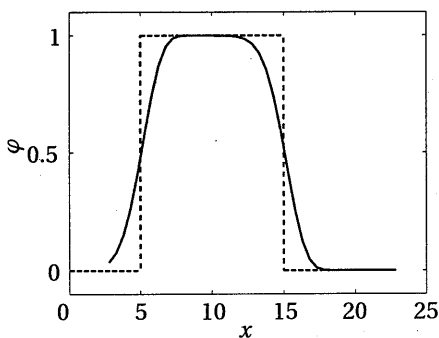


Figure 3.5. Initial (dashed) and transported (solid) solutions  $\varphi$  using LCM for Courant number 0.1.

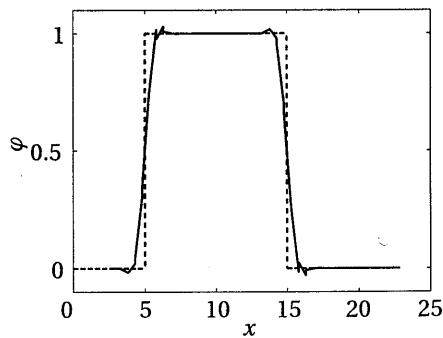
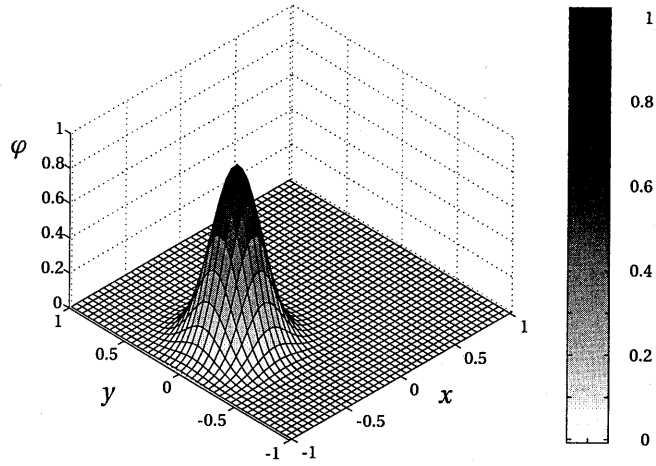


Figure 3.6. Initial (dashed) and transported (solid) solutions  $\varphi$  using DG for Courant number 0.1.

Figure 3.7. Initial field  $\varphi$ .

### 2D convection of a continuous field: Molenkamp test

The Molenkamp test is a two-dimensional test problem (Vreugdenhil and Koren, 1993) by which the performance of convection schemes can be evaluated quantitatively due to the existence of an exact solution. In the problem, a 'cloud' of material, represented by a field  $\varphi$ , is transported. The Gaussian distribution of this field is given by:

$$\varphi(x, y, t) = 0.01^{4r^2} ; r = \sqrt{\left(x + \frac{1}{2} \cos(2\pi t)\right)^2 + \left(y + \frac{1}{2} \sin(2\pi t)\right)^2} \quad (3.41)$$

where  $t \in [0 : 1]$ ,  $x \in [-1 : 1]$ , and  $y \in [-1 : 1]$ . This equation represents a (rigid) rotation of field  $\varphi$  over a fixed grid and the numerical solution is requested after one revolution, i.e.  $t=1$ . The initial distribution of  $\varphi$  is shown in Figure 3.7. Note that  $t$  only represents a pseudo time, which defines the number of steps  $1/\Delta t$  to complete a full revolution. In contrast to the standard Molenkamp test, we will rotate the grid over a fixed field  $\varphi$ .

The performance of the LCM and DG method is determined by the  $\|\cdot\|_1$  norm, the  $\|\cdot\|_\infty$  norm, and the maximum and minimum value of  $\varphi$  after transport,  $\varphi_{\max}$  and  $\varphi_{\min}$ , respectively. The norms are defined by:

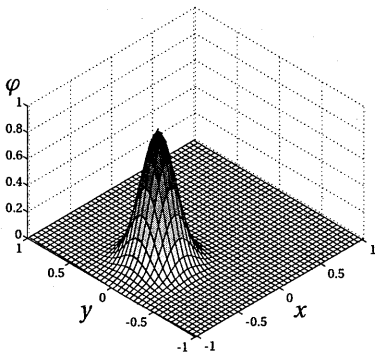
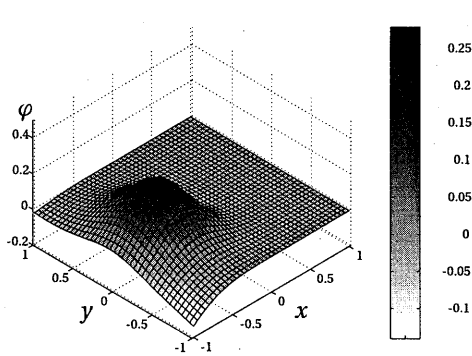
$$\|\cdot\|_1 = \frac{\sum_{i=1}^n |\varphi_{cal,i} - \varphi_{exact,i}|}{n} ; \|\cdot\|_\infty = \max_i |\varphi_{cal,i} - \varphi_{exact,i}| \quad (3.42)$$

where  $n$  is the number of nodes.

Two situations are considered: first, the performance of both methods for a subdivision of the revolution in 200 steps. Note that DG uses sub-increments to obtain a

Method(mesh,steps,sub-incs)	$\  \cdot \ _1$	$\  \cdot \ _\infty$	$\varphi_{max}$	$\varphi_{min}$
DG(20x20,200,9)	0.0127	0.3273	0.8225	-0.0341
DG(30x30,200,13)	0.0111	0.2882	0.8947	-0.0197
DG(40x40,200,18)	0.0109	0.2712	0.9369	-0.0154
DG(20x20,4000,1)	0.0060	0.1750	0.8555	-0.0288
DG(30x30,4000,1)	0.0031	0.1038	0.9288	-0.0131
DG(40x40,4000,1)	0.0016	0.0568	0.9608	-0.0089
LCM(20x20,200)	0.0460	0.8633	0.1419	-0.1501
LCM(30x30,200)	0.0402	0.7945	0.2108	-0.1483
LCM(40x40,200)	0.0355	0.7300	0.2756	-0.1316
LCM(20x20,1)	$3.76 \cdot 10^{-4}$	$1.10 \cdot 10^{-2}$	0.9966679	$-3.80 \cdot 10^{-7}$
LCM(30x30,1)	$1.03 \cdot 10^{-4}$	$2.88 \cdot 10^{-3}$	0.9985399	$-7.10 \cdot 10^{-13}$
LCM(40x40,1)	$4.20 \cdot 10^{-5}$	$1.15 \cdot 10^{-3}$	0.9997270	$-2.23 \cdot 10^{-19}$

Table 3.1. Results of the Molenkamp tests.

Figure 3.8. Transported solution  $\varphi$  for 200 steps using DG.Figure 3.9. Transported solution  $\varphi$  for 200 steps using LCM.

desired Courant number of 0.05. The results for DG and LCM method are shown in Figures 3.8 and 3.9. For LCM, a large diffusion is seen and even large negative values are obtained after transport.

Secondly, the 'optimal' performance of both methods is shown. For that purpose, DG takes 4000 steps (giving rise to one sub-increment with  $Cr = 0.05$ ) and the LCM takes one step. The results for both methods for the two situations are shown in Table 3.1. It can be seen that for DG with the  $40 \times 40$  mesh, although a similar number of total step are taken (200 steps in 18 sub-increments versus 4000 steps in 1 sub-increment), the peak value is (slightly) better conserved and significantly smaller errors are observed for the latter case. This is caused by the fact that the spatial discretisation error of (only) a linear approximation of the field  $\varphi$  is smaller for an incremental smaller displacement of the mesh.

The choice of convection scheme is dependent on the Courant number  $Cr$ . For large Courant numbers LCM performs best, while for small Courant numbers DG seems the appropriate method. For large Courant numbers, the accuracy of the solution can be preserved by splitting the total transport step in sub-increments, limiting the Courant number. In the presented OS-ALE method, the transport step is determined by the displacement in the updated Lagrange computation, which is limited due to the (strongly) non-linear constitutive behaviour of the deforming materials (see Chapter 2). The associated Courant numbers are small ( $Cr < 0.1$ ) and, therefore, the Discontinuous Galerkin method will be used to perform the convection step.

### 3.4 Validation of the method

Before starting simulations with the developed numerical tools, validation is needed by comparing the OS-ALE solution with an analytical or a Lagrange solution using the finite element package MARC. However, for many (forming) problems an analytical solution can not be derived, and accuracy of the Lagrange solution is only guaranteed for relatively small mesh distortion. In this section, two test problems are considered: (1) the backward extrusion forging problem and (2) the wall ironing of blank steel, as a first step in the direction of the industrial application of interest.

#### 3.4.1 Backward extrusion forging problem

Liu *et al.* (1988) show a number of examples to verify the quality of an Arbitrary Lagrange Euler Petrov-Galerkin method. One of the examples considers the backward extrusion forging problem. This forming problem is an illustrative example where a large deformation occurs and a moving free surface has to be tracked.

The material shows elasto-plastic behaviour with isotropic hardening. It has a Young's modulus of  $10^4$  MPa, a Poisson's ratio of 0.4, an initial yield stress of 300 MPa and a hardening modulus of 100 MPa. The initial mesh is rectangular consisting of  $20 \times 15$  linear elements (see Figure 3.10). The punch has a radius of 6.5 mm. The die and punch are assumed to be rigid. Results of the OS-ALE method can only be compared with results from the Lagrange method up to a point in the simulation where the calculation with the Lagrange method is still reliable, i.e. where the Lagrange elements show only a minor distortion. One Lagrange computation of 20 increments is performed with an incremental punch displacement of 0.2 mm. For the OS-ALE calculation, in which state  $\mathcal{S} = [\sigma, \bar{\varepsilon}_p]$  must be transported, 20 sequential computations are done of only one increment imposing a displacement of 0.2 mm.

Figure 3.11 shows that the contour of the free surface computed with OS-ALE is identical to that of the Lagrange computation. Moreover, in the neighbourhood of the punch, the OS-ALE method keeps the mesh well-conditioned in contrast with the large distorted mesh for the Lagrange computation. The load-displacement curves

are identical as shown in Figure 3.12. The computed equivalent plastic strains are compared in Figure 3.13.

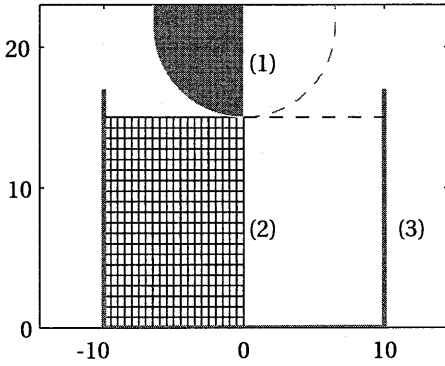


Figure 3.10. Problem description: (1) punch, (2) material and (3) die.

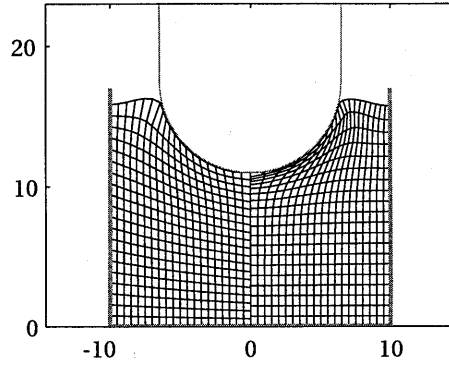


Figure 3.11. Deformed mesh of the OS-ALE method (left part) compared with the Lagrange method (right part).

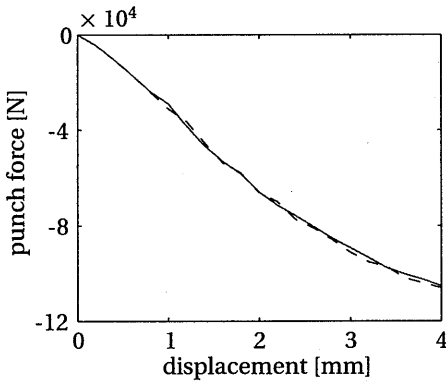


Figure 3.12. Load-displacement curve of the Lagrange method (solid) and OS-ALE method (dashed).

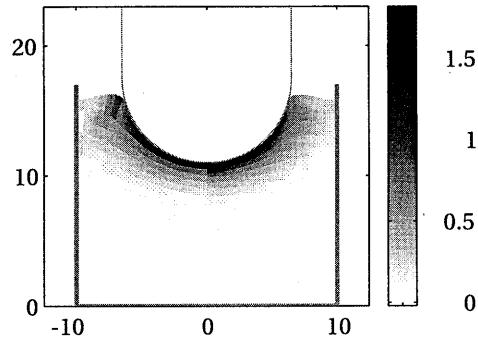


Figure 3.13. Comparison of the equivalent plastic strain for the OS-ALE method (left) and the Lagrange method (right).

### 3.4.2 Wall ironing of blank steel

The wall ironing process of blank steel is simulated using an axisymmetrical model. For the blank metal, the parameters for ECCS are used, as determined in Subsec-

tion 2.4.2. The model for the wall ironing process of blank steel is schematically depicted in Figure 3.14. For the cup, 450 (bi-)linear elements are used, after some mesh refinement trials. The moving punch and stationary ring are modelled as rigid bodies. The ring has a commonly used die angle  $\alpha = 8^\circ$  and a land zone of 0.5 mm. The imposed reduction is 29% from initial thickness  $t_0 = 0.322$  mm to  $t_f = 0.228$  and the ironing velocity is 1 m/s.

In Figure 3.15, the axial force  $F_a$  and radial force  $F_r$  on the ring evolve to steady state values in 0.7 mm punch displacement. The little spikes on the curves are caused by elements coming in contact and loosing contact with the rigid tools, and by the fact that after the transport step the system has to iterate to equilibrium again.

In Figure 3.16, the evolution of the equivalent plastic strain  $\bar{\epsilon}_p$  in time is shown. A steady state value of 0.42 is obtained. This value can be compared with an analytical solution (Avitzur, 1983) for the equivalent total strain:

$$\bar{\epsilon} = \frac{2}{\sqrt{3}} \ln(t_0/t_f) = 0.399 \quad (3.43)$$

This approximation is valid for ironing under a plane strain situation, for small angles ( $\alpha \leq 8^\circ$ ) and the neglect of friction.

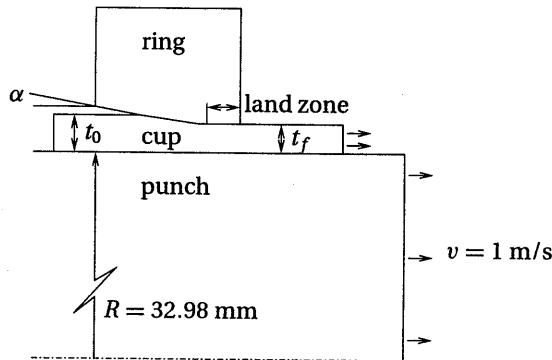


Figure 3.14. Model of the wall ironing process with blank steel.

Simulations have shown that the important variables, which influence the process characteristics, are:

- die angle  $\alpha$
- ironing velocity  $v$
- ironing reduction  $r = \frac{t_0 - t_f}{t_0}$

In Chapter 4, attention will be paid to these process variables.



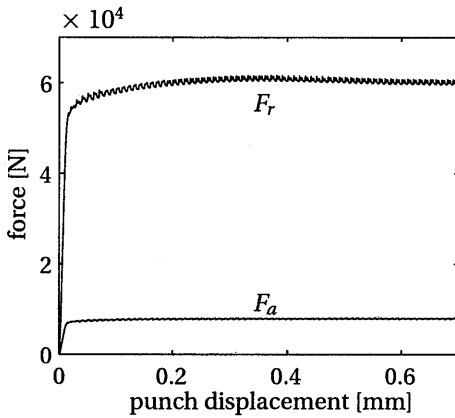


Figure 3.15. Load-displacement curves for axial force  $F_a$  and radial force  $F_r$  on the die.

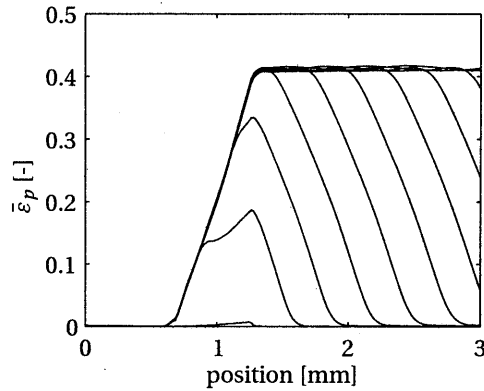


Figure 3.16. Development of the equivalent plastic strain to a steady state situation.

### 3.5 Concluding remarks

In this chapter, it has been shown that Operator Splitted ALE is an appropriate method to simulate forming processes. For the transport, the Discontinuous Galerkin method is chosen as it has proven to be the less diffusive transport method for the intended application of the method.

In the first example, the solution of OS-ALE is compared with the Lagrange solution. It has been shown that free surface motions can be tracked, while keeping the mesh well-conditioned. An identical load-displacement curve is obtained and the equivalent plastic strains compare well for a classical elasto-plastic material model.

In the second example, it is shown that OS-ALE can handle continuous processes and that the method can be combined with the elasto-viscoplastic model, which has been presented in Chapter 2.



# Chapter 4

## Experiments and model validation

### 4.1 Introduction

In this chapter, the OS-ALE method, presented in Chapter 3 is experimentally validated using the constitutive models and their parameters of Chapter 2. Two types of validation experiments are discussed. First, experiments are carried out with an in-house developed strip ironing device, which allows to perform a 'basic' ironing deformation in a setting with good accessibility for measurements and visualisation. Secondly, simulation results are compared with a full-scale experiment done at Hoogovens Research & Development, Centre for Packaging Technology, IJmuiden.

### 4.2 Strip ironing device

In this section, various experimental ironing devices are reviewed and compared. Based on the review, objectives and requirements for an experimental set-up to verify the OS-ALE simulations are formulated. The resulting experimental device is described in Subsection 4.2.2. In Subsection 4.2.4, the verification strategy is discussed. A part of the verification is addressed to displacement field measurement to obtain flow paths and strain fields, which is described in Subsection 4.2.3.

#### 4.2.1 Literature review of experimental devices

Fukui *et al.* (1962), Wilson and Cazeault (1976) and Devenpeck and Rigo (1979) developed a metal strip drawing apparatus in which a strip is ironed symmetrically through a pair of dies. The ratio of the drawing force and the die splitting force was used to calculate a process friction factor. In these three studies, it was not possible to calculate Coulomb friction coefficients nor was the strip supported by a moving punch. The friction factor at the die surface increased with increasing die angle and decreasing reduction.

Kawai *et al.* (1982a,b), Kenny and Sang (1986) and Jaworski *et al.* (1997) developed an experimental apparatus to measure the friction coefficient on the die surface in the strip ironing process. A metal strip combined with a back-up plate (punch) was pulled through a bearing and a die. Ironing travel, reduction and lubrication were varied to study their effects on the die friction coefficient, surface appearance and galling. Another non-symmetrical testing apparatus has been developed by Wang *et al.* (1986). Here, a thin strip was ironed between a die and a rotating drum. The drum torque and normal and tangential forces on the die were measured in order to calculate both the punch and die friction coefficients.

Saito *et al.* (1989) and Kawai *et al.* (1992) used a similar cup ironing device with a splitted punch in order to measure frictional forces at the punch/sheet interface. The slab method was used to calculate the friction on the die surface. Shawki (1970) studied the effects of die geometry and friction conditions on the ironing of axisymmetrical cartridge brass cups. Besides punch load and punch head load, also the tangential strain at the outer cylindrical surface of the die was measured. Using this set-up, both punch and die friction coefficients were determined.

Appleby *et al.* (1984) used transparent dies in a plane strain strip drawing apparatus in order to measure die-interface velocities. In this way, incremental displacement boundary conditions were obtained as input in a FEM analysis. Doege *et al.* (1992) and Deneuille and Lecot (1994) combined the use of strip ironing experiments and a FEM program to obtain friction coefficients for the die surface, punch surface and land zone. The experimental/numerical approach resulted in a powerful analysis tool for the wall ironing process.

Deneuille and Lecot recognised the fact that most (strip)ironing devices are operated at low speeds compared to production speeds in can making. Their set-up is able to work up to moderate speeds (up to 2 m/s), but it is hampered by alignment difficulties. A good alignment can be obtained by a construction which is loaded symmetrically.

The experimental studies discussed above are summarised in Table 4.1. Attention is paid to the following aspects:

- Measurement of tool forces in order to calculate Coulomb friction coefficients on die and punch surfaces,  $\mu_d$  and  $\mu_p$ , respectively. It is difficult to determine the right boundary conditions (i.e. friction) for the numerical simulation, except by explicitly measuring them.
- Symmetric loading of the sheet metal, which is necessary to avoid alignment problems.
- Realistic geometry and ironing speed compared to the industrial DWI process. Friction conditions and process forces are strongly dependent on the ironing velocity.
- Possibility to visualise the deformation process using a digital camera. Using

authors	$\mu_d$	$\mu_p$	moving punch	symm. design	velocity [mm/s]	visua- lisation
Fukui <i>et al.</i> (1962)	-	-	-	+	340	+
Shawki (1970)	+	+	+	+	-	-
Wilson and Cazeault (1976)	-	-	-	+	130	-
Devenpeck and Rigo (1979)	-	-	-	+	6100	+
Kawai <i>et al.</i> (1982b)	+	-	+	-	1	+
Appleby <i>et al.</i> (1984)	-	-	-	+	$8.3 \cdot 10^{-4}$	+
Wang <i>et al.</i> (1986)	+	+	+	-	530	+
Kenny and Sang (1986)	+	-	+	-	8.5	+
Saito <i>et al.</i> (1989)	+	+	+	+	1	-
Kawai <i>et al.</i> (1992)	+	+	+	+	10	-
Doege <i>et al.</i> (1992)	+	+	+	+	-	+
Deneuille and Lecot (1994)	+	+	+	-	2000	-
Jaworski <i>et al.</i> (1997)	+	-	+	-	1500	+

Table 4.1. Literature table on experimental studies in chronological order. In column two and three, the measurement of the friction coefficients on the die and punch,  $\mu_d$  and  $\mu_p$ , respectively, is symbolised by the use of the positive and negative symbols. In column four and five, it is indicated whether a moving punch and a symmetrical design is used in the experiments. Maximum ironing velocity is given in column six, and column seven indicates the *capability* of the experimental set-up to visualise the deformation process. However, not one paper actually performed the visualisation.

a two-dimensional strip ironing device with a non-moving die allows to record displacements and strains in the deformation zone.

Table 4.1 shows that the experimental set-up used by Doege *et al.* meets most of the requirements, however, no velocity is mentioned. In the next section, the strip ironing device used in this study will be discussed.

## 4.2.2 Configuration of the strip ironing device

Earlier studies of the ironing process concentrated on the influence of process parameters, such as die geometry, friction conditions, ironing travel, ironing reduction and surface appearance (see Subsection 4.2.1). In the present study, not only process forces and friction coefficients are determined, but also the deformation is investigated using a two-dimensional plane strain configuration instead of an axisymmetrical set-up.

At the Eindhoven University of Technology, an experimental device has been developed (van der Aa *et al.*, 1998b), which is schematically shown in Figure 4.1. The strip ironing device basically consists of a splitted punch (5) and two die blocks (6), sup-

ported by a frame (4). The frame is attached to the traverse of an hydraulic high-speed Zwick REL 20 kN universal testing machine. A proportional valve is used to control the volume flow rate of hydraulic fluid through the system. The maximum speed of the punch is 10 m/s, which equals speeds in industrial can making practice. The splitted punch is connected to the moving piston of the testing machine, which has a stroke of 250 mm. Rotation of the punch is suppressed by punch guide (11).

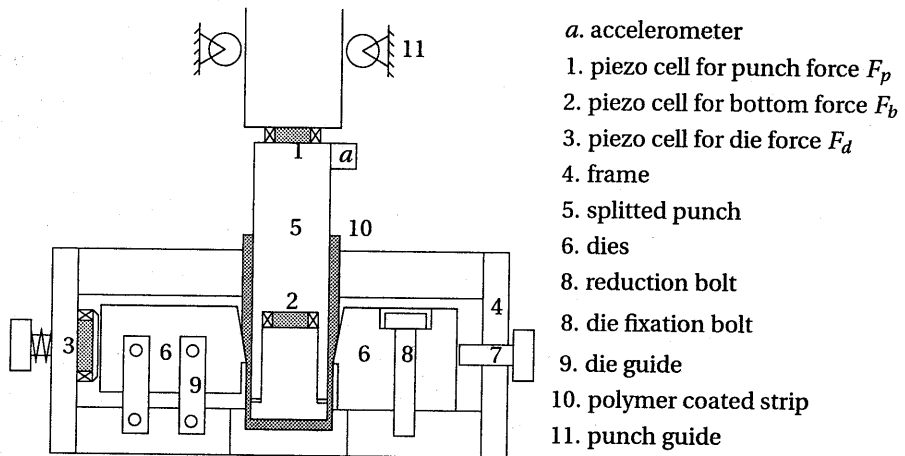


Figure 4.1. Strip ironing device.

A 300×32 mm polymer coated strip (10) is bended around the rectangular punch after which the punch is guided towards the two die blocks. During the movement of the punch between the two dies, the wall thickness of the strip is reduced. Since a relatively thin strip (thickness is 0.32 mm for PET coated steel) is used, a plane strain situation is realised in the strip. In the wall ironing process of cylindrical cups, also a plane strain situation is approximated provided that the tangential strain is small. Therefore, the strip ironing process is assumed to be a representative experiment for the wall ironing of cylindrical cups in the manufacturing of food and beverage cans. The amount of reduction is controlled by the position of the reduction bolt (7), which determines the distance between the two die blocks. Three process forces are measured using piezo-electric cells (1,2,3): the punch force  $F_p$  (20 kN, Kistler 9331A), the punch bottom force  $F_b$  (35 kN, Kistler 9021A), which is the force exerted on the nose of the punch, and the normal force  $F_d$  (60 kN, Kistler 903A) on the die. In ironing experiments with a velocity above 1 m/s, it is required to correct the measured punch forces for dynamic effects. For this purpose, an accelerometer (*a*) is attached to the punch, close to the piezo cell that measures the punch force  $F_p$ .

The position of the punch is measured using the encoder in the tensile tester. By

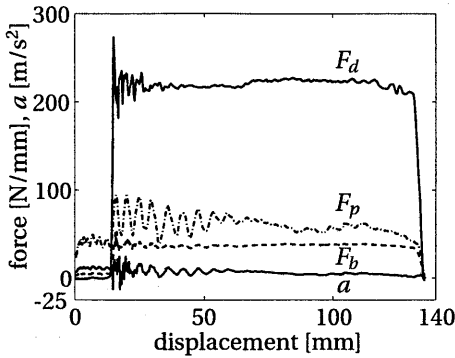


Figure 4.2. Forces and acceleration in a wall during an ironing experiment at 10 m/s.

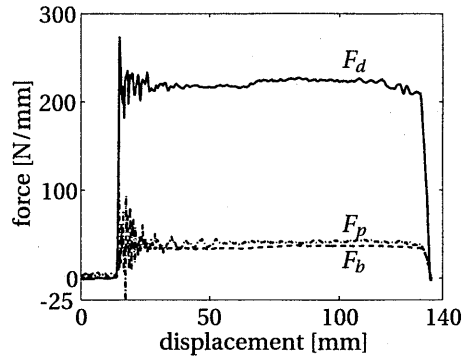


Figure 4.3. Process forces after correcting for dynamic effects.

triggering position measurements at fixed sampling rates, the velocity of the punch can be measured directly. The left die block is supported in the frame by four die guide bars (9) which ensure a nearly frictionless horizontal movement of the block. In this way, the piezo-electric load cell (3) is always properly loaded without introducing a axial force or a moment on the cell. A (small) prestress is applied on the load cell using a spring. This set-up allows rapid change of process parameters such as die angle or reduction. The dies and punch are constructed from tool steel, heat-treated to HRC 60-62 and polished to about  $0.1 \mu\text{m}$  in surface roughness Ra. No land zone is present in the geometry of the dies. Before each ironing experiment, a film of Quakerol cupping lubricant is applied to the coated strip. This semi-synthetic oil is used in its pure form, providing good lubrication during the ironing process.

Because of the high accelerations in the high speed experiments, it is required to correct the measured punch forces for dynamic effects. For this purpose, an accelerometer ( $a$ ) is attached to the punch, close to the piezo cell that measures the punch force  $F_p$ . An example of the acceleration and the three forces encountered during an ironing experiment is shown in Figure 4.2. In order to account for small variations in width of the strip, it is chosen to divide the measured force by the width  $b$ . The dimension of  $F_d$ ,  $F_p$  and  $F_b$  is N/mm. After 17 mm punch displacement, the strip first makes contact with the two dies resulting in oscillations in all transducers. Before this point, only acceleration forces are exerted on the punch load cells. The corrected process forces on the punch,  $F_{p,corr.}$  and  $F_{b,corr.}$ , are now calculated:

$$F_{p,corr.} = F_p - m_p \cdot \frac{a}{b} \quad (4.1)$$

$$F_{b,corr.} = F_b - m_b \cdot \frac{a}{b} \quad (4.2)$$

where  $m_p$  and  $m_b$  are the equivalent masses for the punch and the punch bottom, respectively, which are determined in an experiment at 10 m/s without a specimen. In that case, only acceleration forces are measured. The mass of the punch  $m_p$  is 3.29

kg and mass of bottom part of the punch  $m_b$  is 0.34 kg. Figure 4.3 shows the three process forces after accounting for dynamic effects. The acceleration forces in the first 17 mm of the stroke have disappeared and a steady state situation is reached for all forces between 70 and 110 mm. In the rest of this study, the punch forces are always corrected for dynamic effects and are referred to as  $F_p$  and  $F_b$ . In the experiments, acceleration effects become dominant at punch velocities of about 1 m/s and higher.

### 4.2.3 Displacement measurement: Digital Image Correlation

One of the experimental techniques to access kinematics of forming processes is the so-called Digital Image Correlation (DIC) method. This technique is developed at the University of South Carolina (e.g. Bruck *et al.*, 1989; Sutton *et al.*, 1986) and successfully used by Meuwissen (1998) for small deformations. The method is based on the correlation of gray values of successive digital images of undeformed and one (or more) deformed specimens. It is a versatile alternative to the placement and tracking of individual markers on a sample, which is a cumbersome and time-consuming procedure, and not always possible, for instance when examining small samples. Provided that the images have a sufficient contrast, a set of images can be processed with DIC. For the experiments, good contrast is obtained by sand blasting the surface of the specimen to remove its shiny reflections. Then, small speckles of a matt black and white paint are sprayed on the specimen.

Images of the deformation zone in the strip ironing experiment are obtained with a CCD camera (Charge Coupled Device, Philips type LDH 0703/30) and a PC controlled framegrabber. A Leica monozoom 7 lens (type 312977) is mounted on the digital camera to focus on the small deformation zone of approximately 1 mm<sup>2</sup> (see Figure 4.4). The deformation zone is illuminated by a white light source (Dedocool T2).

The Digital Image Correlation technique is based on correlation of contrast distributions between two images. The images of the specimen are stored as 400×400 sets of 8-bit numbers. Each number in this set represents the intensity of light absorbed by a small area of the camera sensor, which is referred to as a *pixel*. A value of 0 corresponds to black and a value of 255 to white and intermediate values correspond to a range of gray shades. In an image, pixels are identified by their  $(x, y)$  coordinates. The set of possible positions is denoted by:

$$I = \{(x, y) \in \mathbb{R}^2 \mid 0 \leq x \leq 400, 0 \leq y \leq 400\} \quad (4.3)$$

A pixel at the initial position  $(x_r, y_r)$  in the first image is displaced to the deformed position  $(x_d, y_d)$  in the second image as is shown in Figure 4.6. A (rectangular) subset  $\mathcal{A}_1 \in I$  is defined around  $(x_r, y_r)$  and this subset is mapped onto a subset  $\mathcal{A}_2 \in I$  in the second image. The deformation of subset  $\mathcal{A}_1$  is approximated by the first terms of a



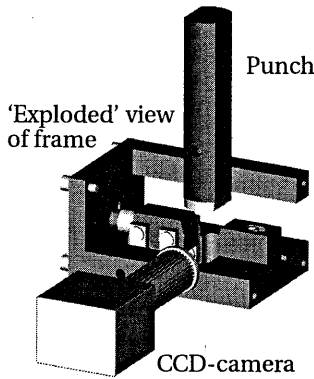


Figure 4.4. Strip ironing device with CCD-camera.

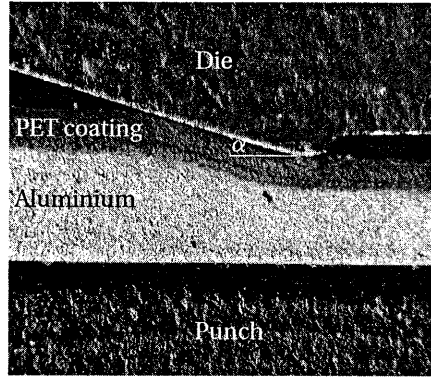


Figure 4.5. Digital image of the deformation zone during strip ironing of PET coated aluminium.

Taylor series expansion:

$$x_2 = x_1 + u + \frac{\partial u}{\partial x} \Delta x + \frac{\partial u}{\partial y} \Delta y \quad (4.4)$$

$$y_2 = y_1 + v + \frac{\partial v}{\partial x} \Delta x + \frac{\partial v}{\partial y} \Delta y \quad (4.5)$$

where  $(x_1, y_1)$  is the position of a material point in  $\mathcal{A}_1$ ,  $(x_2, y_2)$  is the position of the same point in  $\mathcal{A}_2$ ,  $u$  and  $v$  are the displacements in  $x$  and  $y$  direction at  $(x_r, y_r)$ , and  $\frac{\partial u}{\partial x}$ ,  $\frac{\partial u}{\partial y}$ ,  $\frac{\partial v}{\partial x}$ ,  $\frac{\partial v}{\partial y}$  are the displacement gradients at  $(x_r, y_r)$ . The distances  $\Delta x$  and  $\Delta y$  represent the distance from pixel  $(x_1, y_1)$  to the midpoint pixel of subset  $\mathcal{A}_1$ :

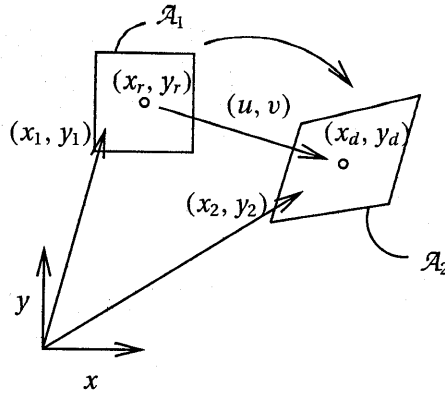
$$\Delta x = x_1 - x_r \quad ; \quad \Delta y = y_1 - y_r \quad (4.6)$$

To identify the unknown parameters  $u$ ,  $v$ ,  $\frac{\partial u}{\partial x}$ ,  $\frac{\partial u}{\partial y}$ ,  $\frac{\partial v}{\partial x}$ ,  $\frac{\partial v}{\partial y}$ , a correlation function  $r$  is introduced which correlates the gray levels in the undeformed subset  $\mathcal{A}_1$  to the gray levels in the deformed set  $\mathcal{A}_2$ :

$$r = \frac{1}{C} \int \int_{\mathcal{A}_1} a_1(x_1, y_1) a_2(x_2, y_2) dx_1 dy_1 \quad (4.7)$$

where  $a_1(x_1, y_1)$  and  $a_2(x_2, y_2)$  denote the gray values of the subsets  $\mathcal{A}_1$  and  $\mathcal{A}_2$ , respectively, and the scaling factor  $C$  is given by:

$$C = \sqrt{\int \int_{\mathcal{A}_1} a_1^2(x_1, y_1) dx_1 dy_1 \int \int_{\mathcal{A}_2} a_2^2(x_2, y_2) dx_2 dy_2} \quad (4.8)$$

Figure 4.6. Deformation of subset  $\mathcal{A}_1$ .

The correlation function  $r$  equals 1 if the gray values of the two subsets match exactly. Due to measurement and discretisation errors,  $r$  will be smaller than 1.

In practice, the gray values are discretised on the pixel level, since a pixel has a finite area and the gray value of a pixel is constant. In this discrete case, let  $\mathcal{A}_1^d \subset \mathcal{A}_1$  be the  $n \times m$  subset of integer positions  $(x_{1i}, y_{1j})$ . Then, the discrete correlation function  $r^d$  has to be maximised, which is defined by:

$$r^d = \frac{1}{C^d} \sum_{i=1}^n \sum_{j=1}^m a_1(x_{1i}, y_{1j}) a_2(x_{2i}, y_{2j}) \quad (4.9)$$

$$C^d = \sqrt{\sum_{i=1}^n \sum_{j=1}^m a_1^2(x_{1i}, y_{1j}) \sum_{i=1}^n \sum_{j=1}^m a_2^2(x_{2i}, y_{2j})} \quad (4.10)$$

with

$$x_{2i} = x_{1i} + u + \frac{\partial u}{\partial x} \Delta x_i + \frac{\partial u}{\partial y} \Delta y_j \quad (4.11)$$

$$y_{2j} = y_{1j} + v + \frac{\partial v}{\partial x} \Delta x_i + \frac{\partial v}{\partial y} \Delta y_j \quad (4.12)$$

where  $\Delta x_i$  and  $\Delta y_j$  are defined by

$$\Delta x_i = x_{1i} - x_r \quad ; \quad \Delta y_j = y_{1j} - y_r \quad (4.13)$$

The positions  $(x_{2i}, y_{2j})$  will generally not coincide with the integer position at which the second image is sampled. Therefore, the gray levels at non-integer positions are

approximated using a bicubic spline interpolation. Then, displacements can be computed with an accuracy smaller than the size of a pixel, so-called *subpixel* accuracy.

To maximise the value of the discretised correlation function  $r^d$ , a two step approach is adopted:

1. First, only the parameters  $u$  and  $v$  are determined, assuming the four displacement gradients to be zero. Then, Eqs. (4.11) and (4.12) reduce to:

$$x_{2i} = x_{1i} + u \quad (4.14)$$

$$y_{2j} = y_{1j} + v \quad (4.15)$$

and correlation function  $r^d$  becomes:

$$r^d = \frac{1}{C^d} \sum_{i=1}^n \sum_{j=1}^m a_1(x_{1i}, y_{1j}) a_2(x_{1i} + u, y_{1j} + v) \quad (4.16)$$

A very efficient manner to calculate  $r^d$  is to determine the Fourier transforms of  $a_1$  and  $a_2$ , due to the equivalence of convolution in the spatial domain and multiplication in the frequency domain.

2. Secondly, the values of  $u$  and  $v$  are used as an initial guess in the optimisation of the correlation function  $r^d$  (4.9) using Eqs. (4.11) and (4.12). For this purpose, the BFGS algorithm (Gill *et al.*, 1981) is used with as initial values of  $u$  and  $v$  the estimates obtained in the first step and the initial estimates of the displacement gradients set to zero.

The displacement of a material point can be retrieved from two images. The first image  $A$  is the reference configuration (see Figure 4.7) and image  $B$  is referred to as the deformed state of the specimen (see Figure 4.8). First, in image  $A$  a window  $A_w$  is defined around a point of interest, as shown in Figure 4.7. The pixel levels of  $A_w$  are stored in a matrix format. Now, in image  $B$  of the deformed specimen, the best match of window  $A_w$  is located in image  $B_w$ , which maximises correlation function Eq. (4.9). As a time saving measure, a search area  $S$  is defined, which covers all possible positions of the window  $B_w$ . The dimensions and location of  $S$  are chosen on the base of the maximum displacement occurring between the two images. In this study, windows of  $20 \times 20$  pixels and search areas of  $45 \times 29$  pixels are used, where the dimension of a pixel corresponds with approximately  $11 \mu\text{m}$ . The recorded ironing experiments are performed at a velocity of  $0.1 \text{ mm/s}$ , with a time difference between the two images of 1 second. This implies a displacement of about 9 pixels between image  $A$  and image  $B$ .

As the strip ironing experiment is a *steady state* forming operation, in principle, only two subsequent images should suffice to determine flow paths and strain fields. Then, the sequence described above is repeated. Therefore, the coordinates of the material point of window  $B_w$  are used in image  $A$  to define a new window  $A_w$ . Again,

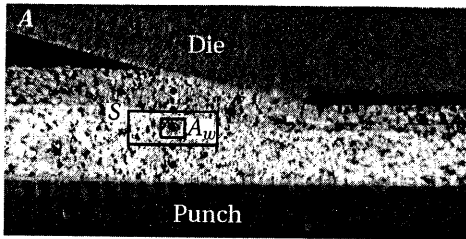


Figure 4.7. Five material points of interest are defined. A window  $A_w$  and the search area  $S$  are shown for one point.

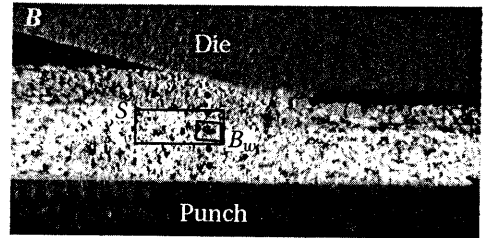


Figure 4.8. The five points are located in the deformed image. The contrast information in  $B_w$  matches matrix  $A_w$  best.

the correlation technique finds the positions of this point in image  $B$ . This procedure is repeated until the material point has reached the end of the deformation zone.

In the case that no optimum or a wrong optimum is found in the *second* step, the estimated position of step one is used to continue the process. Since this occurs in less than 5 percent of all calculations, the accuracy of the method is at least at pixel level. The accumulation of errors from image to image may reduce the maximum attainable accuracy considerably. The maximum displacement resolution depends on: the number of pixels, the size of the subset, the contrast level, the interpolation techniques, the displacement steps, etc.

To determine strain fields in the specimen, a grid of particles is followed during deformation. First, the flow paths of  $n^2$  material points, arranged in a rectangular grid of  $n \times n$  in the undeformed part of the strip, are determined using the digital image correlation method. Considering the relative change in position of all particles, an estimation for the deformation gradient tensor  $F$  can be found, using the gradient-deformation method developed by Geers *et al.* (1996). The irregularity of the grid and the existence of high strain gradients require the use of a second-order approach to minimise errors in the calculation of  $F$ . The right polar decomposition of the deformation tensor ( $F = R \cdot U$ , where  $R$  is the rotation tensor and  $U$  is the elongation tensor) is calculated in order to obtain the natural logarithmic strain field during deformation. The incremental logarithmic strain  $\Delta \epsilon$  can be calculated as

$$\Delta \epsilon = R \cdot \ln(U) \cdot R^C$$

The total logarithmic strain is obtained by adding the strain contributions of each increment. The same method is used to calculate the logarithmic strain fields from the numerically obtained displacements field.

#### 4.2.4 Numerical-experimental verification strategy

A big advantage of the strip ironing device used in this study is the possibility to calculate friction forces between the metal strip and the tools during wall ironing. A

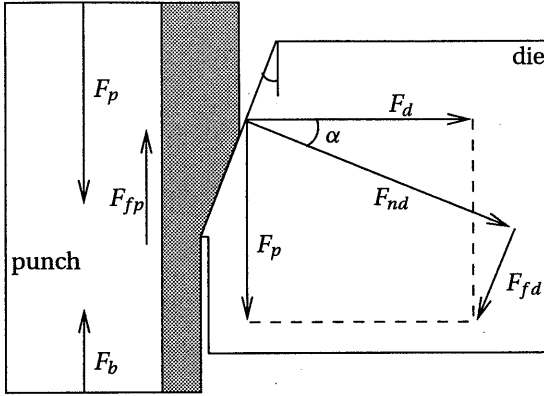


Figure 4.9. Geometric relations in strip ironing device.

Coulomb friction model is assumed, where the shear stress is proportional to the normal stress. Figure 4.9 shows the forces acting on the tools during ironing. The geometric relations for the friction coefficients are given by

$$\mu_p = \frac{F_{fp}}{F_d} = \frac{F_p - F_b}{F_d} \quad (4.17)$$

$$\mu_d = \frac{F_{fd}}{F_{nd}} = \frac{F_p \cos(\alpha) - F_d \sin(\alpha)}{F_d \cos(\alpha) + F_p \sin(\alpha)} \quad (4.18)$$

where  $\mu_p$  is the friction coefficient between punch and strip and  $\mu_d$  is the friction coefficient between die and strip. Furthermore,  $\alpha$  is the entrance angle of the die,  $F_{fp}$  and  $F_{fd}$  are the frictional forces on the punch and the die, respectively and  $F_{nd}$  is the normal force on the die surface. For the PET coated steel strip, the determination of the friction coefficient  $\mu_d$  on the die/strip interface is within the accuracy of the measuring method. The combination of small die angles, good lubrication, the favourable tribological properties of PET in combination with polished steel and the large ironing velocities results in extremely low values of  $\mu_d$ . Therefore, in the numerical simulations,  $\mu_d$  is set at 0.001, for velocities above 1 m/s. However, at lower velocities, friction increased and  $\mu_d$  can be determined accurately enough.

The wall ironing process is studied using a combined numerical-experimental approach, using the numerical procedure OS-ALE addressed in Chapter 3 including the constitutive model described in Chapter 2 and the experimental set-up described in Subsection 4.2.2. First, process forces and the punch acceleration are measured in the strip ironing device using piezo-electric cells and an acceleration transducer. The forces  $F_p$  and  $F_b$  are corrected for acceleration effects according to Eqs. (4.1) and (4.2). Steady state values of the corrected process forces are used to calculate the friction

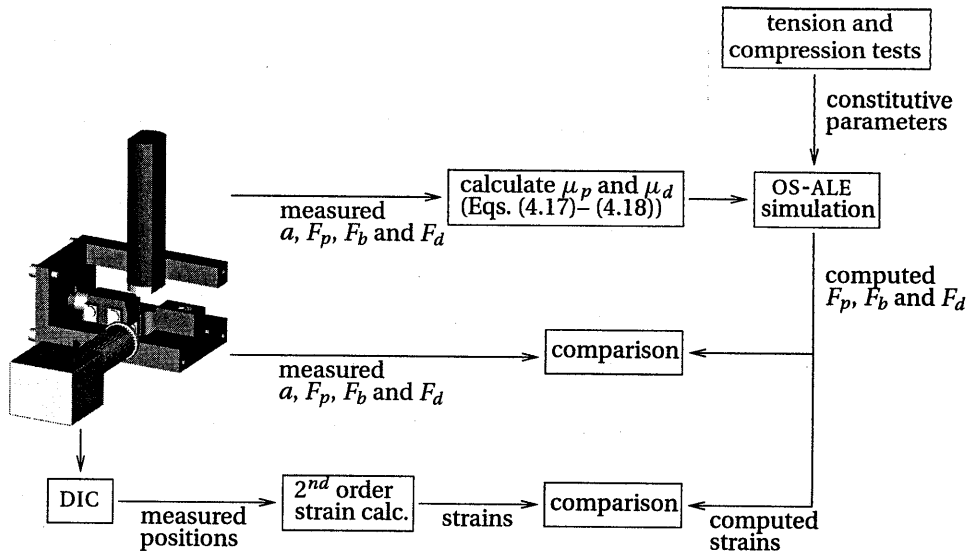


Figure 4.10. Numerical-experimental approach for the strip ironing experiment.

coefficients  $\mu_p$  and  $\mu_d$  using Eqs. (4.17) and (4.18). These friction coefficients are inserted in the OS-ALE simulation as boundary conditions for the contact bodies. Furthermore, material parameters for the sheet metal and the polymer coating are used, which have been determined in tension and compression experiments described in Chapter 2. Then, numerical simulations and experiments are compared in two ways:

- Comparing process forces measured in the strip ironing device with the forces calculated in the simulations.
- Visualising the deformation process in the experiments using the digital image correlation technique, and comparing flow paths and strain fields with the strain fields from the simulations.

The numerical-experimental strategy is illustrated in Figure 4.10.

Apart from the fact that the three forces  $F_p$ ,  $F_b$ , and  $F_d$  have to be measured for the computation of the friction coefficients, bottom force  $F_b$  and die force  $F_d$  are also interesting for other reasons. A too large bottom force  $F_b$  will result in failure of the metal in the ironed part of the strip, close to the bottom of the U-shaped strip. In the industrial cup ironing process, failure of the side wall close to the bottom of the cup limits the ongoing weight reduction of the cans. For the axisymmetric case of wall ironing, die force  $F_d$  is related to the circumferential stress present in the ring. To prevent failure of this ring, too high circumferential stresses should be avoided.

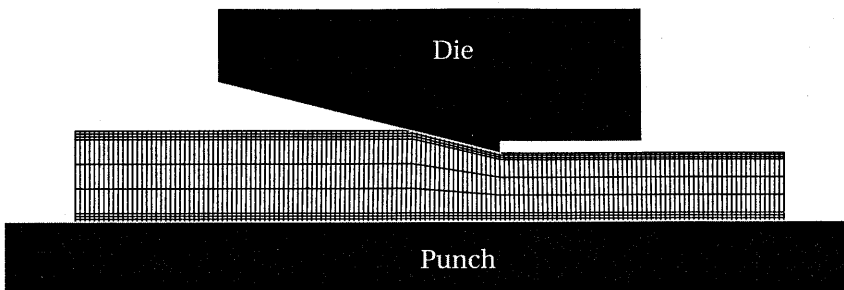


Figure 4.11. Two-dimensional, plane strain mesh used in the simulation of the wall ironing process of 0.26 mm steel, coated on both sides with a 30  $\mu\text{m}$  PET layer.

The simulation of the strip ironing process is performed using an isothermal, two-dimensional, plane strain model. Besides the deformed strip, the model geometry includes a moving punch and a stationary die, both modelled as rigid bodies. As the problem is symmetric, only one side of the strip is modelled, as shown in Figure 4.11. On the right side of the strip in Figure 4.11, an incremental displacement is prescribed, equal to the incremental displacement of the punch. For the coated specimens, perfect adhesion is assumed on the interface between metal and coating. The other boundaries are either free surfaces or in contact with rigid bodies. A total number of 1350 quadrilateral bi-linear elements with four integration points is used. To obtain sufficiently accurate simulation results, 3 elements are used through the thickness of both substrate and the coatings. To prevent locking of these elements, reduced integration is performed by using the constant dilatation option in MARC (1997).

### 4.3 Results

Following the presented approach, a comparison is made between the strip ironing experiments and the numerical simulations using the OS-ALE software. Process forces measured in the experiments are compared with the numerical predictions. In the experiments, three critical parameters, which dominate the mechanical behaviour of the materials, are varied systematically. Subsection 4.3.1 focusses on the influence of the die angle. In Subsection 4.3.2 and 4.3.3, the influence of the ironing velocity and the reduction are investigated. In the strip ironing device, 8 sets of die angles are constructed: 2, 4, 5, 6, 8, 10, 15 and 25°. The parameter study of Subsection 4.3.1–4.3.3 is performed with the PET coated steel laminate. This industrial laminate, consisting of a 0.26 mm steel substrate coated on both sides with a 30  $\mu\text{m}$  PET layer, was manufactured at Hoogovens Research & Development by sandwiching preheated ECCS between sheets of PET with two pressure rollers. The laminate is post-heated in-line

and immediately quenched, rendering the PET amorphous and yielding a strong adhesion between polymer and steel. Subsection 4.3.4 addresses the sensitivity of the equivalent strain for variations in pressure dependence and velocity in the wall ironing process of PET coated steel sheet. In Subsection 4.3.5, the PET coated aluminium sheet is used to compare the flow paths and strain fields obtained in simulations and experiments due to visualisation problems with coated steel sheet. The laminate is aluminium AA 1050 coated on one side with a 0.5 mm PET layer. It is manufactured by melting granulates in a hot press together with the 1 mm thick aluminium sheet and quenched afterwards.

### 4.3.1 Influence of die angle

The process conditions are chosen in a same order of magnitude as the settings in the industrial wall ironing process. Therefore, to investigate the influence of the die angle on the tool forces, a realistic punch velocity of 1 m/s and a reduction of 25% are applied. Figure 4.12 shows the three measured process forces for the entire range of die angles. A number of strips (between 3 and 10) are ironed to reduce the uncertainty associated with the values of the process forces. Error bars are used to indicate the 50% measuring accuracy interval. Numerical simulations are only performed for die angles of 2, 5 and 15° due to long computation times. The punch forces  $F_p$  and  $F_b$  increase only slightly with increasing die angle, while the die force  $F_d$  is strongly angle dependent: the smaller the die angle, the larger the die force  $F_d$ . In the experiments, it is observed that the PET coating survives the ironing process perfectly for die angles between 2 and 10°. However, at die angles of 15 and 25°, the coating often fails and is usually scraped from the steel substrate at the die side.

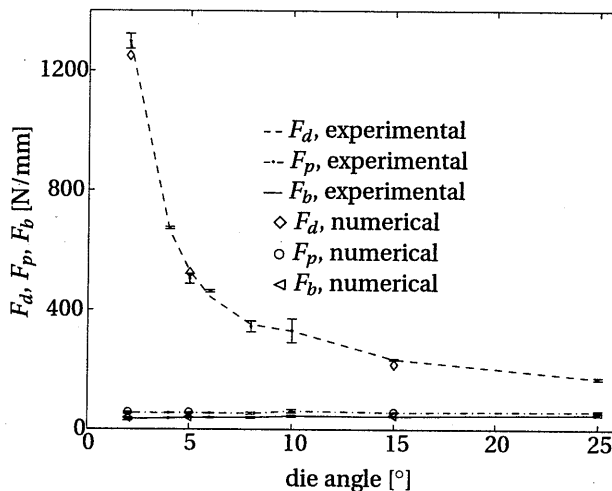


Figure 4.12. Influence of die angle on process forces.



In the development of strains during ironing, hydrostatic pressure plays an eminent role. To elucidate this influence, the pressure and the equivalent total strain  $\bar{\epsilon}$  in the upper PET coating, and the equivalent plastic strain  $\bar{\epsilon}_p$  in the steel, are computed. In Figure 4.13, these quantities are shown as a function of the position in the deformation zone relative to the die outlet. The equivalent strain  $\bar{\epsilon}$  is defined as

$$\bar{\epsilon} = \sqrt{\frac{2}{3}(\epsilon_{xx}^2 + \epsilon_{yy}^2 + 2\epsilon_{xy}^2)} \tag{4.19}$$

For die angles of 2 and 5°, pressure is built up over a large region, resulting in a block shaped pressure curve. An extreme high peak pressure of almost 800 MPa is computed for a die angle of 15°. At a 2° die angle,  $\bar{\epsilon}$  of PET initially develops quickly and subsequently increases slowly to a maximum of 0.43 at the outlet of the die. Once the strip leaves the deformation zone, the elastic contribution in the equivalent total strain is released. At 5°, a slightly higher strain for PET is found. For 15°, a strong increase in  $\bar{\epsilon}$  is seen at the end of the deformation zone, to a maximum of 1.2. After releasing the elastic strain, an equivalent total strain of 0.75 is maintained, which intuitively corresponds to the often observed failure of the coating at this die angle. As may be expected, the equivalent plastic strain  $\bar{\epsilon}_p$  in the steel hardly changes for the three die angles.

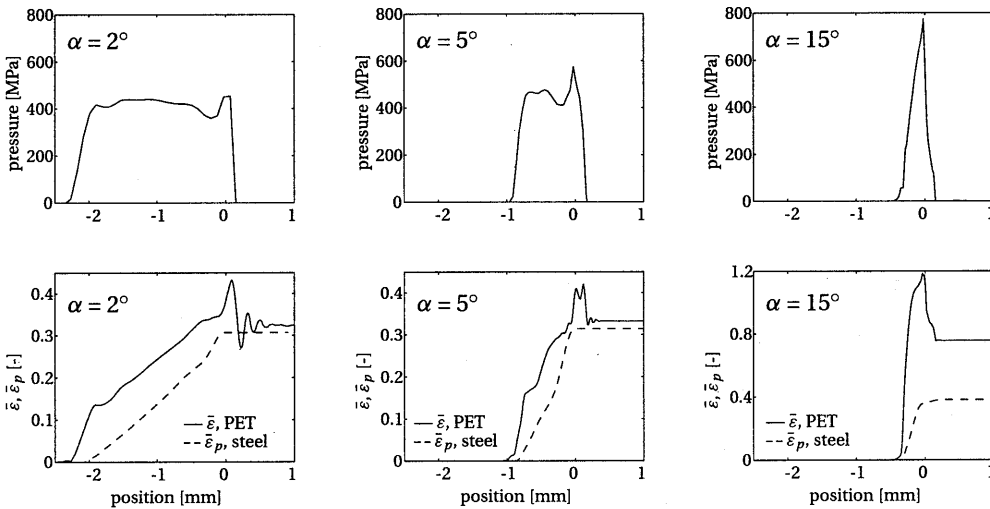


Figure 4.13. Influence of die angle on pressure, equivalent strain  $\bar{\epsilon}$  in PET and equivalent plastic strain  $\bar{\epsilon}_p$  in steel for a reduction of 25% and a velocity of 1 m/s.

A strong link exists between the pressure built up under the die and the resulting plastic deformations (or even failure) of the PET coating. As already observed in the

tensile tests under superimposed pressure in Subsection 2.4.1, PET is pressure sensitive, which results in an improved deformation resistance at higher pressures. Apparently, enough pressure must be built up in the coating to resist the imposed deformations. To explain this, it is necessary to consider the deformation of the coating.

To visualise the deformation occurring during strip ironing for the die angles of 2, 5 and 15°, a grid consisting of 5 × 5 points is positioned in the upper coating. Using the incremental displacements, these 25 particles are tracked through the deformation zone. In Figure 4.14, the deforming grids are shown. The indices (a)–(d) correspond to (a) the initial grid, (b) the grid halfway the deformation zone, (c) the grid just before leaving the die outlet, and (d) the grid after having left the die.

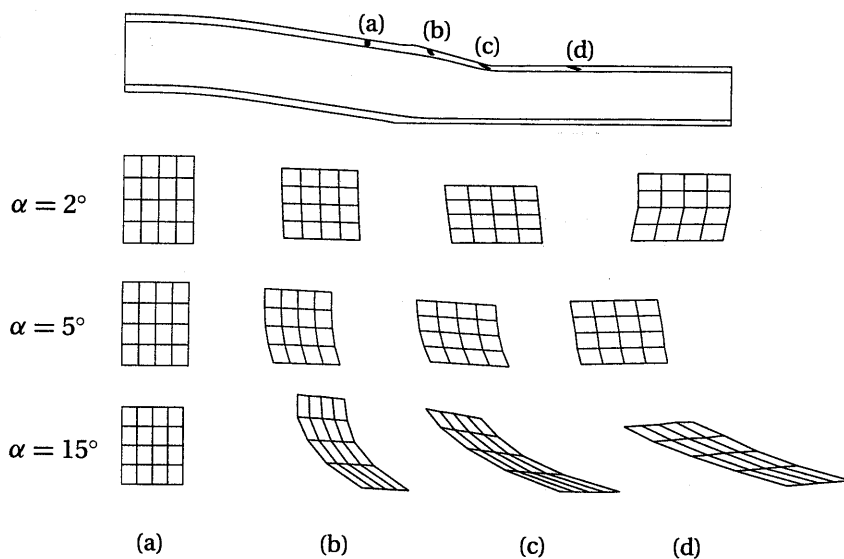


Figure 4.14. Particle tracking of a rectangular grid of a 5 × 5 points in the coating for die angles  $\alpha = 2, 5, 15^\circ$ . The indices (a)–(d) correspond to the positions in the upper picture.

The following aspects attract the attention:

- the deformation of the coating consists of two phases, which are dominated by a shear (b) and an elongation (c) deformation, respectively. These phases can be discerned in Figure 4.13 for the built up of pressure and the equivalent total strain at position -2, -0.8 and -0.2 for the three angles. It can be observed that, for  $\alpha = 2$  and  $5^\circ$ , a gradual accumulation of pressure effectively stops the strong increase in the equivalent strain, which is mainly caused by shear. The subsequent (elongation) deformation results in a slower increasing equivalent strain. For  $\alpha = 15^\circ$ , the built up of pressure can not prevent the extreme shear deformation.

- due to a die swell phenomenon, which occurs during transition (c)-(d), a ‘volumetric’ expansion of the grid is observed which partially recovers the shear deformation. This explains the relative large release of the equivalent total strains in Figure 4.13 after the die outlet for the three die angles.

In conclusion, it can be stated that a decrease in die angle will improve the performance of the coating, giving rise to a gradual pressure accumulation and smaller deformations.

### 4.3.2 Influence of ironing velocity

Since the set-up is mounted in a hydraulic tensile testing machine, it is possible to investigate the influence of ironing velocity up to industrial speeds of 10 m/s. Figure 4.15 shows the die force  $F_d$  as a function of the die angle  $\alpha$ , for velocities of 0.1, 1 and 10 m/s and a reduction of 25%. Simulations are performed for die angles of 2, 5 and 15° and show a quite good agreement with the experimental results. A velocity increase of two decades results in a considerable increase in  $F_d$  of 400 N/mm for a die angle of 2°. This increase is explained by the strain rate dependence of both PET and steel, causing a higher deformation resistance. Figure 4.16 shows that in the experiments it is not possible to determine an unambiguous influence of the ironing velocity on the punch force  $F_p$ . For bottom force  $F_b$ , numerical results predict a slight increase with increasing die angle and increasing velocity, as shown in Figure 4.17.

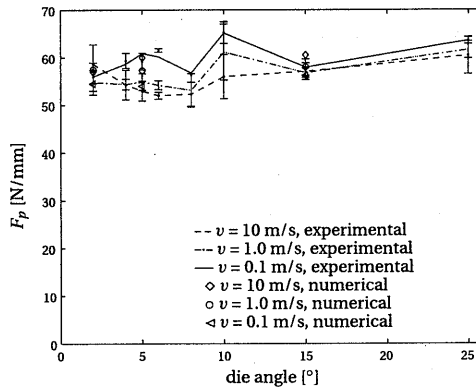
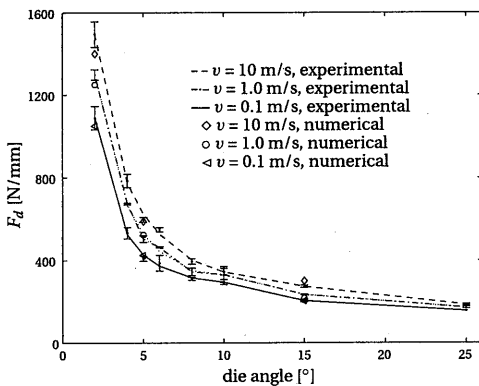


Figure 4.15. Influence of ironing velocity on die force  $F_d$ .

Figure 4.16. Influence of ironing velocity on punch force  $F_p$ .

The Coulomb friction coefficient  $\mu_p$  between punch and sheet is calculated from the experimentally obtained process forces using Eq. (4.17). Friction on the interface between punch and sheet decreases with decreasing die and increasing velocity, as shown in Figure 4.18. A minimum in  $\mu_p$  of 0.01 is found for a 2° die angle and a velocity of 10 m/s, which is similar to what would be expected if a quasi-hydrodynamic

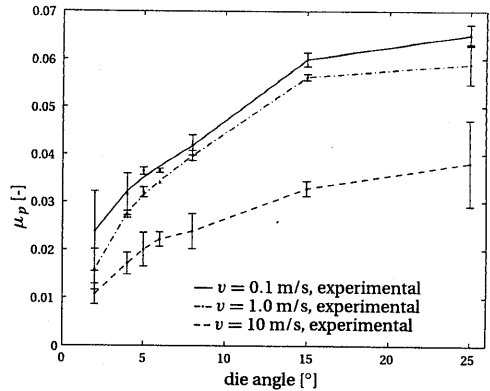
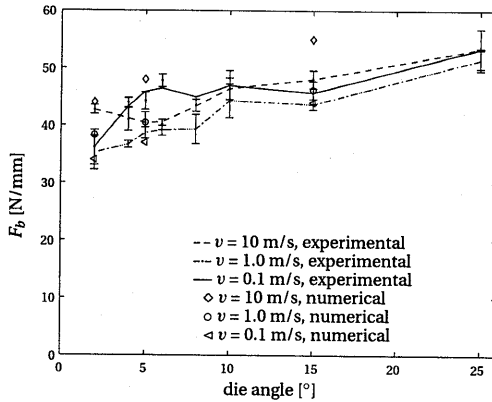


Figure 4.17. Influence of ironing velocity on bottom force  $F_b$ .

Figure 4.18. Influence of ironing velocity on friction coefficient  $\mu_p$ .

mechanism controlled entrainment of lubricant (Wilson and Cazeault, 1976). Apparently, for smaller angles, it is more likely that a fully developed film will give rise to lower friction. In general, it is observed during the experiments that a higher deformation velocity has a positive effect on the visual performance of the deformed coating, which has more gloss and less scratches.

### 4.3.3 Influence of ironing reduction

In this subsection, the influence of the reduction on process forces and friction is studied at a velocity of 10 m/s and for eight die angles. Figure 4.19 shows the die force  $F_d$  as a function of the die angle as determined in experiments and numerical simulations, for reductions of 10, 20 and 30%. In the numerical simulations, the die forces are determined only for two die angles (5 and 10°). Increasing the reduction results in a larger die force  $F_d$ , which implies an increased pressure in the deformation zone. The deformation resistance of PET will increase because of this enlarged pressure in a similar way as for small die angles. However, Figure 4.19 shows that  $F_d$  is increased far more by decreasing the die angle than by increasing reduction. Figure 4.20 illustrates the increase in punch force  $F_p$  with increasing reduction for an ironing velocity of 10 m/s. A minimum in  $F_p$  is found in the experiments for a die angle of 7 to 8°. The numerically obtained punch forces for die angles of 5 and 10° show a good correspondence with the measurements.

The increase in bottom force  $F_b$  with increasing reduction is shown in Figure 4.21. A minimum for  $F_b$  is found for a 5° die angle. Numerical simulations are performed for die angles of 5 and 10°, which match the experimental results quite well.

The influence of the die angle and reduction on the friction coefficient  $\mu_p$  is depicted in Figure 4.22. At small die angles (2 to 10°) and a large ironing velocity (10 m/s), a quite low friction coefficient  $\mu_p$  is found (below 0.03). At larger die angles,

friction increases for larger reductions. In the experiments, it was noticed that for die angle  $\alpha = 25^\circ$ , the coating is regularly scraped from the steel substrate, which gives rise to large deviations in measured friction coefficients. This explains the large error bars for this angle.

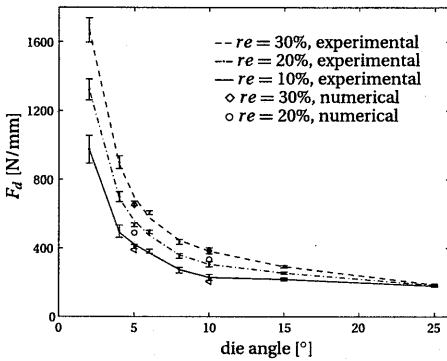


Figure 4.19. Influence of ironing reduction on die force  $F_d$ .

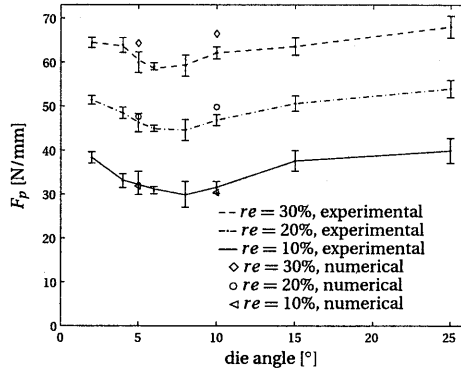


Figure 4.20. Influence of ironing reduction on punch force  $F_p$ .

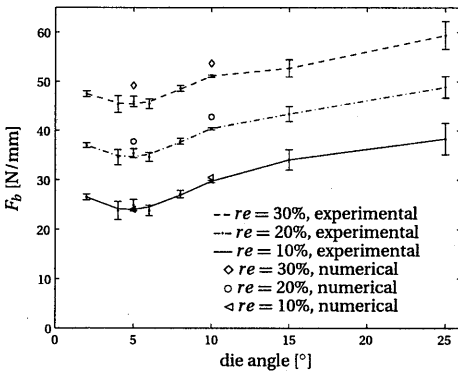


Figure 4.21. Influence of ironing reduction on bottom force  $F_b$ .

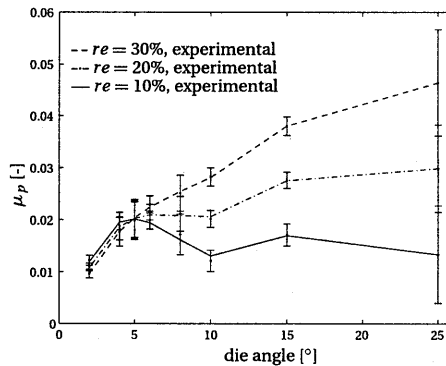


Figure 4.22. Influence of ironing reduction on friction coefficient  $\mu_p$ .

### 4.3.4 Sensitivity study of pressure and velocity dependence

To examine the influence of the pressure dependence and deformation velocity on the total equivalent strain in the coating, three simulations of the strip ironing process for PET coated steel sheet are compared:

- a strip ironing simulation at 1 m/s with pressure coefficient  $\mu = 0.047$
- a strip ironing simulation at 1 m/s with pressure coefficient  $\mu = 0$
- a strip ironing simulation at 1 mm/s with pressure coefficient  $\mu = 0.047$

For all simulations, the die angle  $\alpha = 5^\circ$  and the reduction of 25% are kept constant. In Figure 4.23, the total equivalent strain in the upper coating for the three situations is shown as a function of the position in the deformation zone relative to the die outlet. The total equivalent strains after the die outlet are: 0.32, 0.57 (+78%) and 0.37 (+16%), respectively. Therefore, pressure dependence and strain rate dependence of a polymer significantly contribute to the deformation resistance of the coating.

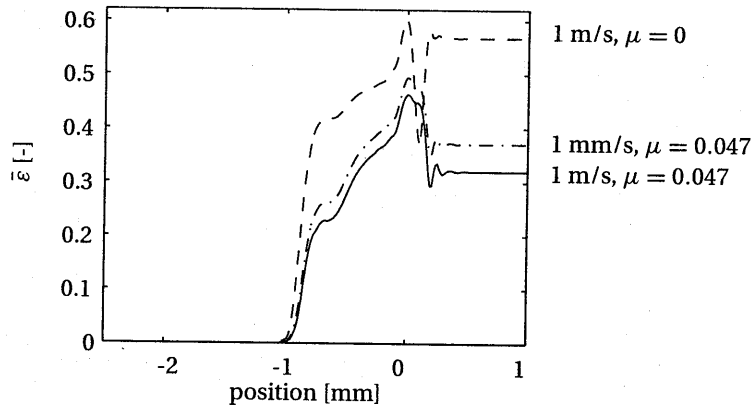


Figure 4.23. Influence of pressure dependence and deformation rate on equivalent strain  $\bar{\epsilon}$ .

#### 4.3.5 Analysis of flow paths and strain fields

The influence of the die angle on the tool forces for PET coated annealed aluminium is determined for a punch velocity of 8 m/s and a reduction of 25%. Figure 4.24 shows the three measured process forces for the entire range of die angles. Numerical simulations are performed for die angles of 5, 10, 15 and 25°. The punch forces  $F_p$  and  $F_b$  do hardly change over the range of die angles while a large die angle dependence is observed for  $F_d$ . As observed for the coated steel, die force  $F_d$  increases considerably for small angles. A good correspondence is found for the measured and computed global forces. In the experiments, in contrast to the coated steel experiments for large angles, no failure of the PET coating is observed for the entire range of die angles.

The digital image correlation technique of Subsection 4.2.3 is used to determine displacement fields from recorded video images. In order to visualise the deformation, a relatively thick strip is used, since the magnification of the zoom lens is restricted. All digital images of the specimen surface are recorded at a punch velocity of 0.1 mm/s

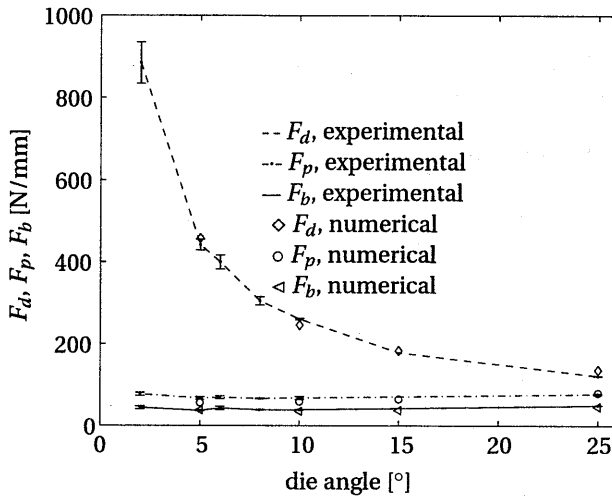


Figure 4.24. Influence of die angle on process forces.

for a die angle of  $15^\circ$ , using an 1 mm aluminium strip coated on one side with a 0.5 mm layer of PET. An annealed aluminium AA 1050 substrate is chosen instead of steel to prevent the polymer from being squeezed out of the deformation zone in the direction of the camera. Figure 4.25 shows the flow paths of 23 points, that originally form a vertical line, in the deformation zone between punch and die. Figure 4.26 shows that a shear deformation homogeneously spreads over both aluminium and polymer during the deformation.

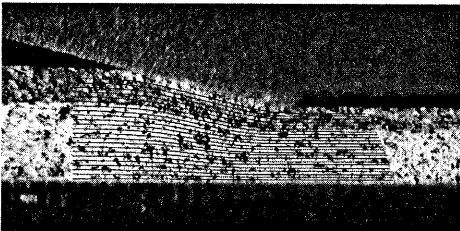


Figure 4.25. Experimentally obtained flow paths of material points in the PET coated aluminium sheet.

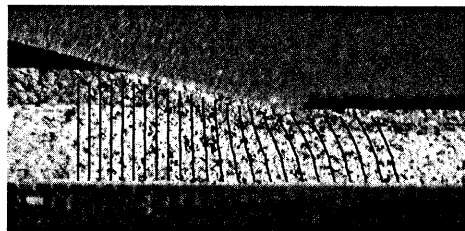


Figure 4.26. Visualisation of shear in the deformation zone. PET and aluminium show an equal amount of shear.

In order to calculate the total equivalent strains in the experiments, a rectangular grid of 121 material points is defined in the undeformed section of the strip. The equivalent strains are calculated in both experiments and simulations using the second order technique described in Subsection 4.2.3. Figure 4.27 shows the experimen-

tally and numerically obtained strain fields in a steady state flow for three reductions (10, 20 and 30%) at an ironing velocity of 0.1 mm/s.

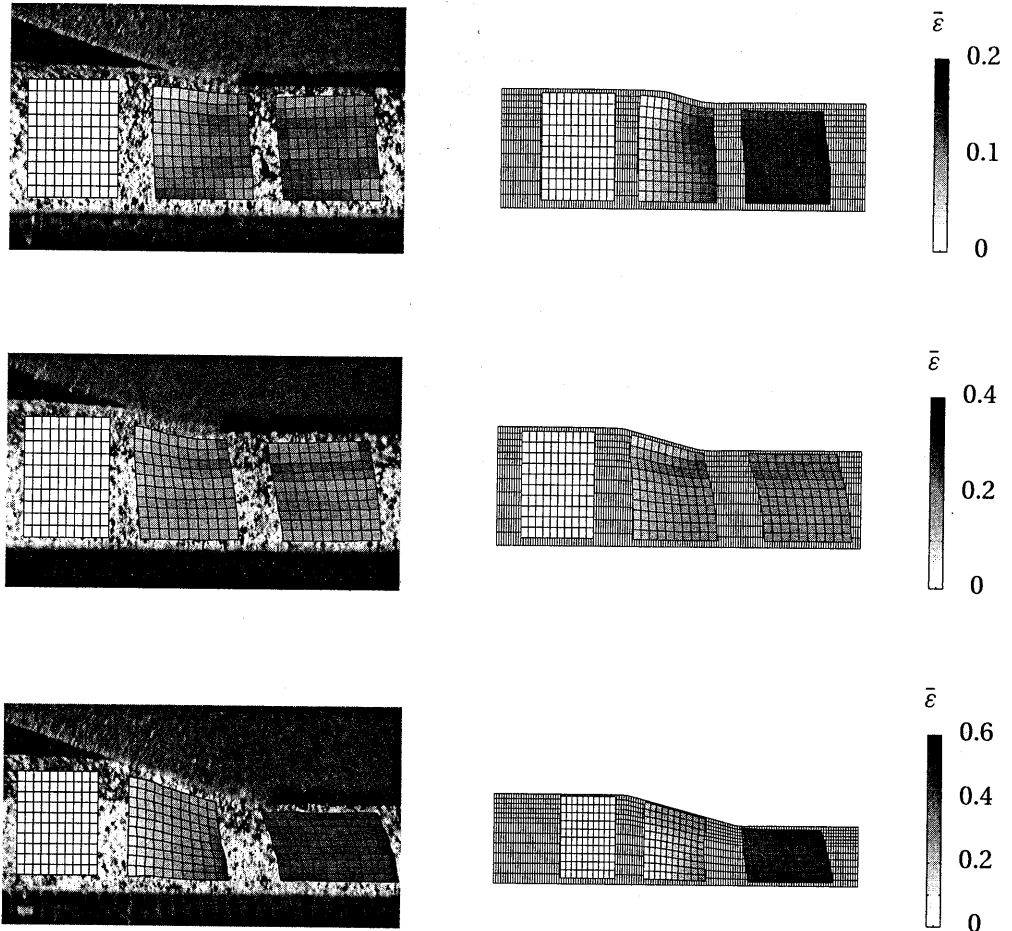


Figure 4.27. Total equivalent strain fields with reductions of 10, 20 and 30%, for polymer coated aluminium.

Obviously, larger reductions give rise to higher equivalent total strains. A reasonable correspondence is found between experimental and numerical results. For all reductions, the numerically calculated strains show a small overestimation of the total equivalent strains. This deviation might be caused by the fact that a plane stress situation in the experiment is compared with a plane strain computation.



## 4.4 Full-scale experiment

Experiments on industrial scale have been performed at Hoogovens Research & Development (van Rijn, 1998). The force that can be measured is the toolpack force, which is the force working on the frame in which the ironing rings are fixed. During the wall ironing process, the cup is deformed separately by each ring, because otherwise failure of the can occurs. Thus, the force exerted on each ring can be measured separately. In Figure 4.28, the position, where force  $F_t$  is measured, is schematically depicted. A measurement of the toolpack force is shown in Figure 4.30. In the experiments, PET coated steel is used and three ironing rings. The strong increase of the toolpack force in the first ring is caused by an increasing wall thickness in the cup due to the deep drawing step preceding the wall ironing operation. For the second and third ring, a more constant force level is observed.

In the simulation, only the first ring of  $8^\circ$  with a reduction of 28% and a 0.5 mm land zone is considered. The velocity of the punch at this position is estimated on 2.5 m/s. available. Therefore, based on the experiments with the strip ironing device, the friction coefficients between punch and coated sheet metal  $\mu_p = 0.017$  and between die ring and coated sheet metal  $\mu_d = 0.010$  are chosen. The computed toolpack force of 12.3 kN is shown in Figure 4.30. by prescribing the (increasing) wall thickness during the ironing simulation.

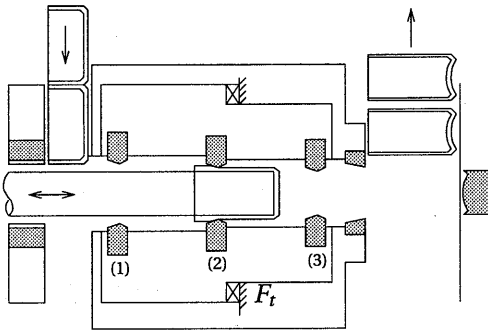


Figure 4.28. Measurement of force  $F_t$  working on the toolpack.

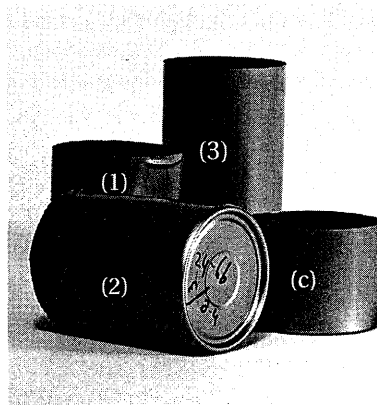


Figure 4.29. Different stages of the can: (c) after cupping, (1)–(3) after ring 1, 2 and 3.

The results of an isothermal simulation are compared with a thermo-mechanical coupled simulation. However, it is quite difficult to determine the proper thermal boundary conditions for the coupled analysis. The set of history dependent variables is extended with temperature  $T$ . The following assumptions are made:

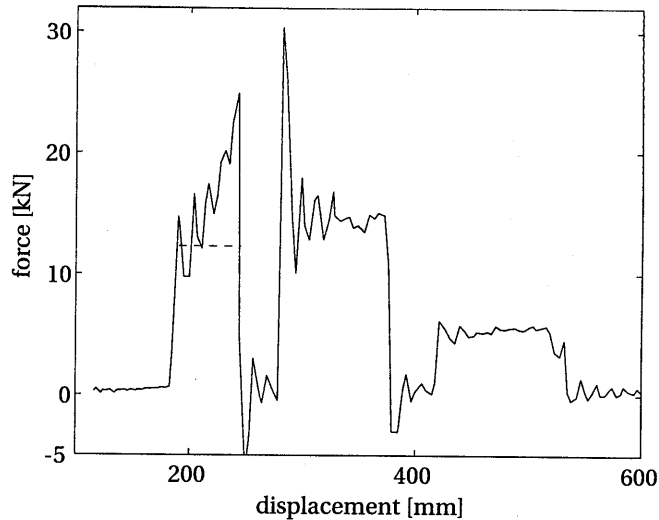


Figure 4.30. Measured toolpack force for three ironing rings and the computed toolpack force (dashed) for only the first ring.

- Good cooling conditions by the emulsion are assumed using a heat convection coefficient  $\alpha = 2000 \text{ W/m}^2\text{K}$  (Balmer, 1990).
- The influence of elevated temperatures on the yield stress of PET is taken into account based on tensile tests performed at 40 and 60 °C.
- For the mechanical behaviour of the sheet metal, no influence of temperature on the resistance to plastic flow  $Z$  is assumed.

In a coupled elasto-viscoplastic analysis, two finite element formulations, coupled through viscoplastic work, are decoupled at each time step and solved in a staggered procedure. The following solution scheme is applied:

1. The heat conduction equation is solved during a small time step by introduction of the updated geometry and heat generation to the solution of the finite element heat conduction equation.
2. The temperature is updated.
3. The mechanical problem is solved during the same time interval, while the updated temperature is held constant. Also, heat generation by viscoplastic work is calculated and saved.
4. The geometry is updated.

Table 4.2 gives additional material parameters for PET and steel: mass density  $\rho$ , thermal conductivity  $k$ , thermal expansion  $\alpha$  and specific heat  $c$ . The material properties are given by the suppliers Eastman and Hoogovens, respectively.

	<i>properties</i>			
	$\rho$ [kg m <sup>-3</sup> ]	$k$ [W m <sup>-1</sup> K <sup>-1</sup> ]	$\alpha$ [K <sup>-1</sup> ]	$c$ [J kg <sup>-1</sup> K <sup>-1</sup> ]
PET	1330	0.28	80 10 <sup>-6</sup>	2150
steel	7800	50	1.2 10 <sup>-5</sup>	480

Table 4.2. Material properties of PET and steel (ECCS) at room temperature (293 [K]).

For the coupled thermo-mechanical simulation, the temperatures of the steel and the inside and outside coating are shown in Figure 4.31. The steady state temperatures of the steel is 135 °C. The temperature of the outside coating (75 °C) becomes significantly higher than the temperature of the inside coating (42 °C), because of the larger deformation occurring in the outside coating, which gives rise to more heat generation due to plastic work. Note that the temperature in the outside coating is higher than the glass transition temperature under atmospheric conditions ( $T_g \approx 70$  °C). Therefore, it is interesting to compare the computed equivalent total strain in the coating with an isothermal computation. In Figure 4.32, the equivalent total strain for the coupled thermo-mechanical and the isothermal simulation are depicted versus the position relative to the die. It is seen that a relatively small increase in equivalent strain of less than 5% is caused by taking into account temperature effects.

The limited influence of thermal effects on the mechanical behaviour of the PET layer is due to an opposing effect of high hydrostatic pressure. To illustrate the effect, Zoller and Bolli (1980) have examined the influence of pressure on the glass transition temperature  $T_g$ . For amorphous PET,  $T_g$  is increasing with pressure according to  $dT_g/dp = 0.36$  °C/MPa over a measured pressure range 0–200 MPa. According to this ratio,  $T_g$  hypothetically rises to 250 °C for a pressure of 500 MPa.

## 4.5 Conclusions

In this chapter, the simulation model for the wall ironing process of polymer coated sheet metal has been validated under realistic processing conditions using (model) experiments on a strip ironing device and an experiment on an industrial production machine. Friction coefficients obtained in a plane strain strip ironing device were directly used in the numerical simulation, thus no assumptions with relation to friction were required. Simulations were performed with an Arbitrary Lagrange Euler method based on an Operator Splitting procedure (OS-ALE) using advanced constitutive models. Experiments and numerical simulation have proved to be complemen-

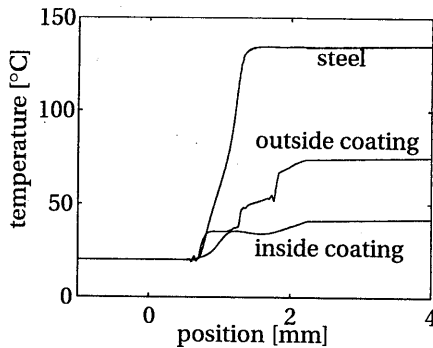


Figure 4.31. Temperature development in the steel and the inside and outside coating.

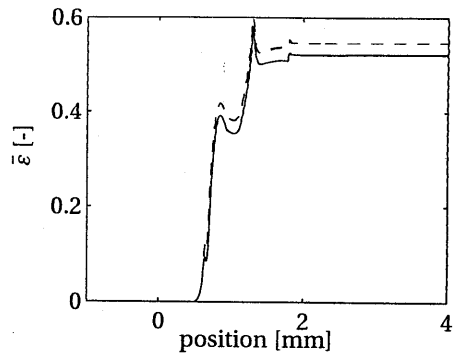


Figure 4.32. Comparison of the equivalent total strain for an isothermal (solid) and a coupled (dashed) computation.

tary. From the investigation using the strip ironing set-up, the following conclusions can be drawn:

- In the strip ironing of polymer coated steel, small die angles enforce a gradual accumulation of pressure, which suppresses the shear deformation, and subsequently a moderate development of the equivalent total strain. For the polymer coating, this increase in pressure is the key parameter to survive the process.
- Increasing ironing velocity gave rise to larger pressures in the deformation zone because of the strain rate dependence of both steel and PET. Therefore, it is necessary to incorporate elasto-viscoplastic material behaviour in the constitutive models.
- In the ironing experiments, it was observed that a minimum in punch force and punch bottom force is found for die angles of 7 and 5 degrees, respectively. Both punch force and punch bottom force increase for increasing reduction and are nearly independent of the ironing velocity.
- Small punch friction coefficients in between 0.01 and 0.03 are measured for PET coated steel for die angles between 2 and 10°, at an ironing velocity of 10 m/s. Increasing the velocity significantly reduced the punch friction coefficient.
- Using a digital image correlation technique, strain fields were obtained and compared to simulations, showing a reasonable agreement. The polymer coated aluminium deformed as an homogeneous material, with equal shear and plastic strain in polymer and metal.

From the experiment on the bodymaker, we can conclude that it is quite difficult to obtain the appropriate mechanical and thermal boundary conditions. However, the

strip ironing device can be used to measure friction coefficients for the full-scale process, provided that the tribological conditions in the device are made similar to those in a bodymaker using the same lubricant and emulsion.

Thermal conditions might strongly influence the mechanical behaviour of the polymer coating. However, hydrostatic pressure opposes the loss of mechanical properties due to thermal effects.



# Chapter 5

## Conclusions and recommendations

In order to obtain a cheaper and environmentally cleaner can production process, can manufacturers must be able to deform polymer coated sheet metal properly, without delamination or failure of the coating. Modelling of the process is one of the possibilities to gain fundamental insight in the process and subsequently improve it without costly tooling and lead times.

In this thesis, a simulation model has been presented to describe the wall ironing process of polymer coated sheet metal. The complex constitutive material behaviour of sheet metal and coating are described using the generalised compressible Leonov model. The model is based on an Arbitrary Lagrange Euler method to prevent mesh distortion and to track the free surfaces. Model validation has been performed for a range of die angles, deformation velocities and reductions. Measurement of the tool-pack force in a full-scale experiment has been compared with results from a coupled thermo-mechanical simulation.

### 5.1 Conclusions

A numerical-experimental strategy has been developed to accurately verify the finite element model OS-ALE. An experimental device has been realised by which realistic experiments can be performed regarding the deformation process, the occurring hydrostatic pressures and the deformation speeds. Moreover, this device can be used to examine friction behaviour of deforming materials under realistic processing conditions. Digital image correlation has proved to be a beneficial tool to obtain displacement fields. The conclusions related to the thesis are:

- The advanced constitutive equations have appeared to be of eminent importance in the understanding of metal and polymer behaviour undergoing large deformations at high strain rates and high pressures.
- Operator Splitted ALE is very well suited to handle large deformations combined with free surface flows.

- The Discontinuous Galerkin method is a successful transport method for the simulation of forming processes with OS-ALE: discontinuous fields of state variables are incrementally transported with a minimum of diffusion.
- The pressure accumulation in the polymer coating is a key parameter for the wall ironing process of polymer coated sheet metal.
- Another important parameter is the strain rate dependence of the polymer, which also improves the deformation resistance of the coating.
- Using aluminium with a PET coating in the strip ironing experiment, measurement of the displacement field shows a similar deformation pattern in both aluminium and PET.
- Temperature rises due to plastic deformation and friction have a minor influence on the mechanical behaviour of the polymer coating.

## 5.2 Recommendations

In this thesis, the attention was focussed on the wall ironing process of virgin coated plate for a single die. Of course, the model has to be extended with a deep drawing and a redraw step preceding this die, and two ironing steps, which follow the first one. With respect to the ironing operations, the presented model can be re-used after the first ironing step by putting the deformed material once again in the ironing model. In fact, instead of starting the forming process with a virgin material, the values of the history dependent variables are used for the second ironing steps.

Up to now, only visualisation experiments have been performed for a 1 mm thick aluminium sheet with a 0.5 mm PET coating at a low deformation velocity. It is interesting to scale this experiment down to thin coated sheet using a microscope. The experiments with PET coated sheet metal failed as the PET is squeezed out of the deformation zone, which gives rise to focussing problems. A transparent plate could be used to suppress this deformation. Then, the die swell phenomenon of the polymer at the outlet of the die can be investigated. Also experiments at higher deformation rates can be performed to examine the increasing deformation resistance of PET at higher velocities. Known problems at higher velocities are vibrations of the frame, which hamper the recording of sharp images.

Another topic that deserves attention is the determination of failure criteria for the coating using the presented numerical-experimental technique. Characteristic for the failure of the PET coating during wall ironing is a phenomenon called 'micro-voiding', in which small voids cause a whitening of the PET film. In Figure 5.1, this effect is illustrated by performing an uniaxial tension test under atmospheric conditions, and under 600 MPa hydrostatic pressure (see Subsection 2.4.1).



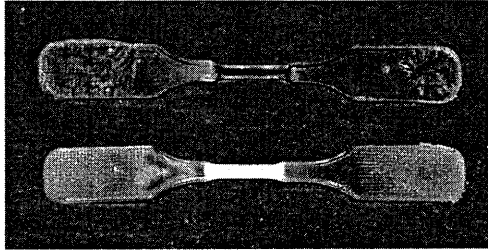


Figure 5.1. Specimens after a tension test under atmospheric conditions (lower figure) and superimposed pressure of 600 MPa (upper figure).

Hydrostatic pressure is an effective method to suppress this phenomenon. Wide Angle X-ray Scattering (WAXS) measurements of both specimens have shown (Schrauwen *et al.*, 1998), that for both specimens the material is amorphous and no crystallisation effects are observed. Using in-situ Small Angle X-ray Scattering (SAXS), characteristic craze formation patterns are observed. Conclusion of their experiments was that stress whitening is caused solely by cavitation. This indicates that a high hydrostatic pressure (or small die angles) also favours the aesthetic performance of polymeric coatings for the wall ironing process of pre-coated cans, but further investigation in this direction is necessary.

A topic closely related to failure mechanisms of coating material is the development of design methodology for coatings. Jayachandran *et al.* (1995) present an approach to design multilayered coatings to provide the desired mechanical behaviour during indentation. Using a parameter variation study using the finite element method, a suitable coating is tailor-made by a careful selection and placement of different material layers required during service. Jayachandran *et al.* have obtained good results using a bilayer polymer coating system, with a soft coating on the metal substrate and a hard coating on top of it. Then, a low interfacial shear stress is maintained during indentation, and the level of surface tensile stress is minimised. Some of their ideas can be used in the coating design of the current application.

The influence of the strain induced crystallisation for semi-crystalline polymers has to be investigated. In Chapter 2, it is stated that no distinction is made between hardening due to molecular orientation and strain induced crystallisation. Using the differential scanning calorimetry method, Zaroulis and Boyce (1997) examined the crystallinity content as a function of the mechanical loading (effects of temperature, strain rate, and strain state on the finite deformation). Main conclusion is that above glass transition temperature  $T_g$ , the mechanical behaviour is characterised by a strong sensitivity of the strain hardening behaviour to strain rate. High strain rates favour orientation and possible strain-induced crystallisation results in pronounced strain hardening. In the wall ironing process of coated material, it is questionable whether strain-induced crystallisation occurs during or after the actual forming process. More-

over, the influence of the high hydrostatic pressure on this effect has to be investigated.

The developed tools can be applied to design an optimised die geometry. Important design variables are:

- the equivalent plastic strain in the coating which is important with respect to failure of the coating (see Section 4.3.1).
- the bottom force  $F_b$  which is important with respect to failure of the total can. It was found in Section 4.3.3 that the bottom force  $F_b$  shows an optimum for a die angle  $\alpha = 5^\circ$ .
- the die force  $F_d$  with respect to failure of the die. For the axisymmetric case of wall ironing, this force is strongly related to the hoop stress present in the ring. To avoid failure of the ring, this stress is a design variable, which should not exceed a critical limit.

Apart from die optimisation, also further research is necessary to investigate other coating materials than PET.

# Appendix A

## Details on the stiffness matrices of the material models

Objective of this appendix is to determine the variation of elasticity scalar  $\delta\lambda$  caused by the variations  $\delta\tilde{\mathbf{B}}_e$  and  $\delta\tilde{\mathbf{F}}$  for both elasto-viscoplastic models. Starting point is the relation (3.22):

$$\delta\lambda = \frac{\lambda\Delta t\Gamma}{G\Delta t + \eta} \delta\eta \quad (\text{A.1})$$

### A.1 Compressible Leonov model

Viscosity function (2.12) depends on the equivalent Von Mises stress  $\bar{\sigma} = G\sqrt{\frac{3}{2}\tilde{\mathbf{B}}_e^d : \tilde{\mathbf{B}}_e^d}$ , pressure  $p$ , and softening variable  $D$ . The viscosity can be written as:

$$\eta = \frac{2A_0\bar{\sigma}}{\sqrt{3}} \exp\left[\frac{\Delta H}{RT} + \frac{\mu p}{\tau_0} - D - \frac{\bar{\sigma}}{\sqrt{3}\tau_0}\right] \quad (\text{A.2})$$

where we used the approximation  $\sinh(x) = \frac{1}{2}(\exp(x) - \exp(-x)) \approx \frac{1}{2}\exp(x)$  as proposed in Subsection 2.4.1.

The variation  $\delta\eta$  can be written as:

$$\delta\eta = \frac{\partial\eta}{\partial\bar{\sigma}}\delta\bar{\sigma} + \frac{\partial\eta}{\partial p}\delta p + \frac{\partial\eta}{\partial D}\frac{\partial D}{\partial\bar{\sigma}}\delta\bar{\sigma} + \frac{\partial\eta}{\partial D}\frac{\partial D}{\partial p}\delta p \quad (\text{A.3})$$

and for  $\delta\bar{\sigma}$  and  $\delta p$ , one obtains:

$$\delta\bar{\sigma} = \frac{3G^2}{2\bar{\sigma}}\tilde{\mathbf{B}}_e^d : \delta\tilde{\mathbf{B}}_e^d = \frac{3G^2}{2\bar{\sigma}}\tilde{\mathbf{B}}_e^d : \delta\tilde{\mathbf{B}}_e \quad ; \quad \delta p = -\kappa \text{Jtr}(\delta\tilde{\mathbf{F}}) \quad (\text{A.4})$$

For the partial derivatives of the discretised evolution equation  $D_{n+1} = D_n + \Delta t\dot{D}$  (2.45), we can write:

$$\frac{\partial D}{\partial\bar{\sigma}} = \Delta t \left( \frac{\partial\dot{D}}{\partial\bar{\sigma}} + \frac{\partial\dot{D}}{\partial D}\frac{\partial D}{\partial\bar{\sigma}} \right) \quad ; \quad \frac{\partial D}{\partial p} = \Delta t \left( \frac{\partial\dot{D}}{\partial p} + \frac{\partial\dot{D}}{\partial D}\frac{\partial D}{\partial p} \right)$$

and, thus:

$$\frac{\partial D}{\partial \bar{\sigma}} = \frac{\Delta t \frac{\partial \dot{D}}{\partial \bar{\sigma}}}{1 - \Delta t \frac{\partial \dot{D}}{\partial D}} \quad ; \quad \frac{\partial D}{\partial p} = \frac{\Delta t \frac{\partial \dot{D}}{\partial p}}{1 - \Delta t \frac{\partial \dot{D}}{\partial D}} \quad (\text{A.5})$$

The partial derivatives in Eq. (A.3) yield:

$$\frac{\partial \eta}{\partial \bar{\sigma}} = \eta \left( \frac{1}{\bar{\sigma}} - \frac{1}{\sqrt{3}\tau_0} \right) \quad ; \quad \frac{\partial \eta}{\partial p} = \frac{\eta \mu}{\tau_0} \quad ; \quad \frac{\partial \eta}{\partial D} = -\eta \quad (\text{A.6})$$

$$\frac{\partial \dot{D}}{\partial \bar{\sigma}} = \frac{\dot{D}}{\sqrt{3}\tau_0} \quad ; \quad \frac{\partial \dot{D}}{\partial p} = \frac{\dot{D} \mu}{\tau_0} \quad ; \quad \frac{\partial \dot{D}}{\partial D} = \dot{D} - \frac{h\bar{\sigma}}{\sqrt{6}D_\infty \eta} \quad (\text{A.7})$$

Substitution of  $\delta \bar{\sigma}$  and  $\delta p$  into Eq. (A.3) gives:

$$\delta \eta = h_1 \tilde{\mathbf{B}}_e^d : \delta \tilde{\mathbf{B}}_e + h_2 \mathbf{I} : \delta \mathbf{F} \quad (\text{A.8})$$

with scalars  $h_1 = \frac{3G^2}{2\bar{\sigma}} \left( \frac{\partial \eta}{\partial \bar{\sigma}} + \frac{\partial \eta}{\partial D} \frac{\partial D}{\partial \bar{\sigma}} \right)$  and  $h_2 = -\kappa J \left( \frac{\partial \eta}{\partial p} + \frac{\partial \eta}{\partial D} \frac{\partial D}{\partial p} \right)$ . Insertion of this relation in Eq. (3.22) yields:

$$\delta \lambda = l_1 \tilde{\mathbf{B}}_e^d : \delta \tilde{\mathbf{B}}_e + l_2 \mathbf{I} : \delta \mathbf{F} \quad (\text{A.9})$$

with scalars  $l_1 = \frac{\lambda \Delta t \Gamma h_1}{\Delta t \Gamma + \eta}$  and  $l_2 = \frac{l_1 h_2}{h_1}$ .

## A.2 Bodner-Partom model

Viscosity function (2.19) depends on the equivalent stress  $\bar{\sigma} = G \sqrt{\frac{3}{2} \tilde{\mathbf{B}}_e^d : \tilde{\mathbf{B}}_e^d}$  and the equivalent plastic strain  $\bar{\varepsilon}_p$ . The variation of  $\delta \eta$  consists of the contributions:

$$\delta \eta = \frac{\partial \eta}{\partial \bar{\sigma}} \delta \bar{\sigma} + \frac{\partial \eta}{\partial \bar{\varepsilon}_p} \frac{\partial \bar{\varepsilon}_p}{\partial \bar{\sigma}} \delta \bar{\sigma} \quad (\text{A.10})$$

For the partial derivatives with respect to the equivalent Von Mises of the discretised evolution equation  $\bar{\varepsilon}_{p,n+1} = \varepsilon_{p,n} + \Delta t \dot{\bar{\varepsilon}}_p$ , we can write in analogy with Eq. (A.5):

$$\frac{\partial \bar{\varepsilon}_p}{\partial \bar{\sigma}} = \frac{\Delta t \frac{\partial \dot{\bar{\varepsilon}}_p}{\partial \bar{\sigma}}}{1 - \Delta t \frac{\partial \dot{\bar{\varepsilon}}_p}{\partial \bar{\varepsilon}_p}} \quad (\text{A.11})$$

The partial derivatives now read:

$$\frac{\partial \eta}{\partial \bar{\sigma}} = \frac{\eta}{\bar{\sigma}} - n \eta \bar{\sigma}^{-2n-1} Z^{2n} \quad ; \quad \frac{\partial \eta}{\partial \bar{\varepsilon}_p} = -m n \eta \bar{\sigma}^{-2n} Z^{2n} (Z_0 - Z_1) \exp(-m \bar{\varepsilon}_p - 1) \quad (\text{A.12})$$

$$\frac{\partial \dot{\bar{\epsilon}}_p}{\partial \bar{\sigma}} = \dot{\bar{\epsilon}}_p \left( \frac{1}{\bar{\sigma}} - \frac{\partial \eta}{\partial \bar{\sigma}} \right) \quad ; \quad \frac{\partial \dot{\bar{\epsilon}}_p}{\partial \bar{\epsilon}_p} = - \frac{\dot{\bar{\epsilon}}_p \frac{\partial \eta}{\partial \bar{\epsilon}_p}}{\eta} \quad (\text{A.13})$$

Substitution of  $\delta \bar{\sigma}$  into Eq. (A.10) and insertion of the result in Eq. (A.1) yields:

$$\delta \lambda = b_1 \tilde{\mathbf{B}}_e^d : \delta \tilde{\mathbf{B}}_e \quad ; \quad b_1 = \frac{\lambda \Delta t \Gamma}{\Delta t G + \eta} \frac{3G^2}{2\bar{\sigma}} \left( \frac{\partial \eta}{\partial \bar{\sigma}} + \frac{\partial \eta}{\partial \bar{\epsilon}_p} \frac{\partial \bar{\epsilon}_p}{\partial \bar{\sigma}} \right) \quad (\text{A.14})$$



# Appendix B

## Derivation and implementation of the Discontinuous Galerkin Method

In this appendix, the Discontinuous Galerkin method is described in more detail. In Section B.1, the Discontinuous Galerkin method is derived for the one-dimensional case. The implementation for the two-dimensional case is discussed in Section B.2.

### B.1 One-dimensional derivation of the DG method

For the one-dimensional case, transport equation (3.39) reads:

$$\varphi^b - \varphi^a - u_m \cdot \frac{\partial \varphi^b}{\partial x} = 0 \quad (\text{B.1})$$

Let  $\Omega$  be the domain of interest, which is subdivided into  $N$  elements  $\Omega^e : x \in [x_{n-1}, x_n]$ . Along the boundary  $\Gamma$  of the domain, we assume no inflow of material:  $u(x = x_0) = u(x = x_N) = 0$  on  $\Gamma$ . Here,  $u_m(x)$  is the *mesh* displacement and the material does not move in space to maintain equivalence with the Lagrange formulation. The weak form of the transport equation (B.1) is given by:

$$\int_{x=x_0}^{x_N} \left( \varphi^b(x) - \varphi^a(x) - u_m(x) \frac{\partial \varphi^b(x)}{\partial x} \right) w(x) dx = 0 \quad \forall w(x) \quad (\text{B.2})$$

Using the finite element method, domain  $\Omega$  is subdivided into  $N$  elements, which results in:

$$\sum_{n=1}^N \int_{x=x_{n-1}}^{x_n} \left( \varphi^b(x) - \varphi^a(x) - u_m(x) \frac{\partial \varphi^b(x)}{\partial x} \right) w(x) dx = 0 \quad \forall w(x) \quad (\text{B.3})$$

The functions  $\varphi^a(x)$ ,  $\varphi^b(x)$ , and  $w(x)$  are allowed to be discontinuous at all mesh points. In the neighbourhood of these points a small interval is defined. The interval for point  $x = x_{n-1}$  is  $[x_{n-1} - \Delta x, x_{n-1} + \Delta x]$  and is shown in Figure B.1. Now, Eq.

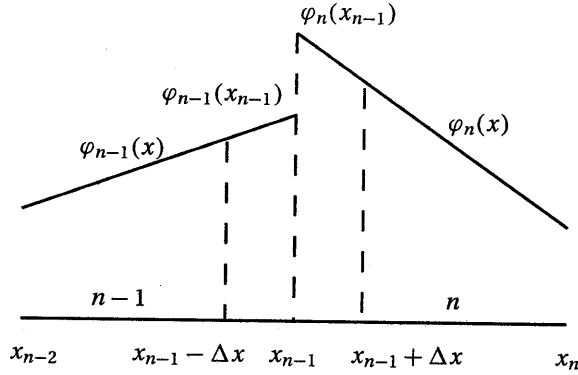


Figure B.1. Neighbourhood of interval  $[x_{n-1} - \Delta x, x_{n-1} + \Delta x]$ .

(B.3) can be split up in four parts:

$$\begin{aligned} & \sum_{n=1}^N \int_{x=x_{n-1}+\Delta x}^{x_n-\Delta x} \left( \varphi^b(x) - \varphi^a(x) - u_m(x) \frac{\partial \varphi^b(x)}{\partial x} \right) w(x) dx + \\ & \sum_{n=2}^N \int_{x=x_{n-1}-\Delta x}^{x_{n-1}+\Delta x} \left( \varphi^b(x) - \varphi^a(x) - u_m(x) \frac{\partial \varphi^b(x)}{\partial x} \right) w(x) dx + \\ & \int_{x=x_0}^{x_0+\Delta x} \left( \varphi^b(x) - \varphi^a(x) - u_m(x) \frac{\partial \varphi^b(x)}{\partial x} \right) w(x) dx + \\ & \int_{x=x_N-\Delta x}^{x_N} \left( \varphi^b(x) - \varphi^a(x) - u_m(x) \frac{\partial \varphi^b(x)}{\partial x} \right) w(x) dx = 0 \quad \forall w(x) \quad (\text{B.4}) \end{aligned}$$

The second term of this equation describes the transport of the material variable through the discontinuities due to mesh displacement  $u_m$ .

On the interval around  $x_{n-1}$ , according to Figure B.1,  $\varphi(x)$  is defined by:

$$\varphi(x) = \varphi_{n-1}(x) + \epsilon(x - x_{n-1})(\varphi_n(x) - \varphi_{n-1}(x)) \quad (\text{B.5})$$

where  $\epsilon(\xi)$  is the unity step function:

$$\epsilon(\xi) = \begin{cases} 1 & \text{for } \xi > 0 \\ 0 & \text{for } \xi \leq 0 \end{cases} \quad (\text{B.6})$$



The derivative of the unity step function  $\frac{d\epsilon(\xi)}{d\xi}$  is the Dirac pulse  $\delta(\xi)$ , which has the properties:

$$\delta(\xi) = 0 \quad \text{for} \quad \xi \neq 0 \quad \text{and} \quad (B.7)$$

$$\int_{-\infty}^{\infty} f(\xi) \delta(\xi - a) d\xi = f(a) \quad (B.8)$$

On interval  $[x_{n-1} - \Delta x, x_{n-1} + \Delta x]$ , we get:

$$\begin{aligned} \frac{d\varphi(x)}{dx} &= \frac{d\varphi_{n-1}(x)}{dx} + \delta(x - x_{n-1})(\varphi_n(x) - \varphi_{n-1}(x)) + \\ &\quad \epsilon(x - x_{n-1}) \left( \frac{d\varphi_n(x)}{dx} - \frac{d\varphi_{n-1}(x)}{dx} \right) \end{aligned} \quad (B.9)$$

After substitution of Eqs. (B.5) and (B.9) into Eq. (B.4), and letting  $\Delta x \rightarrow 0$ , only terms multiplied with the Dirac pulse  $\delta$  result, due to its filtering characteristic given in Eq. (B.8). The resulting equation is given by:

$$\begin{aligned} \sum_{n=1}^N \int_{x=x_{n-1}}^{x_n} \left( \varphi^b(x) - \varphi^a(x) - u_m(x) \frac{\partial \varphi^b(x)}{\partial x} \right) w(x) dx - \\ \sum_{n=2}^N \{ w(x_{n-1}) u_m(x_{n-1}) (\varphi_n^b(x_{n-1}) - \varphi_{n-1}^b(x_{n-1})) \} = 0 \end{aligned} \quad (B.10)$$

Now, a choice has to be made how to evaluate  $w(x_{n-1})$ , which is undefined since  $w(x)$  is discontinuous at  $x = x_{n-1}$ . A possible choice is a weighted average over the lower and upper limit values:

$$w(x_{n-1}) = \alpha w_{n-1}(x_{n-1}) + (1 - \alpha) w_n(x_{n-1}) \quad (B.11)$$

Substitution of this relation into Eq. (B.10) gives:

$$\begin{aligned} \sum_{n=1}^N \int_{x=x_{n-1}}^{x_n} \left( \varphi^b(x) - \varphi^a(x) - u_m(x) \frac{\partial \varphi^b(x)}{\partial x} \right) w(x) dx - \\ \sum_{n=2}^N \{ \alpha w_{n-1}(x_{n-1}) u(x_{n-1}) (\varphi_n^b(x_{n-1}) - \varphi_{n-1}^b(x_{n-1})) + \\ (1 - \alpha) w_n(x_{n-1}) u(x_{n-1}) (\varphi_n^b(x_{n-1}) - \varphi_{n-1}^b(x_{n-1})) \} = 0 \end{aligned} \quad (B.12)$$

Consider element  $n$  and rename  $w_n^1 = w_n(x_{n-1})$ ,  $w_{n-1}^2 = w_{n-1}(x_{n-1})$ ,  $\varphi_n^{b1} = \varphi_n^b(x_{n-1})$ , and  $\varphi_{n-1}^{b2} = \varphi_{n-1}^b(x_{n-1})$ , where the upper index indicates the element node number, then we get:

$$\int_{x=x_{n-1}}^{x_n} \left( \varphi^b(x) - \varphi^a(x) - u_m(x) \frac{\partial \varphi^b(x)}{\partial x} \right) w(x) dx -$$



## B.2 Two-dimensional implementation of the DG method

For the two-dimensional case, the discretised form of Eq. (B.1) has to be solved:

$$\varphi^b - \varphi^a - \vec{u}_m \cdot \vec{\nabla} \varphi^b = 0 \quad (\text{B.17})$$

For this equation, the Discontinuous Galerkin method results in:

$$\int_{\Omega} w \left( \varphi^b - \varphi^a - \vec{u}_m \cdot \vec{\nabla} \varphi^b \right) d\Omega - \sum_{\forall e} \int_{\Gamma_e} w \vec{u}_m \cdot \vec{n} (\varphi^b - \varphi_{ext}^b) d\Gamma = 0 \quad \forall w \quad (\text{B.18})$$

in which  $\Gamma_e^e$  is the inflow boundary ( $\vec{u}_m \cdot \vec{n} > 0$ ) of an element  $e$  with outward unit normal  $\vec{n}$ , and  $\varphi_{ext}^b$  is the value of  $\varphi^b$  on the upstream side of  $\Gamma_e^e$ . Using a Cartesian vector base  $\{\vec{e}_1, \vec{e}_2\}$ , elaboration of the first term of Eq. (B.18) for element  $e$  gives:

$$\underline{w}^T \underbrace{\int_{\Omega_e} \underline{N} \underline{N}^T d\Omega}_{\underline{M}} (\varphi^b - \varphi^a) - \underline{w}^T \underbrace{\int_{\Omega_e} \underline{N} \left[ u_x \frac{\partial \underline{N}^T}{\partial x} + u_y \frac{\partial \underline{N}^T}{\partial y} \right] d\Omega}_{\underline{K}} \varphi^b \quad (\text{B.19})$$

where  $\underline{N}$  is the element shape function column, which is filled with the components of the shape function of a 4-noded bi-linear quadrilateral element.

Introducing  $\underline{N}_B = \underline{D} \underline{N}$  as the shape function on the boundary of an element with  $\underline{D} = \underline{D}_{in}$  in case of evaluation of the current element and  $\underline{D} = \underline{D}_{ex}$  in case of evaluation of the adjacent upstream element, the upwinding term can be written as

$$\int_{\Gamma_e^i} \underline{N}_B^T \underline{w}_B \underline{u}_n (\underline{N}_B^T \varphi_B^b - \underline{N}_B^T \varphi_{E,ext}^b) d\Gamma$$

where  $\underline{u}_n = \vec{u}_m \cdot \vec{n}$ . Further elaboration yields

$$\begin{aligned} & \underline{w}_B^T \int_{\Gamma_e^i} \underline{N}_B \underline{u}_n \underline{N}_B^T d\Gamma (\varphi_B^b - \varphi_{E,ext}^b) = \\ & (\underline{D}_{in} \underline{w})^T \underbrace{\int_{\Gamma_e^i} \underline{N}_B \underline{u}_n \underline{N}_B^T d\Gamma}_{\underline{Q}_B} (\underline{D}_{in} \varphi^b - \underline{D}_{ex} \varphi_{ext}^b) = \\ & \underline{w}^T \underbrace{\underline{D}_{in}^T \underline{Q}_B \underline{D}_{in}}_{\underline{Q}_{in}} \varphi^b - \underline{w}^T \underbrace{\underline{D}_{in}^T \underline{Q}_B \underline{D}_{ex}}_{\underline{Q}_{ex}} \varphi_{ext}^b \end{aligned} \quad (\text{B.20})$$

The  $\underline{D}$  matrices are used to select the nodal values from the upstream element, belonging to  $\Gamma_e^i$ . Substitution of Eqs. (B.19) and (B.20) into Eq. (B.18), gives

$$\underline{w}^T \underline{M} (\varphi^b - \varphi^a) - \underline{w}^T \underline{K} \varphi^b - \underline{w}^T \underline{Q}_{in} \varphi^b + \underline{w}^T \underline{Q}_{ex} \varphi_{ext}^b = 0 \quad \forall \underline{w}$$

which results in the following system of equations:

$$\left(\underline{M} - \underline{K} - \underline{Q}_{in}\right) \underline{\phi}^b = \underline{M}\underline{\phi}^a - \underline{Q}_{ex}\underline{\phi}_{ext}^b \quad (\text{B.21})$$

Although the DG method is unconditionally stable due to the (implicit) backward Euler discretisation scheme, it is diffusive for large Courant numbers as shown in Chapter 3. Therefore, to avoid excessive diffusion, the Courant number is limited by splitting the transport step into a number of sub-increments  $i_{sub} = 1, \dots, i_{sub,max}$ .

Eq. (B.21) is solved subsequently for all elements in a semi-explicit/implicit manner, inspired by Baaijens (1994). The implicit/explicit solver is given by:

$$\underline{A}\hat{\underline{\phi}}^{b^{i+1}} = \underline{M}\underline{\varphi}^a - \underline{Q}_{ex}\hat{\underline{\phi}}_{ext}^{b^i} \quad (\text{B.22})$$

where  $\underline{A} = \underline{M} - \underline{K} - \underline{Q}_{in}$  and  $\hat{\underline{\phi}}^{b^{i+1}}$  denotes the estimated  $\underline{\varphi}^b$  at iteration  $i = 1, \dots, i_{max}$ , with as first estimate:

$$\hat{\underline{\phi}}^{b^1} = \underline{\varphi}^a \quad (\text{B.23})$$

This equation is solved for each element separately, resulting in an updated  $\hat{\underline{\phi}}^{b^{i+1}}$  for this element, which is not only used in the next iteration, but also for the remaining elements in this iteration, for the estimation of the external term of the right-hand side. This results in a new global  $\hat{\underline{\phi}}^{b^{i+1}}$ , which is used to obtain a better estimation in the next iteration, until convergence is obtained.

Implementation of the algorithm can be efficiently done by storing the inverse of the element stiffness matrices  $\underline{A}^{-1}$  and  $\underline{Q}_{ex}$  and re-using these every subincrement and iteration. To reduce computational costs even further, the values of  $\underline{M}\underline{\varphi}^a$  for every element are calculated every subincrement and re-used every iteration. A flow scheme of the implementation is given in Figure B.2.

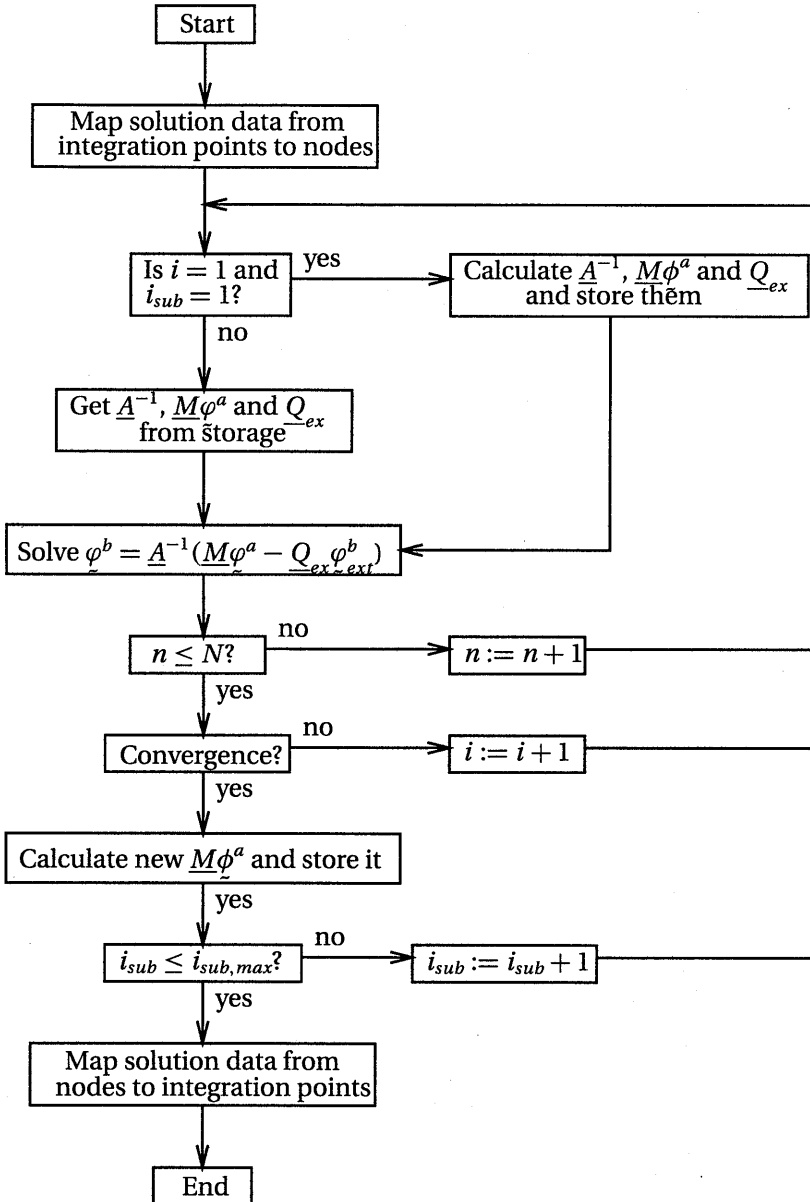


Figure B.2. Flow scheme of the implicit-explicit DG implementation.



# Bibliography

- van der Aa, M.A.H. Schreurs, P.J.G. and Baaijens, F.P.T. (1997). Numerical analysis of the wall-ironing process of coated sheet metal. In D.R.J. Owen, E. Oñate, and E. Hinton, editors, *Proc. Fifth Int. Conf. on Computational Plasticity, Fundamentals and Applications*, 1439–1444. Pineridge Press. Barcelona, Spain.
- van der Aa, M.A.H. Schreurs, P.J.G. and Baaijens, F.P.T. (1998a). Modelling of the wall ironing process of polymer coated sheet metal. In S.R. Idelsohn, E. Oñate, and E.N. Dvorkin, editors, *Proc. Fourth World Congress on Computational Mechanics*, on CDROM. Buenos Aires, Argentina.
- van der Aa, M.A.H. Schreurs, P.J.G. and Baaijens, F.P.T. (1998b). Numerical and experimental analysis of the wall ironing process of polymer coated sheet metal. In J. Huétink and F.P.T. Baaijens, editors, *Proc. Sixth International Conference on Numerical Methods in Industrial Forming Processes*, 603–608. Balkema, Rotterdam. Enschede, The Netherlands.
- Appleby, E.J. Lu, C.Y. Rao, R.S. Devenpeck, M.L. Wright, P.K. and Richmond, O. (1984). Strip drawing: A theoretical-experimental comparison. *Int. J. Mech. Sc.*, **26**(5), 351–362.
- Avitzur, B. (1968). *Metal Forming: Processes and Analysis*. Materials Science and Engineering Series. McGraw-Hill, New York.
- Avitzur, B. (1983). *Handbook of Metal Forming Processes*. Wiley Interscience Publication, New York.
- Baaijens, F.P.T. (1991). Calculation of residual stresses in injection-molded products. *Rheologica Acta*, **30**, 284–299.
- Baaijens, F.P.T. (1993). An U-ALE formulation of 3-D unsteady viscoelastic flow. *Int. J. Num. Meth. Eng.*, **36**, 1115–1143.
- Baaijens, F.P.T. (1994). Numerical experiments with a Discontinuous Galerkin method including monotonicity enforcement on the stick-slip problem. *J. Non-Newtonian Fluid Mech.*, **51**, 141–159.

- Balmer, R.T. (1990). *Thermodynamics*. West Publishing Company.
- Bergeson, B.T. and Reiling, M. (1997). *Two-Piece Beverage Canmaking*. Sayers Publishing Group Ltd.
- Besseling, J.F. and van der Giessen, E. (1994). *Mathematical Modelling of Inelastic Deformation*, volume 5 of *Applied Mathematics and Mathematical Computation*. Chapman & Hall, 2-6 Boundary Row, London SE1 8HN, UK, first edition.
- Bodner, S.R. and Partom, Y. (1975). Constitutive equations for elastic-viscoplastic strain-hardening materials. *Journal of Applied Mechanics*, **42**, 385–389.
- Boyce, M.C. Weber, G.G. and Parks, D.M. (1989). On the kinematics of finite strain plasticity. *J. Mech. Phys. Solids*, **37**(5), 647–665.
- Brokken, D., Brekelmans, W.A.M., and Baaijens, F.P.T. (1998). Numerical modelling of the metal blanking process. *J. Mater. Proc. Techn.*, **83**(1-3), 192–199.
- Brooks, A.N. and Hughes, T.J.R. (1982). Streamline upwind / Petrov Galerkin formulations for convection dominated flows with particular emphasis on the incompressible Navier-Stokes equations. *Comp. Meth. in Appl. Mech. and Eng.*, **32**, 199–259.
- Brown, M. and Nutting, J. (1997). The world in cans: beverages. *The Canmaker*, 42–43.
- Bruck, H.A. McNeill, S.R. Sutton, M.A. and Peters III, W.H. (1989). Digital image correlation using Newton-Raphson method of partial differential correction. *Exp. Mech.*, **29**, 261–267.
- Chan, K.S. Bodner, S.R. and Lindholm, U.S. (1988). Phenomenological modeling of hardening and thermal recovery in metals. *J. Eng. Mat. Technol.*, **110**, 1–8.
- Christiansen, A.W. Baer, E. and Radcliffe, S.V. (1971). The mechanical behaviour of polymers under high pressure. *Phil. Mag.*, **24**(188), 451–467.
- Deneuve, P. and Lecot, R. (1994). The study of friction in ironing process by physical and numerical modelling. *J. Mat. Proc. Techn.*, **45**, 625–630.
- Devenpeck, M.L. and Rigo, J.H. (1979). Research apparatus for simulating high-speed drawing of thin strip. In *Proc. of 7th NAMRC*, 81–88. SME.
- Doege, E. Ragab, M.S. and Galal, G.M.A. (1992). Experimental and numerical simulation of the ironing process by strip drawing. In *Comp. Plasticity, Fundamentals and Applications. Proc. Third Int. Conf.*, 1345–1356.
- Fukui, S. Ohi, T. Kudo, H. Takita, I. and Seino, J. (1962). Some aspects of friction in metal-strip drawing. *Int. J. Mech. Sc.*, **4**, 297–312.



- Geers, M.G.D. de Borst, R. and Brekelmans, W.A.M. (1996). Computing strain fields from discrete displacement fields in 2d-solids. *Int. J. Solids Struct.*, **33**, 4293–4307.
- Gelten, C.J.M. and de Jong, J.E. (1987). A method to redefine a finite element mesh and its application to metal forming and crack growth analysis. In *Proc. European Conf. on nonlinear finite element analysis*. Paper 4.
- Gill, P.E. Murray, W. and Wright, M.H. (1981). *Practical Optimisation*. Academic Press Inc.
- Gilman, J.J. (1969). *Micromechanics of Flow in Solids*. McGraw-Hill, New York.
- Haward, R.N. (1993). Strain hardening of thermoplastics. *Macromolecules*, **26**, 5860–5869.
- Hinton, E. and Campbell, J.S. (1974). Local and global smoothing using a least squares method. *Int. J. Num. Meth. Eng.*, **8**, 461–480.
- Huang, Y.M. Lu, Y.H. and J.W., Chan (1991). An elasto-plastic finite element and experimental study of the ironing process. *J. Mat. Proc. Techn.*, **26**, 53–80.
- Huétink, J. Vreede, P.T. and van der Lugt, J. (1990). Progress in mixed Eulerian-Lagrangian finite element simulation of forming processes. *Int. J. Num. Meth. Eng.*, **30**, 1441–1457.
- Hulsen, M.A. (1992). *The discontinuous Galerkin method with explicit Runge-Kutta time integration for hyperbolic and parabolic systems with source terms*. Delft University of Technology.
- Jaworski, J.A. Frigon, A.J. Schmid, S.R. and Wang, J.E. (1997). Tribological characteristics of coated steels in ironing. In *Proc. First International Conference on Tribology in Manufacturing Processes*.
- Jayachandran, R. Boyce, M.C. and Argon, A.S. (1995). Design of multilayer polymeric coatings for indentation resistance. *J. Comp.-Aided Mat. Des.*, **2**, 151–166.
- Kawai, N. Nakamura, T. and Dohda, K. (1982a). Development of anti-weldability test in metal forming by means of strip-ironing type friction testing machine. *J. Eng. Ind.*, **104**, 375–382.
- Kawai, N. Nakamura, T. and Miyamoto, S. (1982b). On the assessment of lubricity in the deformation process by a strip-ironing type friction testing machine. *Bull. of the JSME*, **25**(199), 95–102.
- Kawai, N. Daohda, K. Saito, M. Hayashi, N. and Wang, Z. (1992). Friction behaviour in the cup ironing process of aluminum sheets. *J. of Eng. for Ind.*, **114**, 175–180.

- Kenny, L.D. and Sang, H. (1986). Effect of particles on scoring and friction in ironing. In *Metal Transfer and Galling in Metallic Systems*, 117–130. AIME.
- Kolkailah, F.A. and McPhate, A.J. (1990). Bodner-partom constitutive model and non-linear finite element analysis. *J. Eng. Mat. Technol.*, **112**, 287–291.
- Leonov, A.I. (1976). Nonequilibrium thermodynamics and rheology of viscoelastic polymer media. *Rheol. Acta*, **15**, 85–98.
- Lesaint, P. and Raviart, P.A. (1974). On a finite element method for solving the neutron transport equation. *Proc. of symp. on mathematical aspects of finite elements in partial differential equations*, 89–123.
- Liu, W.K., Chang, H., Chen, J.S., and Belytschko, T. (1988). Arbitrary Lagrangian-Eulerian Petrov-Galerkin finite elements for nonlinear continua. *Comp. Meth. Appl. Mech. Eng.*, **68**, 259–310.
- MARC (1997). *MARC manuals A-F*. MARC Analysis Research Corporation, Palo Alto, California, U.S.A., Revision K.7 edition.
- MATLAB (1996). *MATLAB Reference Guide, version 4*. The MathWorks Inc., Natick, Mass., U.S.A.
- Meuwissen, M.H.H. (1998). *An inverse method for the mechanical characterisation of metals*. Ph.D. thesis, Eindhoven University of Technology, Netherlands.
- Morgan, E. (1985). *Tinplate and modern canmaking technology*. The Pergamon materials engineering practice series. Pergamon Press Ltd., first edition.
- Nagtegaal, J.C. and Veldpaus, F.E. (1984). *Numerical Analysis of Forming Processes*, chapter 12, On the Implementation of Finite Strain Plasticity Equations in a Numerical Model, 351–371. John Wiley & Sons Ltd.
- Nichols, I.E. Louwerse, G. and Crook, A.J.L. (1995). The application of novel numerical methods to multiple state forming operations in the manufacture of thin walled steel cans. In S. Shen and P. Dawson, editors, *Simulation of Materials Processing: Theory, Methods and Applications. Proc. Fifth Int. Conf. on Numerical Methods in Industrial Forming Processes*, 773–778. Balkema, Rotterdam.
- Odell, E.I. (1978). A study of wall ironing by the finite element technique. *Journal of Engineering for Industry*, **100**, 31–36.
- Oden, J.T. and Brauchli, H.J. (1971). Local and global smoothing using a least squares method. *Int. J. Num. Meth. Eng.*, **3**, 371–324.
- van Rijn, R. (1998). Measuring of punch forces during processing of polymer coated material into a DWI 73mm can. Technical report, Hoogovens R&D, Centre for Packaging Technology.

- Rowley, M.A. and Thornton, E.A. (1996). Constitutive modeling of the visco-plastic response of hastelloy-x and aluminium alloy 8009. *J. Eng. Mat. Technol.*, **118**, 19–27.
- Rubin, M.B. (1987). An elastic-viscoplastic model exhibiting continuity of solid and fluid states. *Int. J. Eng. Sci.*, **25**(9), 1175–1191.
- Rubin, M.B. (1989). A time integration procedure for plastic deformation in elastic-viscoplastic metals. *J. Appl. Math. Phys. (ZAMP)*, **40**, 846–871.
- Rubin, M.B. and Attia, A. (1996). Calculation of hyperelastic response of finitely deformed elastic-viscoplastic materials. *Int. J. Num. Meth. Eng.*, **39**, 309–320.
- Rubin, M.B. and Yarin, A.L. (1993). On the relationship between phenomenological models for elasto-viscoplastic metals and polymeric liquids. *J. Non-Newtonian Fluid Mech.*, **50**, 79–88.
- Saito, M. Saiki, H. and Kawai, N. (1989). Experimental analysis of ironing of thin metal cups. *ASME J. of Eng. for Ind.*, **111**, 56–63.
- Schrauwen, B.A.G. Faessen, J.P.M. and Govaert, L.E. (1998). Personal communication.
- Schreurs, P.J.G. Veldpaus, F.E. and Brekelmans, W.A.M. (1986). Simulation of forming processes, using the arbitrary Eulerian-Lagrangian formulation. *Comp. Meth. Appl. Mech. Eng.*, **58**, 19–36.
- Schünemann, M. Ahmetoglu, M.A. and Altan, T. (1996). Prediction of process conditions in drawing and ironing of cans. *J. Mat. Proc. Techn.*, **59**, 1–9.
- SEPRAN (1995). *SEPRAN Programmers Guide*. Ingenieursbureau SEPRA, Leidschendam, The Netherlands.
- Shawki, G.S.A. (1970). Optimum design of ironing dies. *Sheet Metal Industries*, 855–863.
- Simo, J.C. (1987). On a fully three dimensional finite strain viscoelastic damage model: formulation and computational aspects. *Comp. Meth. Appl. Mech. Eng.*, **60**, 153–173.
- Skipor, A.F. Harren, S.V. and Botsis, J. (1996). On the constitutive response of 63/37 Sn/Pb eutectic solder. *J. Eng. Mat. Technol.*, **118**, 1–11.
- Smit, R.J.M. Brekelmans, W.A.M. and Baaijens, F.P.T. (1999). Flexible, consistent and fully implicit finite element implementation of the generalised compressible Leonov model. *Int. J. Num. Meth. Eng.* Submitted for publication.
- Sutton, M.A. Cheng, M. Peters, W.H. Chao, Y.J. and McNeill, S.R. (1986). Application of an optimized digital correlation method to planar deformation analysis. *Image and Vision Computing*, **4**, 143–150.

- Tervoort, T.A. (1996). *Constitutive Modelling of Polymer Glasses, Finite Nonlinear Viscoelastic Behaviour of Polycarbonate*. Ph.D. thesis, Eindhoven University of Technology.
- Timmermans, P.H.M. (1997). *Evaluation of a constitutive model for solid polymeric materials: model selection and parameter quantification*. Ph.D. thesis, Eindhoven University of Technology, The Netherlands.
- Tufekci, S.S. Ahmetoglu, M.A. Kinzel, G.L. and Altan, T. (1995). Process simulation for can manufacturing by deep drawing and ironing. In *SAE Paper No. 950696*, 45–53. International Congress and Exposition, Detroit, Michigan.
- Vreugdenhil, C.B. and Koren, B. (Eds.) (1993). *Numerical methods for advection-diffusion problems*, volume 45 of *Notes on numerical fluid mechanics (NNFM)*. Vieweg.
- Wang, X.J. Jonasson, D. and Duncan, J.L. (1986). Ironing dynamometer for studying wall ironing in the cupping proces. In *Int. Deep Drawing Research Group; Proc. of the 14th Conf.*, 201–217.
- Wilson, W.R.D. and Cazeault, P. (1976). Measurement of frictional conditions in lubricated strip drawing. In *Proc. of the 4th NAMRC*, 165–171. SMI.
- Zaroulis, J.S. and Boyce, M.C. (1997). Temperature, strain rate, and strain state dependence of the evolution in mechanical behaviour and structure of poly(ethylene terephthalate) with finite strain deformation. *Polymer*, **38**(6), 1303–1315.
- Zoller, P. and Bolli, P. (1980). Pressure-volume-temperature relationships of solid and molten poly(ethylene terephthalate). *J. Macromol. Sci. Part B : Physics*, **B18**(3), 555–568.

# Samenvatting

Het Draw and Wall Ironing (DWI) proces is een metaalomvormproces, waarin een dieptrekstap wordt gevolgd door een wandstrekbewerking resulterend in een dunwandig, cilindrisch eindproduct. Industriële toepassing vindt plaats ten behoeve van een groot aantal producten: drank- en voedselbussen, batterijhulzen, en gas- en hydraulische cilinders. In het huidige productieproces van drank- en voedselbussen worden binnen- en buitenkant van de bussen gelakt. Meerdere wasstappen zijn daarom nodig om smeermiddel en emulsies te verwijderen. Het wassen en lakken van de bussen is kostbaar en vormt een aanzienlijke milieubelasting.

In dit proefschrift wordt een alternatieve methode beschreven, waarbij metaal, dat aan beide zijden met een polymeerlaag is gecoat, tot een bus wordt omgevormd. Deze coating fungeert daarbij als: (1) smeermiddel tijdens het omvormen, (2) beschermingslaag tegen corrosie (aan de binnenkant), en (3) basislaklaag (aan de buitenkant). Verwacht wordt dat deze werkwijze leidt tot een kostprijzreductie en een aanzienlijke vermindering van de milieubelasting.

Ten behoeve van efficiënte optimalisering van het fabricageproces en verbetering van het eindproduct is numerieke simulatie essentieel. Het omvormproces wordt gekarakteriseerd door grote, gelocaliseerde rekken, de beweging van vrije oppervlakken, en, vanwege de hoge productiesnelheden, een aanzienlijke thermo-mechanische koppeling. Om het omvormproces te simuleren is een eindige elementen model ontwikkeld, gebaseerd op een Arbitraire Lagrange Euler (ALE) beschrijvingswijze gebruikmakend van een Operator Splitting techniek (OS-ALE). Na een Lagrange stap, resulterend in een aanzienlijke vervorming van de elementen, worden de posities van knooppunten aangepast, zodat met een goed geconditioneerde mesh verder gerekend kan worden. Toestandsvariabelen, zoals spanningen en plastische rekken, worden daarna naar de nieuwe mesh getransporteerd met de Discontinuous Galerkin (DG) methode, die bij uitstek geschikt is voor het nauwkeurig transporteren van discontinue variabelen.

Vanwege de optredende hoge deformatiesnelheden in het DWI proces, vertonen zowel metaal als polymere coating elasto-viscoplastisch materiaalgedrag. Ter beschrijving hiervan wordt voor beide materialen een analoog model gebruikt: het gegeneraliseerd compressible Leonov model. Voor het polymeer wordt een Eyring viscositeitsfunctie gebruikt en voor het metaal een Bodner-Partom viscositeitsfunctie. Materiaalparameters in deze modellen zijn bepaald door het uitvoeren van trek- en compres-

sieproeven bij hoge snelheden en hoge hydrostatische drukken.

Voor de verificatie van het model is een experimentele opstelling gebouwd, waarin strips gecoat materiaal dungetrokken worden. Door middel van een numeriek-experimentele methode kunnen berekende en gemeten proceskrachten worden vergeleken. Bovendien kunnen met behulp van een digitale image correlatietechniek verplaatsingsvelden bepaald en vergeleken worden met simulatieresultaten.

Het ontwikkelde en experimenteel gevalideerde eindige elementen model voor het wandstrekken van polymeergecoat plaatmateriaal kan gebruikt worden om gericht en sneller drank- en voedselbussen te ontwerpen. Invloeden van de belangrijkste parameters in het proces, zoals gereedschapshoek, materiaalkeuze, deformatiesnelheid en diktereductie zijn onderzocht. Een handzame opstelling is gerealiseerd waarmee realistische beproevingen qua procesomstandigheden kunnen worden gedaan m.b.t. keuze van metaal, coating en gereedschap.

# Dankwoord

Tot slot wil ik de mensen bedanken die een bijdrage hebben geleverd aan het proefschrift:

- Piet Schreurs, Frank Baaijens en Han Meijer voor de enthousiaste begeleiding en discussies met hen.
- Wim van Veenen, Bert van Haastrecht, Stef Kamperman, Paul Tamis, Henk Ras en René van Rijn van Hoogovens Research & Development, Centre for Packaging Technology. Bedankt voor de motiverende discussies en bijdragen aan het onderzoek.
- David Shelby, Jennifer Stewart, Vicky Long and Brenda McClellan from Eastman Chemical Company, Kingsport, USA. Thank you for the materials, the measurements and the pleasant stay.
- Alan Duckett, Keith Norris and Pete Hine from IRC for Polymer Science and Technology, Leeds, UK. The opportunity to perform tensile tests under superimposed pressure at IRC is gratefully acknowledged.
- Voormalige studenten: Olaf van der Sluis, Michiel Spek, Joram Manie en Erik van der Aa.
- Alle collega's uit de Materials Technology groep, en in het bijzonder: Dirk Brokken, Robert Smit, Ad Goijaerts, dispuutsgenoot Bas van Rens en Marcel Meuwissen.
- Odette en onze ouders voor hun onvoorwaardelijke steun.

Maycel van der Aa  
Eindhoven, 4 maart 1999





# Curriculum Vitae

5 febr. 1971	Geboren te Den Dungen
1983 - 1989	R.K. Gymnasium Beekvliet te Sint Michielsgestel
1989 - 1994	Werktuigbouwkunde aan de Technische Universiteit Eindhoven. Afstudeerrichting: Systeem - en Regeltechniek
1994 - 4 mrt 1999	Assistent in Opleiding bij Sectie Materials Technology van de Technische Universiteit Eindhoven



# Stellingen

behorende bij het proefschrift

## Wall ironing of polymer coated sheet metal

1. Drukopbouw in de polymere coating is van essentieel belang voor het succesvol wandstrekken van polymeergecoat plaatmateriaal.

*Dit proefschrift, hoofdstuk 4*

2. Door de keuze van de viscositeitsfunctie kan met één constitutief model het mechanisch gedrag van polymeren en metalen goed worden beschreven.

*Dit proefschrift, hoofdstuk 2*

3. Inzicht in het wandstrekproces van polymeergecoat materiaal wordt in belangrijke mate verkregen door numerieke modelvorming van dit complexe vormgevingsproces (grote deformaties, hoge deformatiesnelheden, hoge hydrostatische drukken en thermo-mechanische koppeling).

*Dit proefschrift, hoofdstukken 2 en 3*

4. Bij voldoende drukopbouw in de polymere coating gedurende het omvormen van polymeergecoat metaal zal de (veranderende) glastemperatuur niet bereikt worden, mits de door wrijving en plastische deformatie opgewekte warmte een kritische grens niet overschrijdt.

*Dit proefschrift, hoofdstuk 4*

5. Zonder inzicht in het wiskundig model én kennis van numerieke optimalisatie (formulering van doelfunctie met beperkingen, bepalen van gevoeligheden, schaling e.d.) faalt procesoptimalisatie.

B. Štok and A. Mihelič (1995). Optimal design of the die shape using nonlinear finite element analysis. In S. Shen and P. Dawson, editors, *Proc. Fifth Int. Conf. on Numerical Methods in Industrial Forming Processes*, 625–630.

6. Een modelexperiment is essentieel voor het bestuderen van een proces in een grootschalige opstelling.

7. Voor vruchtbare samenwerking van industrie en universiteit, bepaalt de eerste de doelstellingen en de laatste de te kiezen weg.  
*Symposium Hora Est 'Onderzoek in Evenwicht', 16 mei 1997*
8. De overdraagbaarheid van software wordt aanzienlijk vergroot door het na de ontwikkelingsfase in te bedden in een commercieel pakket.
9. Een groeiend aantal promotiewerken komt beter tot zijn recht als de bijbehorende proefschriften op CD-ROM verschijnen, aangezien dit de interpretatie en presentatie van simulatieresultaten en experimenten vergemakkelijkt.
10. Zet, bij gebrek aan afstudeerders, familie in.

Maycel van der Aa,  
Eindhoven, 4 maart 1999.